

# Accepted Manuscript

The ALICE Transition Radiation Detector: Construction, operation, and performance

ALICE Collaboration

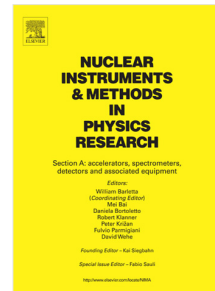
PII: S0168-9002(17)30998-1  
DOI: <http://dx.doi.org/10.1016/j.nima.2017.09.028>  
Reference: NIMA 60107

To appear in: *Nuclear Inst. and Methods in Physics Research, A*

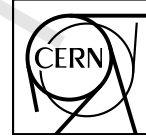
Received date: 11 September 2017  
Accepted date: 14 September 2017

Please cite this article as: The ALICE Transition Radiation Detector: Construction, operation, and performance, *Nuclear Inst. and Methods in Physics Research, A* (2017), <http://dx.doi.org/10.1016/j.nima.2017.09.028>

This is a PDF file of an unedited manuscript that has been accepted for publication. As a service to our customers we are providing this early version of the manuscript. The manuscript will undergo copyediting, typesetting, and review of the resulting proof before it is published in its final form. Please note that during the production process errors may be discovered which could affect the content, and all legal disclaimers that apply to the journal pertain.



## EUROPEAN ORGANIZATION FOR NUCLEAR RESEARCH



CERN-EP-2017-222  
29 August 2017

3

4

## The ALICE Transition Radiation Detector: construction, operation, and performance

5

ALICE Collaboration\*

6

### Abstract

7 The Transition Radiation Detector (TRD) was designed and built to enhance the capabilities of the  
8 ALICE detector at the Large Hadron Collider (LHC). While aimed at providing electron identifica-  
9 tion and triggering, the TRD also contributes significantly to the track reconstruction and calibration  
10 in the central barrel of ALICE. In this paper the design, construction, operation, and performance  
11 of this detector are discussed. A pion rejection factor of up to 410 is achieved at a momentum of  
12 1 GeV/c in p-Pb collisions and the resolution at high transverse momentum improves by about 40%  
13 when including the TRD information in track reconstruction. The triggering capability is demon-  
14 strated both for jet, light nuclei, and electron selection.

© 2017 CERN for the benefit of the ALICE Collaboration.

Reproduction of this article or parts of it is allowed as specified in the CC-BY-4.0 license.

---

\*See Appendix A for the list of collaboration members

## 1 Introduction

A Large Ion Collider Experiment (ALICE) [1, 2] is the dedicated heavy-ion experiment at the Large Hadron Collider (LHC) at CERN. In central high energy nucleus–nucleus collisions a high-density deconfined state of strongly interacting matter, known as quark–gluon plasma (QGP), is supposed to be created [3–5]. ALICE is designed to measure a large set of observables in order to study the properties of the QGP. Among the essential probes there are several involving electrons, which originate, e.g. from open heavy-flavour hadron decays, virtual photons, and Drell-Yan production as well as from decays of the  $\psi$  and  $\Upsilon$  families. The identification of these rare probes requires excellent electron identification, also in the high multiplicity environment of heavy-ion collisions. In addition, the rare probes need to be enhanced with triggers, in order to accumulate the statistics necessary for differential studies. The latter requirement concerns not only probes involving the production of electrons, but also rare high transverse momentum probes such as jets (collimated sprays of particles) with and without heavy flavour. The ALICE Transition Radiation Detector (TRD) fulfils these two tasks and thus extends the physics reach of ALICE.

Transition radiation (TR), predicted in 1946 by Ginzburg and Frank [6], occurs when a particle crosses the boundary between two media with different dielectric constants. For highly relativistic particles ( $\gamma \gtrsim 1000$ ), the emitted radiation extends into the X-ray domain for a typical choice of radiator [7–9]. The radiation is extremely forward peaked relative to the particle direction [7]. As the TR photon yield per boundary crossing is of the order of the fine structure constant ( $\alpha = 1/137$ ), many boundaries are needed in detectors to increase the radiation yield [10]. The absorption of the emitted X-ray photons in high-Z gas detectors leads to a large energy deposition compared to the specific energy loss by ionisation of the traversing particle.

Since their development in the 1970s, transition radiation detectors have proven to be powerful devices in cosmic-ray, astroparticle and accelerator experiments [10–20]. The main purpose of the transition radiation detectors in these experiments was the discrimination of electrons from hadrons via, e.g. cluster counting or total charge/energy analysis methods. In a few cases they provided charged-particle tracking. The transition radiation photons are in most cases detected either by straw tubes or by multiwire proportional chambers (MWPC). In some experiments [10, 13, 16, 21] and in test setups [22–25], short drift chambers (usually about 1 cm) were employed for the detection. Detailed reviews on the transition radiation phenomenon, detectors, and their application to particle identification can be found in [10, 26–28].

The ALICE TRD, which covers the full azimuth and the pseudorapidity range  $-0.84 < \eta < 0.84$  (see next section), is part of the ALICE central barrel. The TRD consists of 522 chambers arranged in 6 layers at a radial distance from 2.90 m to 3.68 m from the beam axis. Each chamber comprises a foam/fibre radiator followed by a Xe-CO<sub>2</sub>-filled MWPC preceded by a drift region of 3 cm. The extracted temporal information represents the depth in the drift volume at which the ionisation signal was produced and thus allows the contributions of the TR photon and the specific ionisation energy loss of the charged particle  $dE/dx$  to be separated. The former is preferentially absorbed at the entrance of the chamber and the latter distributed uniformly along the track. Electrons can be distinguished from other charged particles by producing TR and having a higher  $dE/dx$  due to the relativistic rise of the ionisation energy loss. The usage of the temporal information further enhances the electron-hadron separation power. Due to the fast read-out and online reconstruction of its signals, the TRD has also been successfully used to trigger on electrons with high transverse momenta and jets (3 or more high- $p_T$  tracks). Last but not least, the TRD improves the overall momentum resolution of the ALICE central barrel by providing additional space points at large radii for tracking, and tracks anchored by the TRD will be a key element to correct space charge distortions expected in the ALICE TPC in LHC RUN 3 [29]. A first version of the correction algorithm is already in use for RUN 2.

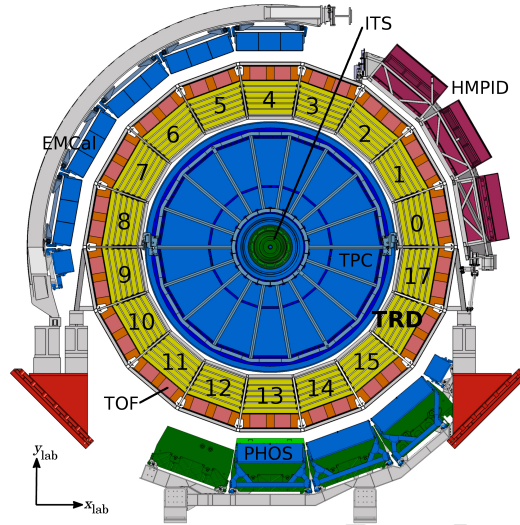


**Fig. 1:** Schematic cross-section of the ALICE detector perpendicular to the LHC beam direction (status of the detector since the start of LHC RUN 2). The central barrel detectors cover the pseudorapidity range  $|\eta| \lesssim 0.9$  and are located inside the solenoid magnet, which provides a magnetic field with strength  $B = 0.5$  T along the beam direction.

62 In this article the design, construction, operation, and performance of the ALICE TRD is described. Section  
 63 2 gives an overview of the detector and its construction. The gas system is detailed in Section 3.  
 64 The services required for the detector are outlined in Section 4. In Section 5 the read-out of the detector  
 65 is discussed and the Detector Control System (DCS) used for reliable operation and monitoring of the  
 66 detector is presented in Section 6. The detector commissioning and its operation are discussed in Section  
 67 7. Tracking, alignment, and calibration are described in detail in Sections 8, 9, and 10, while various  
 68 methods for charged hadron and electron identification are presented in Section 11. The use of the TRD  
 69 trigger system for jets, electrons, heavy-nuclei, and cosmic-ray muons is described in Section 12.

## 70 2 Detector overview

71 A cross-section of the central part of the ALICE detector [1, 2], installed at Interaction Point 2 (IP2)  
 72 of the LHC, is shown in Fig. 1. The central barrel detectors cover the pseudorapidity range  $|\eta| \lesssim 0.9$   
 73 and are located inside a solenoid magnet, which produces a magnetic field of  $B = 0.5$  T along the beam  
 74 direction. The Inner Tracking System (ITS) [30], placed closest to the nominal interaction point, is em-  
 75 ployed for low momentum tracking, particle identification (PID), and primary and secondary vertexing.  
 76 The Time Projection Chamber (TPC) [31], which is surrounded by the TRD, is used for tracking and  
 77 PID. The Time-Of-Flight detector (TOF) [32] is placed outside the TRD and provides charged hadron  
 78 identification. The ElectroMagnetic Calorimeter (EMCal) [33], the PHOTon Spectrometer (PHOS) [34],  
 79 and the High Momentum Particle Identification Detector (HMPID) [35] are used for electron, jet, pho-  
 80 ton and hadron identification. Their azimuthal coverage is shown in Fig. 1. Not visible in the figure  
 81 are the V0 and T0 detectors [36, 37], as well as the Zero Degree Calorimeters (ZDC) [38], which are  
 82 placed at small angles on both sides of the interaction region. These detectors can be employed, e.g.  
 83 to define a minimum-bias trigger, to determine the event time, the centrality and event plane of a col-  
 84 lision [2, 39, 40]. Likewise, the muon spectrometer [41, 42] is outside the view on one side of the  
 85 experiment, only, covering  $-4 < \eta < -2.5$ .

86 Figure 1 also shows the definition of the global ALICE coordinate system, which is a Cartesian system  
 87 with its point of origin at the nominal interaction point ( $x_{\text{lab}}, y_{\text{lab}}, z_{\text{lab}} = 0$ ); the  $x_{\text{lab}}$ -axis pointing in-

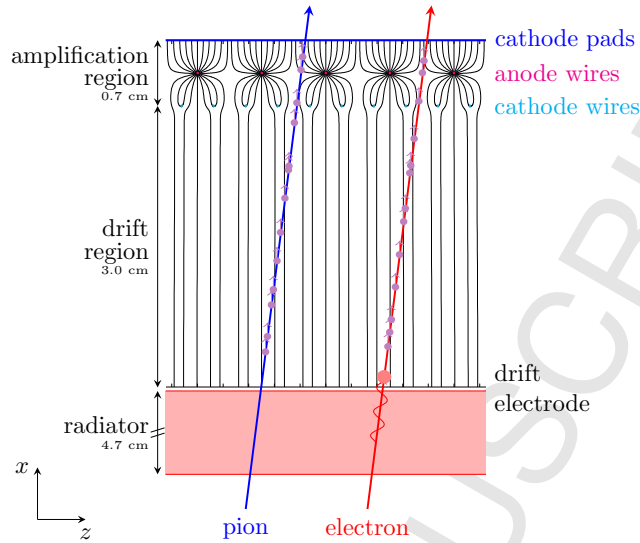


**Fig. 2:** Schematic cross-section of a TRD chamber in the  $x$ - $z$  plane (perpendicular to the wires) with tracks of a pion and an electron to illustrate the ionisation energy deposition and the TR contribution. The large energy deposition due to the TR photon absorption is indicated by the large red circle in the drift region. The drift lines (solid lines) are calculated with Garfield [43] and correspond to the nominal voltage settings for chamber operation. The radiator is not drawn to scale.

wards radially to the centre of the LHC ring and the  $z_{\text{lab}}$ -axis coinciding with the direction of one beam and pointing in direction opposite to the muon spectrometer. According to the (anti-)clock-wise beam directions, the muon spectrometer side is also called C-side, the opposite side A-side.

The design of the TRD is a result of the requirements and constraints discussed in the Technical Design Report [44]. It has a modular structure and its basic component is a multiwire proportional chamber (MWPC). Each chamber is preceded by a drift region to allow for the reconstruction of a local track segment, which is required for matching of TRD information with tracks reconstructed with ITS and TPC at high multiplicities. TR photons are produced in a radiator mounted in front of the drift section and then absorbed in a xenon-based gas mixture. A schematic cross-section of a chamber and its radiator is shown in Fig. 2. The shown local coordinate system is a right-handed orthogonal Cartesian system, similar to the global coordinate system, rotated such that the  $x$ -axis is perpendicular to the chamber. Six layers of chambers are installed to enhance the pion rejection power. An eighteen-fold segmentation in azimuth ( $\phi$ ), with each segment called ‘sector’, was chosen to match that of the TPC read-out chambers. In the longitudinal direction ( $z_{\text{lab}}$ ), i.e. along the beam direction, the coverage is split into five stacks, resulting in a manageable chamber size. The five stacks are numbered from 0 to 4, where stack 4 is at the C-side and stack 0 at the A-side. Layer 0 is closest, layer 5 farthest away from the collision point in the radial direction. In each sector, 30 read-out chambers (arranged in 6 layers and 5 stacks) are combined in a mechanical casing, called a ‘supermodule’ (see Fig. 3 and Section 2.3).

In total the TRD can host 540 read-out chambers (18 sectors  $\times$  6 layers  $\times$  5 stacks), however in order to minimise the material in front of the PHOS detector in three sectors (sectors 13–15, for numbering see Fig. 1) the chambers in the middle stack were not installed. This results in a system of 522 individual read-out chambers. The main parameters of the detector are summarised in Table 1.

At the start of the first LHC period (RUN 1) in 2009 the TRD participated with seven supermodules. Six further supermodules were built and integrated into the experiment during short winter shutdown periods of the accelerator, three in each winter shutdown period of 2010 and 2011. The TRD was completed during the Long Shutdown 1 (LS) of the LHC in 2013–2014. With all 18 supermodules installed, full

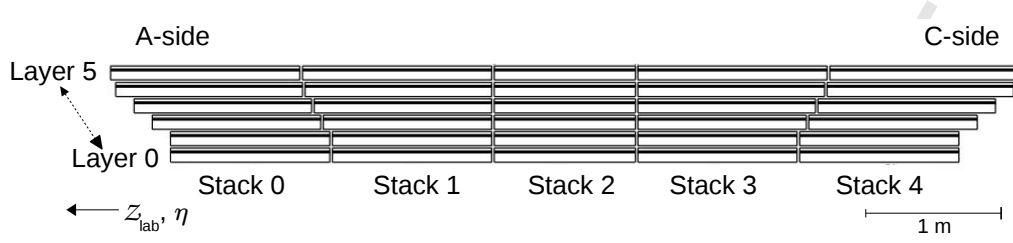


**Fig. 3:** Cross-section (longitudinal view) of a supermodule.

Parameter	Value
Pseudorapidity coverage	$-0.84 < \eta < +0.84$
Azimuthal coverage $\varphi$	$360^\circ$
Radial position	2.90 m to 3.68 m
Length of a supermodule	7.02 m
Weight of a supermodule	1.65 t
Segmentation in $\varphi$	18 sectors
Segmentation in $z_{\text{lab}}$	5 stacks
Segmentation in $r$	6 layers
Total number of read-out chambers	522
Size of a read-out chamber (active area)	$0.90 \text{ m} \times 1.06 \text{ m}$ to $1.13 \text{ m} \times 1.43 \text{ m}$
Radiator material	fibre/foam sandwich
Depth of radiator	4.7 cm
Depth of drift region	3.0 cm
Depth of amplification region	0.7 cm
Number of time bins (100 ns)	30 (22–24)
Total number of read-out pads	1 150 848
Total active area	$673.4 \text{ m}^2$
Detector gas	Xe-CO <sub>2</sub> (85-15)
Gas volume	$27 \text{ m}^3$
Drift voltage (nominal)	$\sim 2150 \text{ V}$
Anode voltage (nominal)	$\sim 1520 \text{ V}$
Gas gain (nominal)	$\sim 3200$
Drift field	$\sim 700 \text{ V/cm}$
Drift velocity	$\sim 1.56 \text{ cm}/\mu\text{s}$
Avg. radiation length along $r$ $\langle X/X_0 \rangle$	24.7%

**Table 1:** General parameters of the TRD. The indicated weight corresponds to a supermodule with 30 read-out chambers; the length of the supermodule does not include the connected services. At maximum 30 time bins can be read out, typical values used in RUN 1 and RUN 2 are 22–24 (see Section 5.2).

114 coverage in azimuth was accomplished for the second LHC period (RUN 2) starting in 2015.

## 115 2.1 Read-out chambers

116 The size of the read-out chambers changes radially and along the beam direction (see Fig. 3). The active  
 117 area per chamber thus varies from  $0.90 \text{ m} \times 1.06 \text{ m}$  to  $1.13 \text{ m} \times 1.43 \text{ m}$  ( $x \times z$ ). The optimal design of  
 118 a read-out chamber (see Fig. 2) was found considering the requirements on precision and mechanical  
 119 stability, and minimisation of the amount of material.

120 The construction of the radiator, discussed in the following sub-section, is essential for the mechanical  
 121 stability of the chamber. The drift electrode, an aluminised mylar foil ( $25 \mu\text{m}$  thick), is an integral part of  
 122 the radiator. To ensure a uniform drift field throughout the entire drift volume, a field cage with a voltage  
 123 divider chain is employed [44]. The current at nominal drift voltage is about  $170 \mu\text{A}$ . The grounded cath-  
 124 ode wires are made of Cu-Be and have a diameter of  $75 \mu\text{m}$ , while the anode wires are made of Au-plated  
 125 tungsten with a diameter of  $20 \mu\text{m}$ . The pitch for the cathode and anode wires are  $2.5 \text{ mm}$  and  $5 \text{ mm}$ , re-  
 126 spectively; the tensions at winding were  $1 \text{ N}$  and  $0.45 \text{ N}$  [45]. The wire lengths vary from  $1.08 \text{ m}$  to

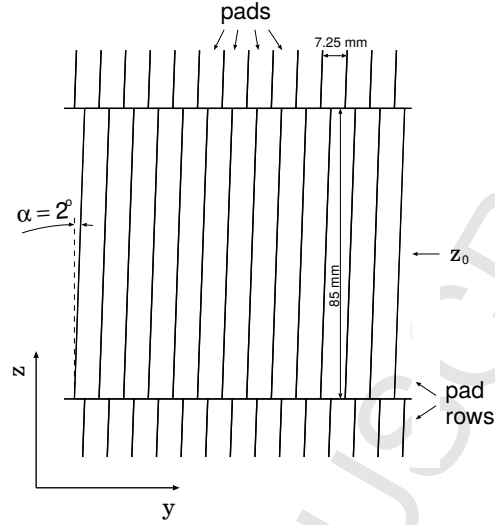


**Fig. 4:** Pad geometry of a TRD read-out chamber in layer 3 (not stack 2). The pad tilt is  $\pm 2^\circ$  with respect to the  $z$ -axis (along the beam direction), with the sign alternating between layers.

127 1.45 m. The maximum deformation of the chamber frame was  $150 \mu\text{m}$  under the wire tension indicated,  
 128 leading to a maximum 10% loss in wire tension. Even with an additional 1 mbar overpressure in the gas  
 129 volume (see Section 3), the deformation of the drift electrode can be kept within the specification of less  
 130 than 1 mm. The segmented cathode pad plane is manufactured from thin Printed Circuit Boards (PCB)  
 131 and glued on a light honeycomb and carbon fibre sandwich to ensure planarity and mechanical stiffness.  
 132 The design goal of having a maximum deviation from planarity of  $150 \mu\text{m}$  was achieved with only a  
 133 few chambers exceeding slightly this value. The PCBs of the pad plane were produced in two or three  
 134 pieces. The PCBs are segmented into 12 (stack 2) or 16 pads along the  $z$ -direction, and 144 pads in the  
 135 direction of the anode wires ( $r\phi$ ). The pad area varies from  $0.635 \text{ cm} \times 7.5 \text{ cm}$  to  $0.785 \text{ cm} \times 9 \text{ cm}$  [45]  
 136 to achieve a constant granularity with respect to the distance from the interaction point. The pad width  
 137 of  $0.635 \text{ cm}$  to  $0.785 \text{ cm}$  in the  $r\phi$  direction was chosen so that charge sharing between adjacent pads  
 138 (typically three), which is quantified by the pad response function (PRF) [46], is achieved. As a consequence,  
 139 the position of the charge deposition can be reconstructed in the  $r\phi$ -direction with a spatial  
 140 resolution of  $\lesssim 400 \mu\text{m}$  [46]. In the longitudinal direction, the coarser segmentation is sufficient for  
 141 the track matching with the inner detectors. In addition, the pads are tilted by  $\pm 2^\circ$  (sign alternating  
 142 layer-by-layer) as shown in Fig. 4, which improves the  $z$ -resolution during track reconstruction without  
 143 compromising the  $r\phi$  resolution. For clusters confined within one pad row, a  $z$  position at the row centre  
 144 is assumed,  $z_{\text{cluster}} = z_0$ . The honeycomb structure also acts as a support for the read-out boards. The pads  
 145 are connected to the read-out boards by short polyester ribbon cables via milled holes in the honeycomb  
 146 structure.

147 The original design of the TRD was conceived such that events with a multiplicity of  $dN_{\text{ch}}/d\eta = 8000$   
 148 would have led to an occupancy of 34% in the detector [44]. The fast read-out and processing of such  
 149 data on  $1.15 \cdot 10^6$  read-out channels required the design and production of fully customised front-end  
 150 electronics (see Section 5).

151 The positive signal induced on the cathode pad plane is amplified using a charge-sensitive PreAmplifier-  
 152 ShAper (PASA) (see Section 5) and the signals on the cathode pads are sampled in time bins of 100 ns  
 153 inside the TRAcKlet Processor (TRAP, see Section 5). For LHC RUN 1 and RUN 2 running conditions  
 154 (see Section 7.2), the probability for pile-up events is small. The averaged time evolution of the signal  
 155 is shown in Fig. 5 for pions and electrons, with and without radiator. In the amplification region (early  
 156 times), the signal is larger, because the ionisation from both sides of the anode wires contributes to the

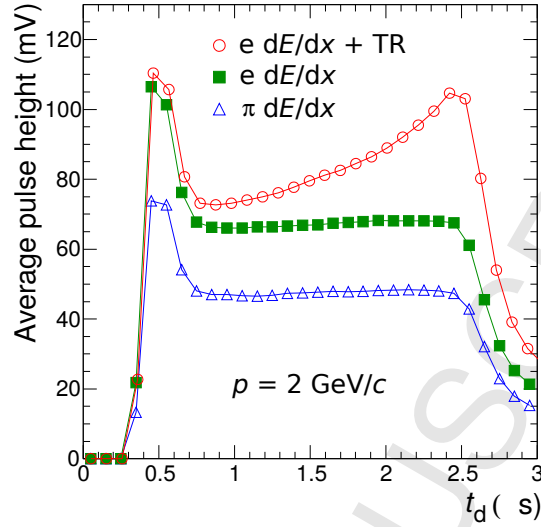


**Fig. 5:** Average pulse height as a function of drift time for pions and electrons (with and without radiator). The time axis is shown with an arbitrary offset of  $0.3 \mu\text{s}$ . The measurements were performed at the CERN PS with prototype read-out chambers that were smaller in overall size (active area  $25 \text{ cm} \times 32 \text{ cm}$ ) but otherwise similar in construction to that of the final detector. Figure taken from [47].

157 same time interval. The contribution of TR is seen as an increase in the measured average signal at  
 158 times corresponding to the entrance of the chamber (around  $2.5 \mu\text{s}$  in Fig. 5), where the TR photons are  
 159 preferentially absorbed. At large times (beyond  $2.5 \mu\text{s}$ ), the effect of the slow ion movement becomes  
 160 visible as a tail. Various approximations of the time response function, the convolution of the long tails  
 161 with the shaping of the PASA, were studied in order to optimally cancel the tails in data, see Section 8.

162 The knowledge of the ionisation energy loss is important for the control of the detector performance and  
 163 for tuning the Monte Carlo simulations. A set of measurements was performed with prototype read-out  
 164 chambers with detachable radiators for pions and electrons at various momenta [48]. An illustration of  
 165 the measured data is shown in Fig. 6 for pions and electrons with a momentum of  $2 \text{ GeV}/c$ . The sim-  
 166 ulations describe the Landau distribution of the total ionisation energy deposition, determined from the  
 167 calibrated time-integrated chamber signal. A compilation of such measurements over a broad momen-  
 168 tum range including data obtained with cosmic-ray muons and from collisions recorded with ALICE is  
 169 shown in Section 11, Fig. 37.

170 Measurements of the position resolution in the  $r\phi$ -direction ( $\sigma_r$ ) and angular resolution  $\sigma_\phi$ , conducted  
 171 with prototype chambers, established that the required performance of the detector and electronics  
 172 ( $\sigma_r \lesssim 400 \mu\text{m}$  and  $\sigma_\phi \leq 1^\circ$ ) is reached for signal-to-noise values of about 40, which corresponds to a  
 173 moderate gas gain of about 3500 [46].

174 The production of a chamber was performed in several steps [49] and completed in one week on average.  
 175 First, the aluminium walls of the chamber were aligned on a precision table and glued to the radiator  
 176 panel. The glueing table was custom-built to ensure the required mechanical precision and time-efficient  
 177 handling of the components. For almost all junctions the two-component epoxy glue Araldite<sup>®</sup> AW 116  
 178 with hardener HV 953BD was used. In a few places, where a higher viscosity glue was needed, Araldite<sup>®</sup>  
 179 AW 106 was applied. In a second step, the cathode and anode wires were wound on a custom-made  
 180 winding machine and glued onto a robust aluminium frame in order to keep the wire tension. This  
 181 aluminium frame was subsequently placed on top of the chamber body, and the cathode and anode wires  
 182 were transferred to the G10 ledges glued to the chamber body. After gluing of the anode and cathode  
 183 wire planes, the tension of each wire was checked by moving a needle valve with pressurised air across



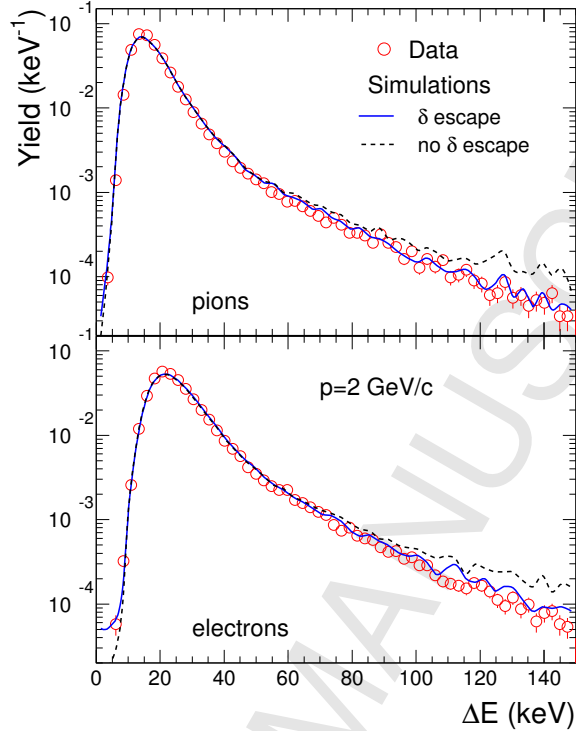


**Fig. 6:** Distributions of the ionisation energy loss of pions and electrons with momenta of 2 GeV/ $c$ . The symbols represent the measurements obtained at the CERN PS with prototype read-out chambers that were smaller in overall size (active area 25 cm  $\times$  32 cm) but otherwise similar in construction to that of the final detector. The lines are simulations accounting (continuous line) or not (dashed line) for the long range of  $\delta$ -electrons as compared to the chamber dimensions. Figure taken from [48].

184 the wires. The induced resonance frequency in each wire was determined by measuring the reflected  
 185 light of an LED [50]. Afterwards the pad plane and honeycomb structure were placed on top of the  
 186 chamber body. Following this production process, each chamber was subjected to a series of quality  
 187 control tests with an Ar-CO<sub>2</sub> (70-30) gas mixture. The tests were performed once before the chamber  
 188 was sealed with epoxy (closed with clamps) and repeated after chamber validation and glueing. In the  
 189 following the requirements are described [51]. The anode leakage current was required not to exceed a  
 190 value of 10 nA. The gas leak rate was determined by flushing the chamber with the Ar-CO<sub>2</sub> gas mixture  
 191 and measuring the O<sub>2</sub> content of the outflowing gas. It was required to be less than 1 mbar  $\cdot$  1/h. In  
 192 addition, the leak conductance was measured at an underpressure of 0.4–0.5 mbar in the chamber. The  
 193 underpressure test was only introduced at a later stage of the mass production after viscous leaks were  
 194 found, see Section 3.4.1 for more details. Comparisons of the anode current induced by a <sup>109</sup>Cd source  
 195 placed at 100 different positions across the active area allowed determinations of the gain uniformity.  
 196 The step size for this two-dimensional scan was about 10 cm in both directions and the measured values  
 197 were required to be within  $\pm$  15% of the median. Electrically disconnected wires were detected by  
 198 carrying out a one-dimensional scan perpendicular to the wires with a step size of 1 cm. This scan  
 199 clearly identified any individual wire that was not connected due to the visible gas gain anomaly in the  
 200 vicinity of this wire, and allowed for repair. For one position the absolute gas gain was determined by  
 201 measuring the anode current and by counting the pulses of the <sup>109</sup>Cd source. The long term stability was

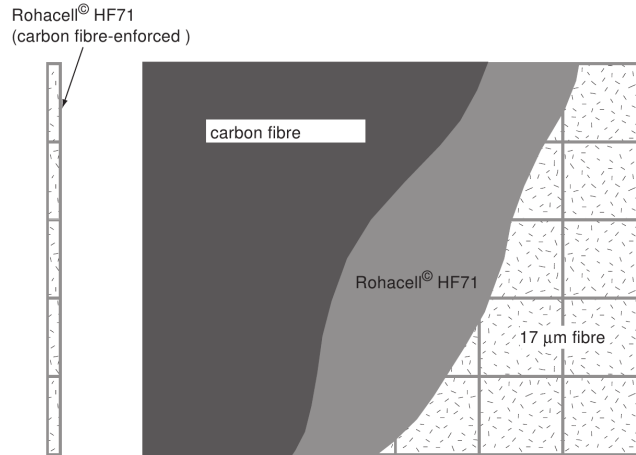


**Fig. 7:** Side (left) and top (right) view of the design of the TRD sandwich radiator [44].

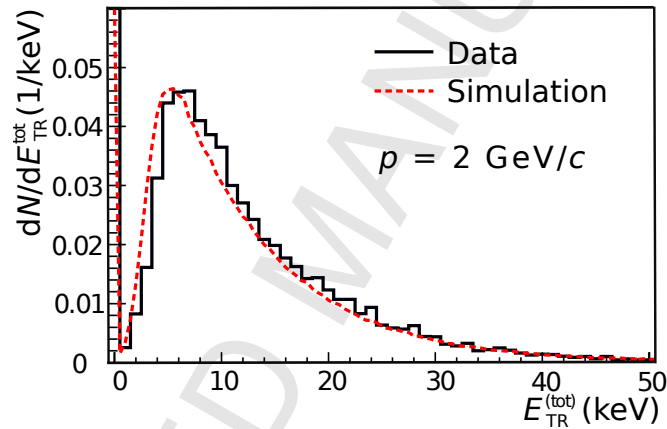


**Fig. 8:** Measured and simulated spectra of TR produced by electrons with a momentum of 2 GeV/c for the ALICE TRD sandwich radiator. Figure adapted from [53].

202 characterised by monitoring the gas gain in intervals of 15 minutes over a period of 12 hours.

## 203 2.2 Radiator

204 The design of the radiator is shown in Fig. 7. Polypropylene fibre mats of 3.2 cm total thickness are  
 205 sandwiched between two plates of Rohacell® foam HF71, which are mechanically reinforced by lamination  
 206 of carbon fibre sheets of 100 µm thickness. Aluminised kapton foils are glued on top, to ensure gas tight-  
 207 ness and to also serve as the drift electrode. For mechanical reinforcement, cross-bars of Rohacell® foam  
 208 of 0.8 cm thickness are glued between the two foam sheets of the sandwich, with a pitch of 20–25 cm  
 209 depending on the chamber size. After construction the transmission of the full radiator was measured  
 210 using the  $K_{\alpha}$  line of Cu at 8.04 keV to ensure the homogeneity of the radiators [52]. This line was chosen  
 211 as its energy is close to the most probable value of the TR spectrum (see Fig. 8).

212 Measurements with prototypes [53] indicated that such a sandwich radiator produces 30–40% less TR  
 213 compared to a regularly spaced foil radiator. However, constructing a large-area detector with radiators  
 214 made out of 100 regularly spaced foils each is infeasible. The impact of various radiators constructed  
 215 from fibres and/or foam on, e.g. particle identification is discussed in [47, 53]. Based on these measure-  
 216 ments the fibre/foam sandwich radiator design was chosen for the final detector.

217 The spectra of TR produced by electrons with a momentum of 2 GeV/c as measured with the ALICE  
218 TRD sandwich radiator is shown in Fig. 8. Such a measurement is important for the tuning of simula-  
219 tions in the ALICE setup. As the production of TR is not included in GEANT3 [54], which is used to  
220 propagate generated particles through the ALICE apparatus for simulations, we have explicitly added  
221 it to our simulations in AliRoot [55], the ALICE offline framework for simulation, reconstruction and  
222 analysis. An effective parameterisation of the irregular radiator in terms of a regular foil radiator is em-  
223 ployed as an approximation. The simulations describe the data satisfactorily including the momentum  
224 dependence [53].

### 225 2.3 Supermodule

226 The detector is installed in the spaceframe (the common support structure for most of the central barrel  
227 detectors) in 18 supermodules, each of which can host 30 read-out chambers arranged in 5 stacks and  
228 6 layers (see Fig. 3). The overall shape of the supermodule is a trapezoidal prism with a length of  
229 7.02 m (8 m including services). Its height is 0.78 m and the shorter (longer) base of the trapezoid is  
230 0.95 m (1.22 m). The weight of a supermodule with 30 read-out chambers is about 1.65 t. Mechanical  
231 stability is provided by a hull of aluminium profiles and sheets, connected with stainless steel screws.  
232 The materials were chosen to minimise the interference with the magnetic field in the solenoid magnet.  
233 In front of PHOS, where minimal radiation length is required, the aluminium sheets of the short and long  
234 base of the trapezoid were replaced by carbon-fibre windows.

235 All service connections must be routed internally to the end-caps of the supermodule. Those that require  
236 materials with large radiation length are placed at the sidewalls, outside the active area of the TRD and  
237 most other detectors in ALICE. This includes the low-voltage power distribution bus bars as well as  
238 other copper wires for the Detector Control System (DCS) board power, network and high-voltage (HV)  
239 connections between the fanout boxes and read-out chambers, and the rectangular cooling pipes (see  
240 Section 4 for more details).

241 Low-voltage (LV) power for the read-out boards is provided via copper power bus bars (2 for each layer  
242 and voltage as described in Table 3) with a cross-section of 6 mm × 6 mm (per channel) running along  
243 the sidewalls of the supermodule. Each read-out board is connected directly to the power bus bars. Heat  
244 generated by ohmic losses in the power bus bars is partially transferred to the adjacent cooling pipes  
245 (see Section 4.2). The power bus bars protrude about 30 cm from each side of the supermodule hull,  
246 where they are equipped with capacitors for voltage stabilisation. On one end-cap of the supermodule  
247 the power-bus bars are connected via a low-voltage patch panel to the long supply lines to the power  
248 supplies outside of the magnet.

249 Each read-out chamber is equipped with 6 or 8 read-out boards (see Section 2.1) and one DCS board (see  
250 Section 4.4). Power is provided and controlled separately for each DCS board by a power distribution  
251 box. The DCS boards are connected via twisted-pair cables to Ethernet patch panels at the end-caps and  
252 the boards of two adjacent layers are connected via flat-ribbon cables in a daisy chain loop to provide  
253 low-level Joint Test Action Group (JTAG) access to neighbouring boards.

254 For each chamber, three optical fibres are routed to the end-cap on the C-side. Two fibres connect the  
255 optical read-out interfaces to a patch panel, where they are linked via the Global Tracking Unit (GTU)  
256 (see Section 5) to the Data AcQuisition (DAQ) systems. One trigger fibre connects the DCS board to the  
257 trigger distribution box (see Section 5.1), which receives the trigger signals from the pretrigger system  
258 or its back-up system and splits them into 30 fibres (+ 2 spares).

259 The supermodules were constructed from 2006 to 2014. In the following, we discuss the sequence of  
260 required steps. After the construction of the supermodule hulls, the power bus bars and patch panels for  
261 the distribution of low voltage for the read-out boards and the cooling bars for the water cooling were  
262 mounted on the sidewalls. Next the power distribution box (DCS board power), the box for trigger signal

263 distribution, a patch panel for the optical read-out fibres, and the high-voltage distribution boxes were  
264 installed at the end-caps.

265 Before integrating the read-out chambers into a supermodule, they were equipped with electronics (read-  
266 out boards, DCS boards) and cooling pipes. After a series of tests were performed to ensure stable  
267 operation [56, 57], the chambers were then inserted layer by layer. The first connection established  
268 during the installation was the gas link between the chambers (using polyether ether ketone connectors).  
269 The chambers were fixed to the hull with three screws on each of the long sides after performing a manual  
270 physical alignment. As demonstrated by later measurements (Section 9), the alignment in  $r\phi$  between  
271 the chambers is of the order of 0.6–0.7 mm (r.m.s.).

272 The cables to and from the read-out boards used for JTAG, low-voltage sensing, Ethernet, and DCS  
273 power were routed along one side of the chambers. The cable lengths in the active area on top of the  
274 chambers were minimised, avoiding cables from the read-out pads to cross. On the other side of the  
275 chambers, only the high voltage cables were routed. They were soldered at two separate HV distribution  
276 boxes for anode and drift voltage at one end-cap of the supermodule. Each read-out board (38 per layer)  
277 was connected to the power bus bars (low voltage) using pre-mounted cables. The cooling pipes (4 per  
278 read-out board) were connected by small Viton tubes. In the  $z$ -direction across the read-out chambers,  
279 only optical fibres for the trigger distribution (1 per chamber) and data read-out (2 per chamber) were  
280 routed.

281 In addition to layer-wise tests during installation, a final test was done after completion. The test setup  
282 consisted of low-voltage and high-voltage supplies, a cooling plant, a gas system [58], as well as a full  
283 trigger setup and read-out equipment. Also a trigger for cosmic rays was built and installed [59, 60]. It  
284 was used for first measurements of the gas gain and the chamber alignment, and to also study the zero  
285 suppression during assembly [50, 61–65].

286 After transport to CERN pre-installation tests were performed (see Section 7.1 and [66]) and the su-  
287 permodules were installed in the space frame with a precision of 1 cm (r.m.s.) in  $z_{\text{lab}}$ -direction. The  
288 maximum tolerance in  $\phi$  is 2 cm due to constraints given by the space frame.

289 In addition to the sequential assembly and installation, four supermodules were completely disassembled  
290 again in 2008 and 2009. The initial tests were not sensitive to viscous leaks of the read-out chambers and  
291 thus the supermodules were rebuilt after improving the gas tightness (see Section 3.4.1). Furthermore, in  
292 2013 during LS 1, one supermodule was disassembled in order to improve the high-voltage stability of  
293 the read-out chambers (see Section 7.3).

## 294 2.4 Material budget

295 A precise knowledge of the material budget of the detector is important to obtain a precise description  
296 of the detector in the Monte Carlo simulations, which are used, e.g. to compute the track reconstruction  
297 efficiencies.

298 The TRD geometry, as implemented in the simulation part of AliRoot, consists of the read-out chambers,  
299 the services, and the supermodule frame. All these parts are placed inside the space frame volume. The  
300 material of a read-out chamber is obtained including several material components. A general overview  
301 of the various components is given in Table 2.

302 The material budget in the simulation was adjusted to match the estimate based on measurements during  
303 the construction phase of the final detector. The supermodule frames consist of the aluminium sheets on  
304 the sides, top, and bottom of a supermodule together with the traversing support structures, such as the  
305 LV power bus bars and cooling arteries. Additional electronics equipment is represented by aluminium  
306 boxes that contain the corresponding copper layers to mimic the present material. The services are also  
307 introduced, including, e.g. the gas distribution boxes, cooling pipes, power and read-out cables, and

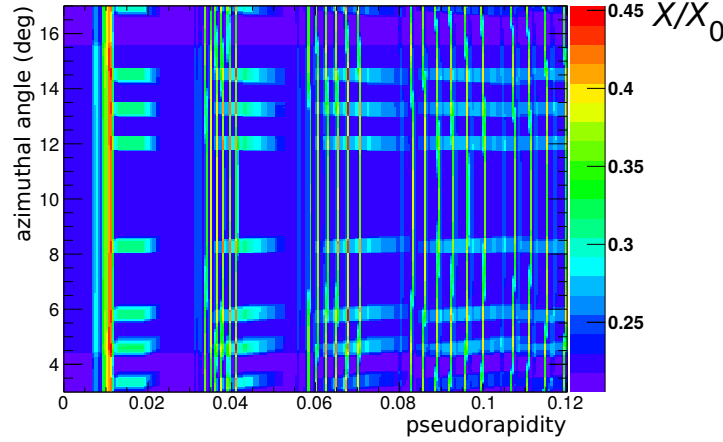


**Fig. 9:** The radiation length map in units of  $X/X_0$  in a zoomed-in part of the active detector area as a function of the pseudorapidity and the azimuthal angle, calculated from the geometry in AliRoot (the colour scale has a suppressed zero). The positions of the MCMs and the cooling pipes are visible as hot spots. The radiation length was calculated for particles originating from the collision vertex. Therefore the cooling pipes of the six layers overlap for small, but not large  $\eta$ .

Description	$X/X_0$ (%)
Radiator	0.69
Chamber gas and amplification region	0.21
Pad plane	0.77
Electronics (incl. honeycomb structure)	1.18
Total	2.85

**Table 2:** Parts of one read-out chamber, radiator, electronics, and their average contribution to the radiation length in the active area for particles with normal incidence.

308 power connection panels.

309 Figure 9 shows the resulting radiation length map, quantified in units of radiation length ( $X/X_0$ ), in a  
 310 zoomed-in part of the active detector area. It is clearly visible that the Multi-Chip Modules (MCM)s on  
 311 the read-out boards (see Section 5) and the cooling pipes introduce hot spots in  $X/X_0$ . After averaging  
 312 over the shown area, the mean value is found to be  $\langle X/X_0 \rangle = 24.7\%$  for a supermodule with aluminium  
 313 profiles and sheets and 30 read-out chambers (6 chambers per stack with the material budget as indicated  
 314 in Table 2). The reduced material budget of the supermodules in front of the PHOS detector (carbon  
 315 fibre inserts instead of aluminium sheets and no read-out chambers in stack 2) is likewise modelled in  
 316 the simulation. In regions directly in front of PHOS  $\langle X/X_0 \rangle$  is only 1.9%.

317 The total weight of a single fully equipped TRD supermodule as described in the AliRoot geometry,  
 318 including all services, is 1595 kg, which is about 3.3% less than its real weight. This discrepancy can  
 319 be attributed to material of service components, such as the gas manifold (see Section 3.3) and the patch  
 320 panel, outside the active area, which were not introduced in the AliRoot geometry.

### 321 3 Gas

322 At atmospheric pressure, a total of 27 m<sup>3</sup> of a xenon-based gas mixture must be circulated through the  
 323 TRD detector. This expensive gas cannot be flushed through, but rather has to be re-circulated in a closed  
 324 loop by using a compressor and independent pressure and flow regulation systems. The gas system of

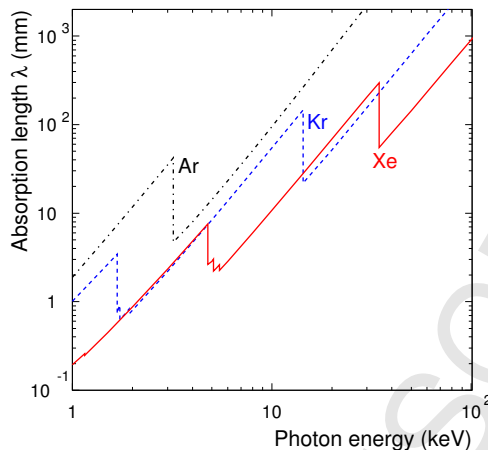


**Fig. 10:** Absorption length of X-rays in noble gases in the relevant energy range of TR production.

325 the TRD follows a pattern in construction, modularisation, control, and supervision which is common  
 326 to all LHC gaseous detectors, with emphasis on the regulation of a very small overpressure on the read-  
 327 out chambers and on the minimisation of leaks. The basic modules such as mixer, purification, pump,  
 328 exhaust, analysis, etc., are based on a set of equal templates applied to the hardware and the software.  
 329 A Programmable Logic Controller (PLC) controls each system and the user interacts with it through a  
 330 supervision panel. Upon a global command, the PLC executes a sequence that configures all elements of  
 331 the gas system for a given operation mode and continuously regulates the active elements of the system.  
 332 In this manner the modules and operational conditions can be customised to the specific requirements  
 333 of each detector, from the control of the stability of the overpressure in the detectors, the circulation  
 334 flow, and the gas purification, recuperation and distillation, to the monitoring of the gas composition and  
 335 quality (Xe-CO<sub>2</sub> (85-15), and as little O<sub>2</sub>, H<sub>2</sub>O and N<sub>2</sub> as possible).

### 336 3.1 Gas choice

337 As well as being an array of tracking drift chambers, the TRD is an electron identification device,  
 338 achieved through the detection of TR photons. In order to efficiently absorb these several keV pho-  
 339 tons, a high Z gas is necessary. Figure 10 shows, for three noble gases, the absorption length of photons  
 340 of energies in the range of typical TR production. At around 10 keV the absorption length in Xe is less  
 341 than a cm, whereas for Kr it is several cm. This argues for the choice of Xe as noble gas for the operating  
 342 mixture. CO<sub>2</sub> is selected as the quenching gas, since hydrocarbons are excluded for flammability and  
 343 ageing reasons. The choice of the exact composition is in this case rather flexible, since the design of the  
 344 wire chambers leaves enough freedom in the choice of the drift field and anode potential. The best com-  
 345 promise for the CO<sub>2</sub> concentration corresponds to the mixture Xe-CO<sub>2</sub> (85-15), which ensures a very  
 346 good efficiency of TR photon absorption by Xe and provides stability against discharges to the detector.

347 Furthermore, this mixture exhibits a nice stability of the drift velocity, at the nominal drift field, also  
 348 with the inevitable contamination of small amounts of N<sub>2</sub> that accumulates in the gas through leaks (see  
 349 Section 3.2). The drift velocity of the Xe-CO<sub>2</sub> (85-15) mixture, pure and with substantial admixtures  
 350 of N<sub>2</sub>, as a function of the drift field, is shown in Fig. 11 (left). The drift velocity does not depend on  
 351 the N<sub>2</sub> contamination at the nominal drift field of 700 V/cm. On the other hand, as illustrated in Fig. 11  
 352 (right), the anode voltage would need a 50 V readjustment to keep the gain constant when increasing  
 353 the concentration of N<sub>2</sub> by 10% in the mixture. It should be noted that intakes of less than 5% N<sub>2</sub>  
 354 are typically observed in one year of operation. After 2–3 years of operation, the N<sub>2</sub> is cryogenically  
 355 separated from the Xe (see Section 3.3.9).

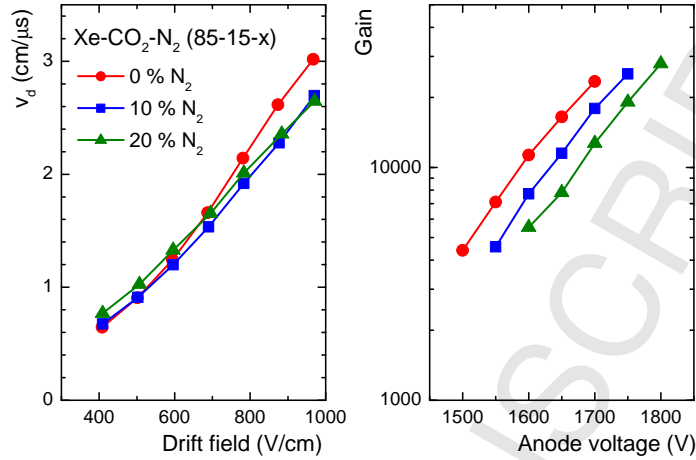


**Fig. 11:** Left: Drift velocity as a function of the drift field for the nominal gas mixture Xe-CO<sub>2</sub> and different admixtures of N<sub>2</sub>. Right: Gain as a function of the anode voltage for the same gas mixtures.

356 The operation of the chambers in a magnetic field of 0.5 T, perpendicular to the electric drift field  
 357 (700 V/cm), forces the drifting electrons on a trajectory, which is inclined with respect to the electric  
 358 field. The so-called Lorentz angle is about 9° for this gas mixture (see Section 10).

359 For commissioning purposes, where TR detection is not necessary, the read-out chambers are flushed  
 360 with Ar-CO<sub>2</sub> (82-18), which is available in a premixed form at low cost.

### 361 3.2 Requirements and specifications

362 The TRD consists of read-out chambers with an area of about 1 m<sup>2</sup> which are built with low material  
 363 budget. This poses a severe restriction on the maximum overpressure that the detector can hold. There-  
 364 fore, while in operation, the pressure of each supermodule is regulated by the gas system to a fraction  
 365 of a mbar above atmospheric pressure and the safety bubblers, installed close to the supermodules, are  
 366 adjusted to release gas at about 1.3 mbar overpressure. The detector can hold an overpressure in excess  
 367 of 5 mbar.

368 Another tight constraint arises from the highly disadvantageous surface-to-volume ratio of the detector,  
 369 which enhances the challenge of keeping the gas losses through leaks to a minimum. Cost considerations  
 370 drive the criterion for the maximum allowable leak rate of the system: a reasonable target is to lose less  
 371 than 10% of the total gas volume through leaks in one year. This translates into a total leak conductance  
 372 of 1 ml/h per supermodule at 0.1 mbar overpressure. As a result, unlike in other gas systems, gas is not  
 373 continuously vented out to the atmosphere. Furthermore, the filling and emptying of the system must be  
 374 performed with marginal losses of xenon. Adequate gas separation and cryogenic distillation techniques  
 375 are therefore implemented. Furthermore, any pulse-height measuring detector must be operated with a  
 376 gas free of electronegative substances, such as O<sub>2</sub>, which is continuously removed from the gas stream.  
 377 Precautions are taken by chromatographic analyses of both the supply xenon and of the air inside the  
 378 volume of the solenoid magnet to avoid any SF<sub>6</sub> contamination of the gas through gas supply cylinders  
 379 or from neighbouring detectors.

### 380 3.3 Description of the gas system

381 The TRD gas system follows the general architecture of all closed loop systems of the LHC detectors,  
 382 but is customised to meet the requirements specified above. The various modules of the gas system are

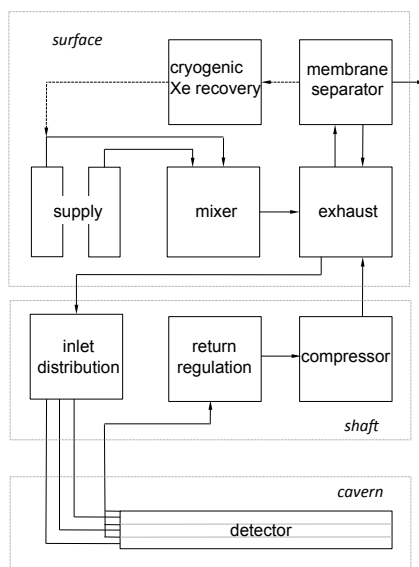


**Fig. 12:** Schematic view of the TRD gas system. The gas circulates in a closed loop pushed by a compressor. The flow for each supermodule is determined by the pressure set at individual pressure reducers in the inlet distribution modules. The overpressure is regulated with individual pneumatic valves at the return modules. The gas is purified at the surface and, when needed, supply gas is mixed and added to the loop. For the filling and the removing of the expensive xenon, semipermeable membranes are used to separate it from the CO<sub>2</sub>. The recovered xenon can be treated in a cryogenic plant in order to remove accumulated N<sub>2</sub>, prior to storage.

383 distributed, as shown schematically in Fig. 12, on the surface, in a location halfway down the cavern  
 384 shaft, and in the cavern. The gas is circulated by compressors that suck the gas from the detector and  
 385 compresses it to a high pressure value. This pumping action is regulated to keep the desired overpressure  
 386 at the detector. In the high-pressure part of the system, at the surface, gas purification, mixing, and other  
 387 operations are carried out. On its way to the cavern, the gas is distributed to individual supermodules  
 388 using pressure regulators. The gas circulates through the detector and at the outlet of each sector a gas  
 389 manifold is used to return the gas through a single line and to hold the pressure regulation hardware.  
 390 Halfway to the surface, a set of pneumatic valves is used to regulate the flow from each supermodule in  
 391 order to keep the desired overpressure. The gas is then compressed into a high pressure buffer prior to  
 392 circulation back to the surface.

### 393 3.3.1 Distribution

394 Xenon is a heavy gas; its standard condition density at ambient conditions is 5.76 kg/m<sup>3</sup>, 4.7 times that  
 395 of air. This means that over the 7 m height-span of the TRD in the experiment, the total hydrostatic  
 396 pressure difference between the top and the bottom supermodules would be about 2.8 mbar. In order  
 397 to overcome this, gas is circulated separately through each supermodule (except the top three and the  
 398 bottom three, which are installed at similar heights) and the pressure is thus individually regulated to  
 399 equal values everywhere. In addition, due to the different heights of the supermodules, the gas, supplied  
 400 from the surface, would flow unevenly through the different supermodules, the lower ones being favoured  
 401 over the higher ones. This second inconvenience is overcome by supplying the gas to each supermodule  
 402 from the distribution area (half way down the cavern shaft) through 4 mm thin lines over a length of  
 403 about 100 m. The pressure drop of the circulating gas in these lines, of several tens of mbar, is much  
 404 larger than the difference in hydrostatic pressure between supermodules, and therefore nearly equal flow,  
 405 at equal overpressure, is assured in all supermodules.

406 The six layers of the supermodules are supplied from one side (A-side) with three inlet lines, each



407 of them serving two consecutive layers. Small bypass bellows connect two consecutive layers on the  
408 opposite side. In the A-side, a manifold arrangement is used to connect the gas outlets and a common  
409 safety bubbler, pressure sensors and back-up gas. The return outlets in each supermodule are connected  
410 together into one line which returns to the pump module. The three top and three bottom supermodules  
411 are connected to one single return line each. This arrangement results into 14 independently regulated  
412 circulation loops. Each supermodule has its own two-way bubbler, which provides the ultimate safety  
413 against over- or underpressure.

### 414 3.3.2 Pump

415 In the distribution area, the flow through each return line is regulated by a pneumatic valve per loop  
416 driven by the pressure sensors located at the detector. In this area, the gas is kept at a pressure slightly  
417 below atmospheric pressure, and it is stored in a 0.8 m<sup>3</sup> buffer container before it is compressed by two  
418 pumps which operate at a constant frequency. The compressor module drives a bypass valve in order to  
419 maintain a calculated pressure set point at its inlet. In this manner, a dual regulation concept is used to  
420 handle the 14 loops. The role of the inlet buffer is to act as a damper of possible regulation oscillations.  
421 This pressure regulation system keeps the overpressure in the supermodule stable at 0.1 mbar above  
422 atmospheric pressure (set point) within 0.03 mbar.

423 A 0.93 m<sup>3</sup> high pressure buffer at the compressor outlet is used as a storage volume. Its content varies  
424 according to the atmospheric pressure, either by providing gas to the detectors, or by receiving it from  
425 them. The overpressure in this buffer typically ranges between 0.8 and 2 bar. Knowledge of all the  
426 system volumes allows the pressure in the buffer to be predicted for any atmospheric pressure value. Gas  
427 leaks ultimately result in a reduction of this pressure, in that case the dynamic regulation of the high  
428 pressure triggers the injection of fresh gas from the mixer until the high pressure is restored. From this  
429 buffer, the pressurised gas is circulated up to the gas building at the surface.

### 430 3.3.3 Purifier

431 The purifier module consists of two 3 litre cartridges each filled with a copper catalyser which is efficient  
432 in chemically removing oxygen by oxidising the copper, and mechanically removing water by absorption.  
433 Upon saturation, the PLC switches between cartridges at the pre-defined frequency, and launches an  
434 automatic regeneration cycle where CuO<sub>2</sub> is reduced at high temperatures with a flow of H<sub>2</sub> diluted in  
435 argon. As the detector is rather gas tight, the O<sub>2</sub> intake through leaks is moderate, and the purifier keeps  
436 it between 0 and 3 ppm. However, H<sub>2</sub>O diffusion, probably through the aluminised Mylar foil which  
437 constitutes the drift electrode of every read-out chamber, makes it necessary to switch between purifiers  
438 about every 3.5 days, in order to keep the H<sub>2</sub>O content below a few hundred ppm.

### 439 3.3.4 Recirculation

440 The surface module is used to recirculate the gas at high enough pressure to the distribution modules in  
441 the cavern shaft area. It also contains provisions for extracting gas samples for analysis, and a bypass loop  
442 to allow for the installation of containers such as a krypton source for gain calibration (see Section 10).

### 443 3.3.5 Mixer

444 Under normal operation and since the gas is only exhausted through leaks, gas injection into the system  
445 happens only if the pressure in the high pressure buffer falls below a dynamic threshold, as explained  
446 above. On such occasions, the mixer is activated and injects the nominal gas mixture at a rate of a few  
447 tens of l/h until the high pressure buffer is replenished. The amount of gas injected by the mixer during  
448 a given period provides a direct measurement of the leak rate.

449 In addition, a second set of mass flow controllers provides flows in the m<sup>3</sup>/h range and is used for filling  
450 and emptying the detector.

### 451 3.3.6 Backup system

452 When the gas system is in stop mode, e.g. when there is a power failure, the safety bubbler installed  
453 on each supermodule ensures that the detector pressure always remains within about  $\pm 1.3$  mbar relative  
454 to atmospheric pressure. In order to avoid that air, i.e. oxygen, enters the detector, the external side  
455 of the bubbler is connected to a continuous flow of neutral gas, in this case  $N_2$ , that flows through the  
456 bubbler in case of a large detector underpressure. The choice of  $N_2$  is driven by the small influence on  
457 the gas properties that this admixture has (see Fig. 11). The full TRD is served by three independent  
458 backup lines, each with connections to six supermodule bubblers, and arranged such that the flow points  
459 downwards. In this way, if the xenon mixture is exhausted through the bubblers, it falls down the back-  
460 up line, relieving its high hydrostatic pressure. A differential pressure transmitter measures the pressure  
461 difference between the detector and the backup gas.

### 462 3.3.7 Analysis

463 The control of the gas quality is perhaps the most demanding aspect of running detectors where both  
464 signal amplitude and drift time information are important. This control is even more crucial for the  
465 ALICE TRD, where accurate and uniform drift velocity and gain values are needed for triggers based  
466 on online tracking and particle identification. Thus, in addition to effective tightness of the system  
467 and continuous removal of  $O_2$  and  $H_2O$ , constant monitoring of the gas composition and in particular  
468 of the  $N_2$  is necessary. Although for a large volume system such as that of the TRD the changes in  
469 composition are obviously slow, the precision and stability requirement of the measuring instruments  
470 are quite challenging. Furthermore, constantly measuring analysers, such as  $O_2$ ,  $H_2O$  and  $CO_2$  sensors,  
471 must be installed in the gas loop, since xenon must not be exhausted. Therefore they must be free of  
472 outgassing of contaminants into the gas.

473 The analysis module samples the return gas from individual supermodules in a bypass mode, before it  
474 is compressed. For this, a fraction of the gas is pushed through the analysis chain by a small pump, and  
475 returned to the loop at the compressor inlet. Usually, the PLC is programmed to continuously sample  
476 one supermodule after the other, for about 10 minutes each.

477 An external gas chromatograph is used to periodically measure the gas composition. This device is not  
478 in the gas loop; rather, the gas is exhausted while purging and sampling a small stream for a few seconds  
479 every few hours.

### 480 3.3.8 Membranes

481 One system volume of xenon is injected for operation and, typically every two or three years, removed  
482 for cleaning and storage. This means that it must be possible to separate  $CO_2$  from Xe. This separation  
483 is achieved with a set of two semipermeable membrane cartridges. Each cartridge consists of a bundle  
484 of capillary polyimide tubes through which the mixture flows. The bundle is in turn enclosed in the  
485 cartridge case. While the  $CO_2$  permeates through the polyimide walls, most of the xenon is contained  
486 and continues to flow into the loop. The permeating gas can be circulated through the second membrane  
487 cartridge to further separate and recover most of the Xe.

488 During the filling, the detector is first flushed with  $CO_2$  and then, in closed-loop circulation, the xenon is  
489 injected as the  $CO_2$  is removed through the membranes. The reverse process is used for the recuperation  
490 of the xenon into a cryogenic plant.

### 491 3.3.9 Recuperation

492  $N_2$  inevitably builds up in the gas through small leaks and cannot be removed by the purifier cartridges.  
493 Therefore, after each long period (2–3 years) of operation, the  $N_2$  is cryogenically separated from the Xe.

494 A cryogenic buffer is filled with xenon after separating it from CO<sub>2</sub>. At the same time, CO<sub>2</sub> is injected  
495 into the gas system in order to replace the removed gas.

496 The cryogenically isolated buffer is surrounded by a serpentine pipe with a regulated flow of liquid  
497 nitrogen (LN<sub>2</sub>) in order to keep its temperature at  $-170\text{ }^{\circ}\text{C}$ , just above the N<sub>2</sub> boiling point ( $-195.8\text{ }^{\circ}\text{C}$ ).  
498 At this temperature Xe (and CO<sub>2</sub>) freezes whereas N<sub>2</sub> stays in the gaseous phase. Once the buffer is full,  
499 the stored gas is pumped away. After this, the buffer is heated up in a regulated way, and the evaporating  
500 Xe is compressed into normal gas cylinders. The resulting Xe has typically a N<sub>2</sub> contamination of  $<1\%$ ,  
501 and the total Xe loss (due to the efficiency of the membranes and the cryogenic recovery process) is about  
502  $1\text{ m}^3$  for a full recovery operation.

### 503 3.4 Operational challenges

504 The gas system has been operating reliably over several years in several modes, but mainly in so-called  
505 run mode. Aside from minor incidents, a number of important leaks have been dealt with, which deserve  
506 a brief description.

#### 507 3.4.1 Viscous leaks

508 As part of the standard quality assurance procedure, a leak test was performed on each chamber prior to  
509 installation in the supermodule. The leak test consisted of flushing the chamber with gas and measuring  
510 the O<sub>2</sub> contamination at the exhaust, where the overpressure was typically about 1 mbar. It was found,  
511 however, that a supermodule would lose gas even if the O<sub>2</sub> content was very low. The reason turned  
512 out to be the particular construction of the pad planes, which are glued to a reinforcement honeycomb  
513 panel with a carbon fibre sheet. Viscous leaks would develop between the glued surfaces and gas would  
514 find its way out through the cut-outs for the signal connections machined in the honeycomb sandwich.  
515 The impedance of this kind of leak is large enough that gas can escape the detector with no intake of  
516 air through back-diffusion. The concerned read-out chambers were then extracted and repaired, and  
517 the leak tests on subsequent chambers were modified such that the O<sub>2</sub> was measured both at over- and  
518 underpressure in the read-out chamber, resulting in a tight system.

#### 519 3.4.2 Argon contamination

520 At one point, the routine gas analysis with the gas chromatograph showed increasing levels of Ar in the  
521 Xe-CO<sub>2</sub> mixture. This elusive leak came from a faulty pressure regulator which was pressurised with  
522 argon on the atmospheric side. Occasionally, depending on the pressure, the membrane of the regulator  
523 would leak and let Ar enter the gas volume. A total of 1% Ar accumulated in the mixture and was  
524 removed by cryogenic distillation, together with N<sub>2</sub>.

#### 525 3.4.3 Leak in pipe

526 The last major leak in the system was detected when suddenly the pressure at the high pressure buffer  
527 started to steadily decrease. Any leak of the system would appear, while running, as a decrease in the  
528 high pressure buffer, because the system always ensures the right overpressure at the read-out chambers.  
529 By stopping the system and isolating all of its modules, it was found that the source of the leak was a  
530 long, stainless steel pipe which connected the compressor module, half way down the cavern shaft, to  
531 the surface, where the gas, still at high pressure, is cleaned and recirculated. It was not possible to find  
532 the exact location of the leak. This was solved by replacing the pipe by a spare.

## 533 4 Services

534 The supermodules installed in the space frame require service infrastructure for their operation. To  
535 reduce the weight, the connections (low and high voltage, cooling, gas, read-out, and control lines) are

Channel	$U_{\text{nom}}$ (V)	$I_{\text{typ}}$ (A)
3 x Analogue 1.8 V	2.5	125
3 x Analogue 3.3 V	4.0	107
3 x Digital 1.8 V	2.5	95–150
Digital 3.3 V	4.0	110
DCS boards	4.0	$2 \times 30$

**Table 3:** Number of low voltage channels, nominal voltages and typical currents for the electronics on the chamber-mounted read-out boards of one supermodule. The current for the TRAP cores (digital 1.8 V) increases with the trigger rates. The current for the DCS boards is  $2 \times 30$  A for two adjacent sectors.

536 routed via dedicated frames on the A- and C-side, respectively. Both frames are 2 m extensions of the  
 537 space frame with similar geometry, but mechanically independent except for the flexible services. Most  
 538 of the equipment, such as the low-voltage power supplies, is placed in the cavern underground and thus  
 539 inaccessible during beam operation. Some devices are situated in counting rooms in the cavern shaft,  
 540 which are supervised radiation areas but accessible.

#### 541 4.1 Low voltage

542 The low voltage system supplies power to various components of the TRD. The largest consumer is  
 543 the Front-End Electronics (FEE), i.e. the electronics of the Read-Out Boards (ROB) mounted on the  
 544 chamber (see Section 5). To minimise noise, separate (floating) voltage rails are used for analogue and  
 545 digital components. The power supply channels for analogue 1.8 V, analogue 3.3 V, and digital 1.8 V  
 546 are grouped such that one power supply channel supplies two layers of a supermodule. For the digital  
 547 3.3 V there is one channel per supermodule. For each supermodule, this results in the supply channels  
 548 listed in Table 3. The DCS boards (see Section 4.4) are powered by a power distribution box (PDB), two  
 549 of which (in two adjacent supermodules) are supplied by a dedicated channel. The PDBs are controlled  
 550 by Power Control Units (PCU) over a redundant serial interface.

551 Because of the high currents, the intrinsic resistances of the cables and connections are critical and are  
 552 constantly monitored by measuring the voltage drop between the power supply unit (terminal voltage)  
 553 and the patch panel at each supermodule (sense voltage). Typical values are 6–8 m $\Omega$ , depending on the  
 554 cable length. In addition, the voltages at the end of each power bus bar are monitored.

555 The Global Tracking Unit (GTU) (see Section 5.3) uses additional power supplies which are shared with  
 556 the PCUs. The pretrigger system (see Section 5.1) is powered by separate power supplies, laid out in a  
 557 fail-safe redundant architecture.

558 Different customizations of the Wiener PL512 power supply units are used. The power supplies feeding  
 559 the FEE are connected to a PLC-based interlock based on the status of the cooling. Power is automatically  
 560 cut in case of a cooling failure.

561 During the RUN 1 operation, several low-voltage connections on the supermodules showed increased  
 562 resistivity resulting in excessive heat dissipation, which in some cases required to switch off part of the  
 563 detector until the problem could be fixed during an access. Later, during LS 1, the affected supermodules  
 564 were pulled out of the experiment and the connections were reworked in the cavern. The supermodules  
 565 were re-inserted and re-commissioned immediately after the rework. The complete procedure took about  
 566 one day per supermodule.

#### 567 4.2 Cooling

568 The complexity of the cooling system, whose cooling medium is deionised water, is driven by the large  
 569 amount of heat sources (more than 100000) distributed over the complete active area of the detector. Heat  
 570 is produced by the MCMs and the Voltage Regulators (VR) on the read-out boards, the DCS boards, and  
 571 the power bars. The total heat dissipation in a supermodule amounts to about 3.3 kW, of which about

572 2.6 kW are produced in the FEE, the remaining 700 W originate from the voltage regulators and the bus  
573 bars. The DCS boards contribute with about 130 W per supermodule. Overall, the rate of heat to be  
574 carried away during detector operation amounts to 55 kW and 70 kW in Pb–Pb and pp collisions, respec-  
575 tively, due to different read-out rates. Apart from the power bus bars, the heat sources are positioned on  
576 top of the read-out boards.

577 In the cooling system the pressure is kept below atmospheric pressure. Thus a leak leads to air entering  
578 in the system but no water is spilled onto the detector. The cooling plant [67] consists of a 1500 l storage  
579 tank positioned at the lowest point outside the solenoid magnet, which is able to contain all the water of  
580 the installation, the circulation pump, the 18 individual circuits that supply cooling water to the 6 layers of  
581 each supermodule, and the heat exchanger connected to the CERN chilled water network. The reservoir  
582 is kept at 300–350 mbar below atmospheric pressure by means of a vacuum pump that also removes  
583 any air collected through small leaks. In addition, the pressure of the circulation pump (1.8 bar) and the  
584 diameter of all pipes are chosen such that a sub-atmospheric pressure is maintained in all places of the  
585 detector, despite a difference in height of about 7 m between the lowest and the highest supermodule.  
586 Each circuit is equipped with individual heaters and balancing valves in order to control the temperature  
587 and the flow in each loop separately. The heaters are regulated by a proportional-integral-derivative  
588 controller. A temperature stability in the cooling water of  $\pm 0.2^\circ\text{C}$  is achieved. The typical water flow  
589 is about 1300 l/h per supermodule. To avoid corrosion a fraction of the total water flow is passed by a  
590 deioniser to keep the water conductivity low. As the water is in contact with similar materials (stainless  
591 steel and aluminium), the TRD cooling system also supplies the water to the cooling panels of the thermal  
592 screening between TPC and TRD [31].

593 The loop regulations and cooling plant control is done by a PLC. Warnings and alarms are issued by  
594 the PLC if the parameters are outside the allowed intervals and read out by the Detector Control System  
595 (see Section 6). Two independent security levels were implemented in each loop. The first continuously  
596 monitors the pressure of each loop and stops the water circulation of the cooling plant if any value reaches  
597 atmospheric pressure. Secondly, large safety valves were installed at the entrance to each supermodule.  
598 They will open in case an overpressure of 50 mbar is reached, providing a low resistance path for the  
599 water evacuation in case of emergency.

600 The cold water is supplied in the lowest point of each supermodule and the warm water is collected on  
601 the highest point in order to have more homogeneous water flow in all pipes. A water manifold at one  
602 end-cap of the supermodule distributes the water in parallel to the 6 layers inside each supermodule, and  
603 on the opposite side a similar manifold collects the warm water. In each layer, two rectangular pipes  
604 along the  $z$ -direction ( $65 \times 8 \times 7500$  mm) supply (collect) water to (from) the meanders, 76 individual  
605 cylindrical aluminium pipes (3 mm in diameter) running across the  $y$ -direction where the heat sources  
606 are. A total of 17 meander types were designed for the system. To bring the water from the rectangular  
607 pipes to the individual meanders, the rectangular pipe has small stainless steel pipes (3 mm diameter and  
608 5 cm length) soldered at the proper position for each MCM row. A Viton tube of about 2 cm length is  
609 used to connect the small stainless steel pipes and the meanders as well as for the connections between  
610 the two meanders (one per ROB) in  $y$ -direction. A total of about 25000 Viton tube connectors were used  
611 in the system. This kind of connector was previously used in the CERES/NA45 leakless cooling system  
612 [68] because of its low price and reliability.

613 The cooling pad mounted on top of the heat source consists of an 0.4 mm thick aluminium plate. The  
614 meander is glued on top of the pad by aluminium-filled epoxy (aluminium powder: Araldite<sup>®</sup> 130:100  
615 by weight) to increase the thermal conductivity. In order to maximise the heat transfer, the longest  
616 possible path was chosen. The choice of aluminium was driven by the necessity of keeping the material  
617 budget as low as possible in the active area of the detector.

### 618 4.3 High voltage

619 The high voltage distribution for the drift field and the anode-wire plane is made separately for each  
620 chamber, reducing the affected area to one chamber in case of failure. The power supplies for the  
621 drift channels and anode-wires were purchased from ISEG [69] (variants of the model EDS 20025).  
622 Each module has 32 channels, which are grouped in independent 16-channel boards. Each channel is  
623 independently controllable in terms of the voltage setting and current limit as well as monitoring of  
624 current and voltage. Eight modules are placed into each crate and remotely controlled via CANbus  
625 (Controller Area Network) from DCS (see Section 6). The HV crates are placed in one of the counting  
626 rooms in the cavern shaft, which allows access even during beam operation.

627 For each of the 30 read-out chambers in a supermodule one power supply is needed for the drift field  
628 and one for the anode-wire plane. A multiwire HV cable connects the 32 channel HV module with  
629 a 30 channel HV fanout box (patch box) located at one end of the supermodule, where the output is  
630 redistributed to single wire HV cables (see Section 2.3). The individual HV cables are then connected to  
631 a HV filter box, mounted along the side of the read-out chamber. The HV filter box supplies the HV to  
632 the 6 anode segments and the drift cathode of the read-out chamber, and in addition it allows connection  
633 of the HV ground to the chamber ground. It consists of a network of a resistor and capacitors (2.2 nF and  
634 4.7 nF) to suppress load-induced fluctuations of the voltages in the chamber.

635 The HV crates are equipped with an Uninterruptible Power Supply (UPS) and a battery to bridge short  
636 term power failures. In case of a longer power failure ( $> 10$  s) a controlled ramp-down is initiated, i.e.  
637 the HV of the individual drift and anode-wire channels is slowly ramped down. Details on maximum  
638 applied voltages, channel equalisation, ramp speed as well as high-voltage instability observed during  
639 data taking are discussed in Sections 6 and 7.3.

### 640 4.4 Slow control network

641 The slow control of the TRD is based on Detector Control Systemboards [70]. They communicate  
642 with the DCS (see Section 6) by a 10 Mbit/s Ethernet interface, mostly using Distributed Information  
643 Management (DIM) as protocol for information exchange. The use of Ethernet allows the use of standard  
644 network equipment, but a dedicated network restricted to the ALICE site is used. The DCS boards are  
645 used as end points for the DCS to interact with subsystems of the detector. Later sections will discuss  
646 how the DCS boards are used as interface to the various components, e.g. the front-end electronics or the  
647 GTU.

648 The DCS boards were specifically designed for the control of the detector components and are used  
649 by several detectors in ALICE. At the core, the board hosts an Altera Excalibur EPXA1 (ARMv4 core  
650 + FPGA), which hosts a Linux operating system on the processor and user logic in the FPGA fabric  
651 depending on the specific usage of the board. The DCS board also contains the Trigger and Timing  
652 Control receiver (TTCrx) for clock recovery and trigger reception. The Ethernet interface is implemented  
653 with a hardware PHY (physical layer) and a soft-Media Access Controller (MAC) in the FPGA fabric.  
654 In case of the boards mounted on the detector chambers, the FPGA also contains the Slow Control Serial  
655 Network (SCSN) master used to configure the front-end electronics. Further general purpose I/O lines  
656 are, e.g. used for JTAG and I<sup>2</sup>C communication.

657 Since the Ethernet connections are used for configuration and monitoring of the detector components,  
658 reliable operation is crucial. All DCS boards are connected to standard Ethernet switches installed in the  
659 experimental cavern outside of the solenoid magnet. Because of the stray magnetic field and the special  
660 Ethernet interface of the DCS board (no inductive coupling), there are limitations on the usable switches.  
661 Since the failure of an individual switch would result in the loss of connectivity to a large number of DCS  
662 boards, a custom-designed Ethernet multiplexer was installed in front of the switches in the second half  
663 of RUN 1. This allows the connection of each DCS board to be remotely switched between two different

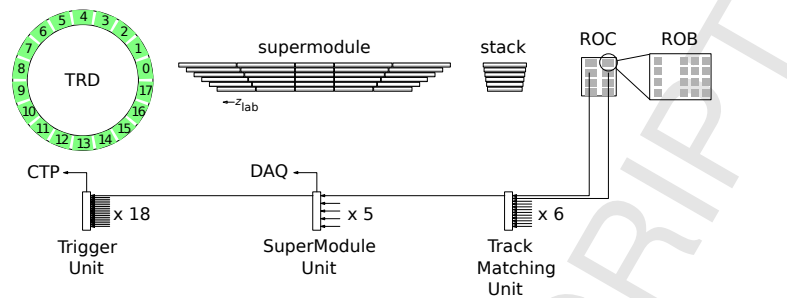


**Fig. 13:** Detector structures and corresponding read-out stages [71]. The top row of the figure represents the detector and the bottom row the GTU components. The dimensions are not to scale.

664 switches with separate uplinks to the DCS network. The multiplexers themselves are implemented with  
 665 fully redundant power supplies and control interfaces.

## 666 5 Read-out

667 The read-out chain transfers both raw data and condensed information for the level-1 trigger. While the  
 668 former requires sufficient bandwidth to minimise dead time, the latter depends on a low latency, i.e. a  
 669 short delay of the transmission. The data from the detector are processed in a highly parallelised read-out  
 670 tree. Figure 13 provides an overview and relates entities of the read-out system to detector components.  
 671 In the detector-mounted front-end electronics, the data are processed in Multi-Chip Modules grouped on  
 672 Read-Out Boards (ROB) and eventually merged per half-chamber. Then, they are transmitted optically  
 673 to the Track Matching Units (TMU) as the first stage of the Global Tracking Unit (GTU). The data from  
 674 all stacks of a supermodule are combined on the SuperModule Unit (SMU) and eventually sent to the  
 675 Data Acquisition system (DAQ) through one Detector Data Link (DDL) per supermodule.

676 The read-out of the detector is controlled by trigger signals distributed to both the FEE and the GTU. The  
 677 ALICE trigger system is based on three hardware-level triggers (level-0, 1, 2) and a High Level Trigger  
 678 (HLT) [72] implemented as a computing farm. In addition to these levels, the FEE requires a dedicated  
 679 wake-up signal as described in the next subsection.

### 680 5.1 Pretrigger and LM system

681 Both FEE and GTU must receive clock and trigger signals, which are provided by the Central Trigger  
 682 Processor (CTP) [73] using the Trigger and Timing Control (TTC) protocol over optical fibres. While  
 683 the GTU only needs the level-0/1/2 and is directly connected to the CTP, the FEE requires a more com-  
 684 plicated setup. To reduce power consumption, it remains in a sleep mode when idle and requires a fast  
 685 wake-up signal before the reception of a level-0 trigger to start the processing. During RUN 1, an in-  
 686 termediate pretrigger system was installed within the solenoid magnet [74, 75]. Besides passing on the  
 687 clock and triggers received from the CTP, it generated the wake-up signal from copies of the analogue  
 688 V0 and T0 signals (reproducing the level-0 condition) and distributed it to the front-end electronics. In  
 689 addition, the signals from TOF were used to generate a pretrigger and level-0 trigger on cosmic rays.  
 690 Because of limitations of this setup, the latencies of the contributing trigger detectors at the CTP were  
 691 reduced for RUN 2 (also by relocating the respective detector electronics) such that the functionality of  
 692 the pretrigger system could be integrated into the CTP. The latter now issues an LM (level minus 1)  
 693 trigger for the TRD before the level-0 trigger. An interface unit (LTU-T) was developed for protocol  
 694 conversion [76] in order to meet the requirements of the TRD front-end electronics. A comparison of  
 695 the two designs is shown in Fig. 14. The new system has been used since the beginning of collision data  
 696 taking in RUN 2.

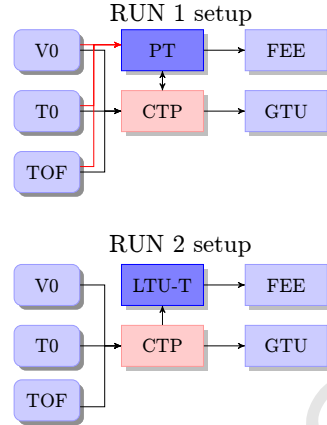


**Fig. 14:** In RUN 1, the wake-up signal required for the front-end electronics was generated by a dedicated pretrigger system. In RUN 2, the functionality was implemented in the central trigger processor and the LTU-T serves as an interface to the TRD FEE.

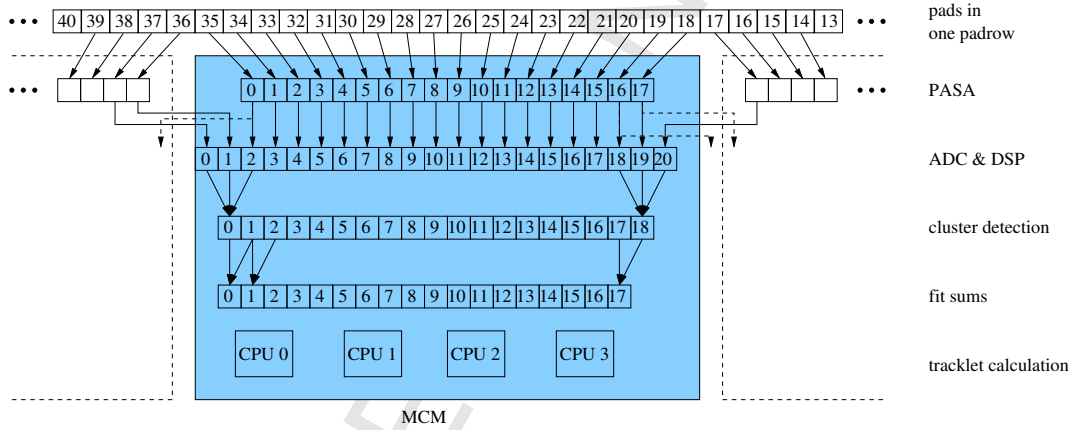


**Fig. 15:** Connections in one MCM [66].

## 697 5.2 Front-end electronics

698 The FEE is mounted on the back-side of the read-out chamber. It consists of MCMs which are connected  
 699 to the pads of the cathode plane with flexible flat cables. An MCM comprises two ASICs, a PASA and a  
 700 TRAP, which feature a large number of configuration settings to adapt to changing operating conditions.  
 701 The signals from 18 pads are connected to the charge-sensitive inputs of the PASA on one MCM. An  
 702 overview of the connections is shown in Fig. 15.

703 The very small charges induced on the read-out pads (typically  $7\ \mu\text{A}$  during  $1\ \text{ns}$ ) are not amenable to  
 704 direct signal processing. Therefore, the signal is first integrated and amplified by a Charge Sensitive  
 705 Amplifier (CSA). Its output is a voltage signal with an amplitude proportional to the total charge. The  
 706 CSA has a relatively long decay time, which makes it vulnerable to pile-up. A differentiator stage re-  
 707 moves the low frequency part of the pulse. The exponential decay of the CSA feedback network, in  
 708 combination with the differentiator network, leads to an undershoot at the shaper output with the same  
 709 time constant as the CSA feedback network. A Pole-Zero network is used to suppress the undershoot.  
 710 A shaper network is required to limit the bandwidth of the output signal and avoid aliasing in the subse-  
 711 quent digitisation process. At the same time the overall signal-to-noise ratio must be optimised. These



Parameter	Value
PASA gain	12 mV/fC
PASA power	15 mW/channel
PASA pulse width (FWHM)	116 ns
PASA noise (equivalent charge)	1000 e
TRAP power	12.5 mW/channel
TRAP ADC depth	10 bit
TRAP sampling frequency	10 MHz

**Table 4:** Achieved PASA and TRAP characteristics.

712 objectives are achieved by a semi-Gaussian shaper, implemented with two low-pass filter stages. Each  
 713 stage consists of two second-order bridged-T filters connected in cascade. The second shaper consists of  
 714 a fully differential amplifier with a folded cascode configuration and a common-mode feedback circuit.  
 715 This circuit network was implemented to prevent the output of the fully differential amplifier from drifting  
 716 to either of the two supply voltages. It establishes a stable common-mode voltage. The last stage in  
 717 the chain comprises a pseudo-differential amplifier with a gain of 2. This stage adapts the DC voltage  
 718 level of the PASA output to the input DC-level of the TRAP ADC [77].

719 The differential PASA outputs are fed into the ADCs of the TRAP, the second ASIC on the same MCM.  
 720 The PASA and TRAP parameters are listed in Table 4. The TRAP is a custom-designed digital chip  
 721 produced in the UMC 0.18  $\mu\text{m}$  process. The TRAP comprises cycling 10-bit ADCs for 21 channels, a  
 722 digital filter chain, a hardware preprocessor, four two-stage pipelined CPUs with individual single-port,  
 723 Hamming-protected instruction memories (IMEM, 4k x 24 bit), about 400 configuration registers usable  
 724 by the hardware components, a quad-port Hamming-protected data memory (DMEM, 1k x 32 bit), and  
 725 an arbitrated Hamming-protected data bank (DBANK, 256 x 32 bit) [78]. Three excess ADC channels  
 726 are fed with the amplified analogue signal from the two adjacent MCMs to avoid tracking inefficiencies  
 727 at the MCM boundaries. The signals of all 21 channels are sampled and processed in time bins of 100 ns.  
 728 The number of time bins to be read out, can be configured in the FEE. At the beginning of RUN 1 24 time  
 729 bins were conservatively read out. At a later stage the number of time bins was reduced to 22 in order to  
 730 reduce the readout time and the data volume.

731 The first step in the TRAP is the digitisation of the incoming analogue signals. In order to avoid rounding  
 732 effects, the ADC outputs are extended by two binary digits and fed into the digital filter chain. First, the  
 733 pedestal of the signal is equilibrated to a configurable value. Then, a gain filter is used to correct for  
 734 local variations of the gain, arising either from detector imperfections or the electronics themselves. A  
 735 tail cancellation filter can be used to suppress the ion tails. The filtered data are fed into a pre-processor  
 736 which contains hardware units for the cluster finding. The four CPUs (MIMD architecture) are used for  
 737 the further processing. The local tracking procedure is discussed in detail in Section 12.1.

738 The MCMs are mounted on the ROB. On each board, 16 chips are used to sample and process the  
 739 detector signals. A full detector chamber is covered by 8 ROBs (6 for chambers in stack 2). The read-out  
 740 is organised in a multi-level tree. First, the data from four chips are collected by so-called column merger  
 741 chips. The latter, in addition to processing the data from their own inputs, receive the data from three  
 742 more MCMs. The data are merged and forwarded to the board merger, which combines the data from all  
 743 chips of one ROB. One ROB per half-chamber carries an additional MCM which acts as half-chamber  
 744 merger (without processing data of its own). It forwards the data to the Optical Read-out Interface (ORI)  
 745 from where it is transmitted through an optical link (DDL) to the GTU. The link is operated at 2.5 Gbit/s  
 746 and is implemented for uni-directional transmission without handshaking, i.e. the receiving side must  
 747 be able to handle the incoming data for a complete event as it arrives. As the FEE does not provide  
 748 multi-event buffering, the detector is busy until the transmission from the FEE is finished. The slowest  
 749 half-chamber determines the contribution to the dead time of the full detector.

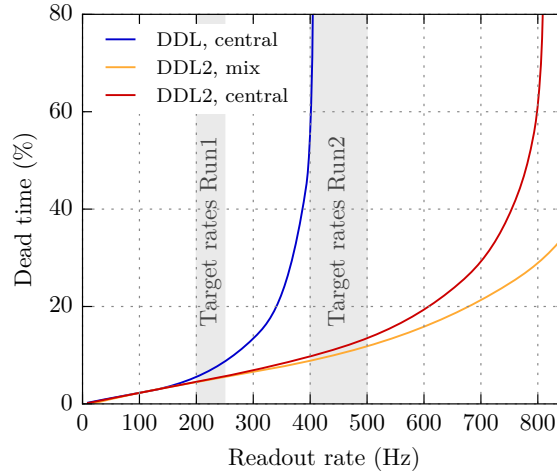


**Fig. 16:** Simulation of the dead time as function of the read-out rate in Pb–Pb collisions for the effective DDL bandwidth in RUN 1 (DDL) and RUN 2 (DDL2). The simulation assumes a 5% L1/L0 accept ratio and no L2 rejects. The scenarios central and mix correspond to an event size of 470 kB and 310 kB per supermodule, respectively, mimicking thus different event multiplicities.

### 750 5.3 Global Tracking Unit

751 The GTU receives data via 1044 links from the FEE. The aggregate net bandwidth amounts to 261 GB/s.  
 752 The two main tasks of the GTU are the calculation of level-1 trigger contributions from a large number  
 753 of track properties in about  $2\ \mu\text{s}$  and the preparation of the event data for read-out. Accordingly, the  
 754 data processing on the GTU features a trigger path, which is optimised for low latency, and a data path,  
 755 which equips the detector with the capability to buffer up to 4 events (multi-event buffering, MEB). The  
 756 derandomisation of the incoming data rate fluctuations with multiple event buffers minimises the read-  
 757 out related dead time. The data transfer from the GTU to the DAQ contributes to the dead time only  
 758 when the read-out rate approaches the rate which saturates the output bandwidth as shown in Fig. 16.

759 The GTU consists of three types of FPGA-based processing nodes organised in a three-layer hierarchy  
 760 (see Fig. 17). The central component of all nodes is a Virtex-4<sup>©</sup> FX100 FPGA, supplemented by a  
 761 4 MB source-synchronous DDR-SRAM, 64 MB DDR2-SDRAM and optical transceivers. Depending  
 762 on the type, the nodes are equipped with different optical parts and supplementary modules. 90 TMUs  
 763 and 18 SMUs are organised in 18 segments of 5+1 nodes (corresponding to the 18 sectors). The TMUs  
 764 and SMU of a segment are interconnected using a custom LVDS backplane, which is optimised for high-  
 765 bandwidth transmissions at low latency. A single top-level Trigger Unit (TGU) is connected to the SMUs  
 766 of the individual segments via LVDS transmission lines.

767 The data from one stack is received by the corresponding TMU. Each TMU implements the global online  
 768 tracking, which combines pre-processed track segments to tracks traversing the corresponding detector  
 769 stack, as first stage of the trigger processing (see Section 12). The TMUs furthermore implement the  
 770 initial handling and buffering of incoming events as a pipelined data push architecture. Input shaper  
 771 units monitor the structural integrity of the incoming data and potentially restore it to a form that allows  
 772 for stable operation of all downstream entities. Dual-port, dual-clock BRAMs in the FPGA are utilised  
 773 to compactify data of the 12 incoming link data streams to dense, wide lines suitable for storage in the  
 774 SRAM. The SRAM provides buffer space for multiple events and its controller implements the required  
 775 write-over-read prioritisation to ensure that data can be handled at full receiver bandwidth. On the read  
 776 side, a convenient interface is provided to read out or discard stored events in accordance to the control  
 777 signals generated by the segment control on the SMU.

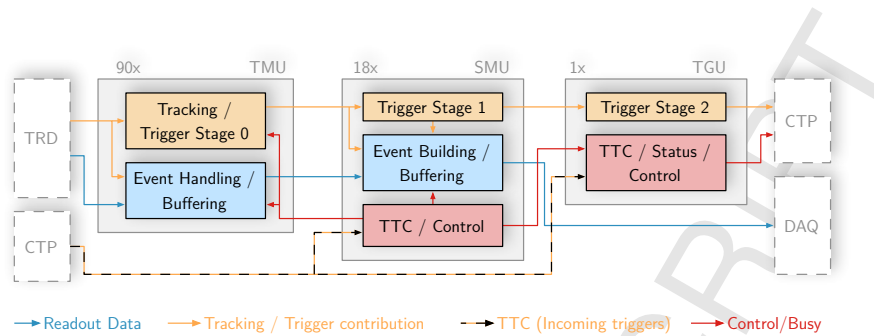


**Fig. 17:** Major design blocks of the TMU and SMU stages of the GTU and data flow. The busy and trigger logic information are combined on the TGU before transmission to the CTP.

778 Via its DCS board the SMU receives relayed trigger data issued by the CTP to synchronise the operation  
 779 of the experiment. The trigger sequences are decoded, and converted to suitable control signals and  
 780 time frames to steer the operation of the segment. The segment control on the SMU supports operation  
 781 with multiple, interlaced trigger sequences in order to support the concurrent handling and buffering of  
 782 multiple events. Upon reception of a level-2 trigger, the SMU requests the corresponding event data  
 783 from the event buffers and initiates the building of the event fragment for read-out. The built fragment  
 784 contains, in addition to the data originating from the detector, intermediate and final results from tracking  
 785 and triggering relevant for offline verification, as well as checksums to quickly assess its integrity. The  
 786 SMU implements the read-out interface to the DAQ/HLT with one DDL. The endpoint of the DDL is a  
 787 Source Interface Unit (SIU), which in RUN 1 was a dedicated add-on card mounted on the SMU backside  
 788 that operates at a line rate of 2.125 Gbit/s. The read-out upgrade for RUN 2 integrates the functionality  
 789 of the SIU into the SMU FPGA and employs a previously unused transceiver on the SMU at a line rate  
 790 of 4 Gbit/s. The elimination of the interface between SMU and SIU add-on card, the higher line rate  
 791 as well as data path optimisations resulted in an increase of the effective DDL output bandwidth from  
 792 189 MB/s to 370 MB/s in RUN 2. Figure 16 illustrates the performance improvement for the assumed  
 793 data taking scenarios. With the upgrade the read-out-related dead time can be kept at an acceptable level.  
 794 The almost linear increase at low rates is due to the dead time associated with the L0–L1 interval and the  
 795 FEE-GTU transmission. The typical aggregate output bandwidth for all 18 supermodules is 126 MB/s,  
 796 202 MB/s, and 1260 MB/s in pp, p–Pb, and Pb–Pb collisions (see also Section 7.3).

797 The top-level TGU consolidates the status of the segments, which operate independently in terms of  
 798 read-out, as well as the segment-level contributions of the triggers. It constitutes the interface to the CTP,  
 799 to which it communicates the detector busy status and the TRD-global trigger contributes for various  
 800 signatures (see Section 12).

## 801 6 Detector Control System

802 The purpose of the DCS is to ensure safe detector conditions, to allow fail-safe, reliable and consis-  
 803 tent monitoring and control of the detector, and to provide calibration data for offline reconstruction. In  
 804 addition it provides detailed information on subsystem conditions and full functionality for expert moni-  
 805 toring and detector operation. Tools were implemented to reduce the operational complexity and the  
 806 information on detector conditions to a level that allows operators to monitor and handle the detector  
 807 in an intuitive and safe way. The TRD DCS is integrated with the rest of the ALICE detector control  
 808 systems into one system which is operated by one operator.

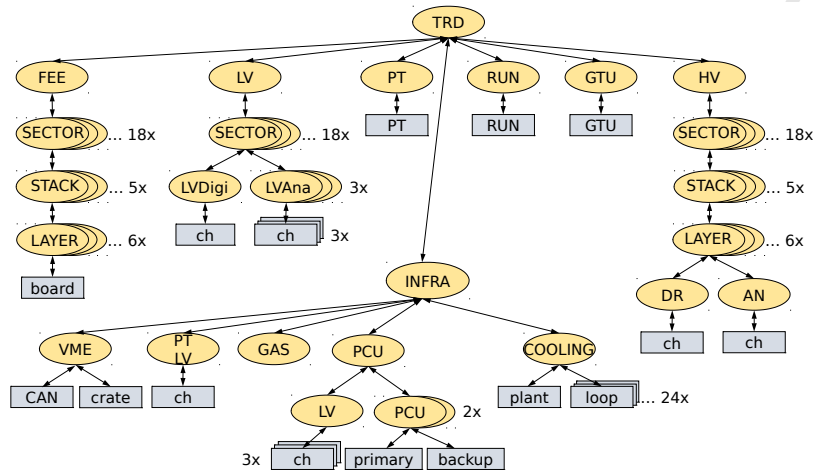


**Fig. 18:** Overview of the DCS software architecture. The tree structure consists of device units (boxes) and logical control units (ellipses). The abbreviations PT, DR and AN correspond to the pretrigger, the drift and anode channels, respectively.

## 809 6.1 Architecture

810 The hardware architecture of the DCS can be divided into three functional layers. The field layer contains  
 811 the actual hardware to be controlled (power supplies, FEE, etc). The control layer consists of devices  
 812 which collect and process information from the field layer and make it available to the supervisory layer.  
 813 Finally, the devices of the control layer receive and process commands from the supervisory layer and  
 814 distribute them to the field layer.

815 The software on the supervisory layer is distributed over 11 server computers. It is based on the commer-  
 816 cial Supervisory Control and Data Acquisition (SCADA) system PVSS II from the company ETM [79],  
 817 now called Symatic WinCC [80]. The implementation uses the CERN JCOP control framework [81],  
 818 shared by all major LHC experiments. This framework provides high flexibility and allows for easy in-  
 819 tegration of separately developed components in combination with dedicated software developed for the  
 820 TRD, including Linux-based processes.

821 The software architecture is a tree structure that represents (sub-)systems of the detector and its devices,  
 822 as shown in Fig. 18. The entities at the bottom of the hierarchy represent the devices (device units),  
 823 logical entities are represented by control units. The DCS system monitors and controls 89 low voltage  
 824 (LV) power supplies with more than 200 channels, and 1044 high voltage channels. The system also  
 825 monitors the electronics configuration of more than one million read-out channels, the GTU, and the  
 826 cooling and gas systems.

## 827 6.2 Detector safety

828 To ensure the safety of the equipment, nominal operating conditions are maintained by a hierarchical  
 829 structure of alerts and interlocks. Whenever applicable, internal mechanisms of devices (e.g. power  
 830 supply trip) are used to guarantee the highest level of reliability and security. Thresholds and status  
 831 of the interlocks are controlled by the system, but the functioning of the device is independent of the  
 832 communication between hardware and software. The possible range of applied settings (e.g. anode  
 833 channel high voltage) is limited to a nominal range to prevent potential damage due to operator errors.

834 In addition, the system employs a three-level alert system, which is used to warn operators and detector  
 835 experts of any unusual detector condition.

836 On the control and supervisory layer, cross system interlocks protect the devices and ensure consistent  
837 detector operation. These are a few examples:

- 838 – In case of a failure of the cooling plant for the FEE, a PLC-based interlock disables the LV power  
839 supplies.
- 840 – The temperature of the FEE is monitored at the control and supervisory level and interlocked with  
841 the PCU to switch off the devices in case of overheating or loss of communication to the SCADA  
842 system.
- 843 – In case of a single LV channel trip, the corresponding FEE channels are consistently switched off.
- 844 – Unstable LHC beam conditions, e.g. during injection or adjustment of the beam optics, pose a  
845 potential danger to gas-filled detectors. Therefore the HV settings are adapted to the LHC status  
846 (see Section 7.2). At injection, the anode voltages are decreased automatically to an intermediate  
847 level to reduce the chamber gain. Restoring the nominal gain is inhibited until the LHC operators  
848 declare stable beams via a data interchange protocol.

### 849 **6.3 High voltage**

850 The HV system comprises 36 HV modules in 5 crates. The 1044 HV channels, 1 of each polarity provid-  
851 ing anode and drift voltage to each chamber, are controlled via a 250 kbit/s CAN bus through a dedicated  
852 Linux-based DIM server [82]. The published DIM services, commands and remote procedure calls  
853 (RPC) resemble the logical structure of items used in commercial process control servers: the command  
854 to change a setting is confirmed by the server via a read back setting. In addition, the actual measured  
855 value from the device is published. Update rates for different services can be adjusted independently.

856 The HV gain and drift velocity are equilibrated for each chamber individually to compensate for small  
857 differences in the chamber geometry. Changes of environmental conditions (atmospheric pressure and  
858 temperature) as well as small variations of the gas composition cause changes in gas gain and drift  
859 velocity. To ensure stable conditions for the level-1 trigger (see Section 12), these dynamic variations are  
860 compensated by automatic adjustments of the anode and drift voltages which are performed in between  
861 runs. These and other automatic actions on the HV are described in Section 7.2.

### 862 **6.4 Detector operation**

863 The DCS employs a dedicated Graphical User Interface (GUI) and a Finite State Machine (FSM). The  
864 FSM allows experts and operators intuitive monitoring and operation of the detector. The FSM hierarchy  
865 reflects the structure of subsystems and devices shown in Fig. 18. Detector conditions are mapped to  
866 FSM states, and these are propagated from the device level upwards to the FSM top node. Standard  
867 operational procedures (configuration of read-out and trigger electronics, ramping voltages etc.) are  
868 carried out via FSM commands which propagate down to the devices and cause a transition to a different  
869 state.

870 The GUI for detailed monitoring and expert operation comprises a dedicated panel for each node in the  
871 FSM tree. An example is shown in Fig. 19. Detector subsystem ‘ownership’, i.e. the right to execute  
872 FSM commands and change the detector state, is only granted to a single operator at a time, and is  
873 represented by symbolic ‘locks’. Operators can work on-site or access the DCS system remotely through  
874 appropriate gateways.

875 The monitoring data acquired by the DCS system are stored in dedicated databases. Dedicated trending  
876 GUIs allow the experts to visualise the time dependence of the detector conditions. During data taking,  
877 the monitoring data needed for detector calibration is queried and made available for offline analysis (see  
878 Section 7.3).

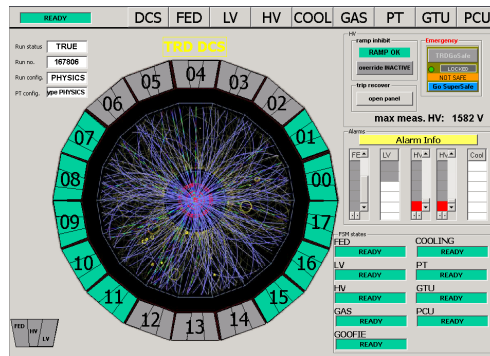


**Fig. 19:** Graphical User Interface: example panel (FSM top node) representing the status in the year 2010 (i.e. with 10 installed TRD sectors). The FSM state of the main systems of each sector is represented by the corresponding colour; run status and alarm summary are displayed. The panel gives quick access to emergency actions and detailed monitoring panels via single mouse clicks.

## 879 7 Operation

880 In this section, first the commissioning steps for the detector and the required infrastructure and then the  
881 operation and performance for different collision systems are described.

### 882 7.1 Commissioning

883 The service connections in the cavern were prepared and tested in parallel to the construction of the  
884 supermodules. The low-voltage connections were tested with dummy loads and the leak tightness of the  
885 cooling loops was verified. The Ethernet connections were checked using both cable testers and stand-  
886 alone DCS boards. The optical fibres for the read-out were controlled for connectivity and mapping.  
887 These tests were crucial in order to identify connection problems prior to the detector installation when  
888 all connections were still well accessible.

889 The supermodules were installed in different installation blocks as described in Section 2. Prior to the  
890 installation the supermodules were tested at the surface site. They were rotated along the  $z_{lab}$ -axis to the  
891 orientation corresponding to their foreseen installation position (e.g. relevant for cooling). A test setup  
892 provided all relevant services (low/high voltage, cooling, Ethernet, read-out, ...) to allow a full system  
893 test of each supermodule. The testing procedure included basic functionality tests, such as water and gas  
894 tightness, front-end electronic stress tests, read-out tests as well as checks of the noise level [66].

895 After successful surface testing, the supermodules were installed into the space frame in the cavern (see  
896 Section 2.3). Subsequently, the services were connected and the basic tests described above repeated to  
897 verify operation in the final setup. At this stage, also the full read-out of the detector with the experiment-  
898 wide trigger and data acquisition systems was commissioned. To check the data integrity of the read-out  
899 chain, test pattern data, generated either in the FEE or in the GTU, were used. Errors observed during  
900 those tests, e.g. bitflips on individual connections on a read-out board, were cured by switching to spare  
901 lines or by masking channels from the read-out if a correction was not possible. After establishing the  
902 read-out, pedestal runs (without zero suppression) were recorded to determine the baseline and noise of  
903 each channel. If needed, further data were recorded to perform a Fourier analysis in order to identify  
904 and fix noise sources, e.g. caused by missing ground connections. In addition, these runs were used to  
905 identify inactive channels which cannot be read out.

906 After each installation block of new supermodules, a dedicated calibration run was performed before the  
907 actual data taking. The detector is read out with radioactive  $^{83m}\text{Kr}$  distributed through the gas system  
908 (see Section 10.2). Since this was usually the first high-rate data taking after the end-of-year shutdown  
909 (and installation), these runs and the preparations for them were an important step to get ready for the

910 real data taking.

911 Before each physics production run, periods of cosmic-ray data taking were scheduled to study the per-  
912 formance of the detector system, to align individual detector components (see Section 9.1) and to pro-  
913 vide reference spectra for particle identification (see Section 11). Data were obtained with and without  
914 magnetic field. A two-level trigger condition was used to ensure sufficient statistics in the detector ac-  
915 ceptance, even when only the first supermodules were installed in the horizontal plane (see Section 12.3).

## 916 7.2 High voltage operation

917 To avoid HV trips during the critical phases of beam injection (e.g. a possible kicker failure), the anode  
918 voltages are reduced to values with very low gain. After the injection is completed, the anode voltages are  
919 ramped up from  $\sim 1030$  V (gain of about a factor  $\sim 100$  lower than nominal) to an intermediate voltage of  
920  $\sim 1230$  V (gain  $\sim 6.5\%$  of nominal). The ramp speed is 6 V/s. After the declaration of stable beams, the  
921 anode voltages are ramped to the nominal voltages ( $U_{\text{anode}} \simeq 1520$  V) for data taking. The drift voltages  
922 always remain at nominal settings.

923 To equalise the gain and drift velocity of all chambers, the results from the calibration (see Section 10)  
924 are used. The nominal voltages and r.m.s. variations for drift and anode voltages are  $2150 \pm 22$  V and  
925  $1520 \pm 14$  V, respectively.

926 Based on measurements in pp, p–Pb and Pb–Pb collisions in RUN 1, it has been estimated that the  
927 chambers had a time averaged current of about 200 nA. This led to a total accumulated charge of less  
928 than 0.2 mC per cm of wire for RUN 1. As the chambers were validated for charges above 10 mC/cm, it  
929 is expected that no ageing effect occurs during the time the TRD is going to be operated. Up to now, in  
930 fact no deterioration in the performance of tracking, track matching and energy resolution was observed.

931 The average anode current as a function of the interaction rate as measured by the T0 detectors used  
932 for the ALICE luminosity measurement has a linear dependence with a slope of 1/200 nA/Hz for p–Pb  
933 collisions at  $\sqrt{s_{\text{NN}}} = 5.02$  TeV. The slope parameter was obtained from different LHC fills ranging from  
934 minimum-bias data taking up to high rate interaction running, where the LHC background conditions can  
935 be different. Under the vacuum conditions in RUN 1, about 1/3 of the current was due to the background  
936 rate, which is nearly negligible in RUN 2.

937 The expected dependence of the measured current on detector occupancy was found. The probability for  
938 pile-up events in, e.g. p–Pb collisions at  $\sqrt{s_{\text{NN}}} = 5.02$  TeV at 200 kHz interaction rate is about 14% when  
939 averaged over time, with a maximum of  $\sim 24\%$  as calculated from the bunch spacing and the number of  
940 bunch crossings in the LHC filling scheme [2, 83] as well as the integration time of the read-out chamber  
941 (drift length/drift velocity).

942 For the level-1 trigger it is crucial to reduce the time dependence of the drift velocity and the gain to  
943 a minimum. The former impacts the track matching, the latter the electron identification. To ensure  
944 the required stability, the anode and drift voltages are adjusted to compensate for pressure changes (the  
945 temperature is sufficiently stable). The parameters for the correction were obtained by correlating the  
946 calibration constants with pressure (see Section 10). A relative pressure change  $dp/p$  results in a change  
947 of gain of  $dG/G = -6.76 \pm 0.04$  and drift velocity of  $dv_d/v_d = -1.41 \pm 0.01$  [84]. In addition, the  
948 dependences of the gain and drift velocity on the anode and drift voltage, respectively, as obtained from  
949 test beam measurements [85] were used (from RUN 2 onwards the dependence of gain on voltage was  
950 taken from the krypton calibration runs). This results in voltage changes of about 0.83 V and 1.4 V  
951 for a pressure change of 1 mbar. During RUN 1 the gain and the drift velocity could be kept constant  
952 within about 2.5% and 1%, respectively. These values include the precision of the determination of the  
953 calibration constants (see Section 10). The variations can be further reduced by measuring and correcting  
954 for the gas composition using a gas chromatograph installed during LS 1.

955 During RUN 1, 10% of the anode and 5.5% of the drift channels turned out to be problematic (see Fig. 35).  
 956 The respective channels had to either be reduced in anode voltage or switched off. As the detector is seg-  
 957 mented into 5 stacks along the beam direction and 6 layers in radial direction, the loss of a single chamber  
 958 in a stack is tolerable and excellent performance is still achieved for tracking and particle identification  
 959 (see Sections 8 and 11). Most of the problematic chambers showed strange current behaviours (trending  
 960 vs time). The de-installation of a supermodule and disassembly of the individual read-out chambers fol-  
 961 lowed by detailed tests revealed that the inspected problematic anode and drift channels had broken filter  
 962 capacitors (4.7 nF/3 kV). Thus, the 4.7 nF capacitors (see Section 4.3) were removed from the resistor  
 963 chain in the last supermodules built and installed during the LS 1 (5 supermodules).

### 964 7.3 In-beam performance

965 After commissioning with cosmic-ray tracks and krypton calibration runs in 2009, the detector went  
 966 into operation and worked reliably during the first collisions at the LHC on December 6<sup>th</sup> 2009. Since  
 967 then, the detector has participated in data taking for all collision systems and energies provided by the  
 968 LHC [2]:

- 969 – pp collisions from  $\sqrt{s} = 0.9$  to 13 TeV at low interaction rates (minimum-bias data taking) and  
 970 high intensities (minimum-bias data taking and rare triggering) with a maximum interaction rate  
 971 of 200–500 kHz. During the rare trigger periods, the detector contributed level-1 triggers on high-  
 972  $p_T$  electrons and jets (see Section 12).
- 973 – p–Pb collisions at  $\sqrt{s_{NN}} = 5.02$  TeV and 8 TeV with interaction rates at the level of 10 kHz  
 974 (minimum-bias data taking) and at maximum 200 kHz (rare triggering). The detector contributed  
 975 the same triggers as in the pp running scenario.
- 976 – Pb–Pb collisions at  $\sqrt{s_{NN}} = 2.76$  TeV and 5.02 TeV with maximum interaction rates of up to 8 kHz  
 977 (minimum-bias and rare triggering).

978 At the beginning of a fill, once all detectors within ALICE are ready for data taking, a global physics  
 979 run is started. A run is defined in ALICE as an uninterrupted period of data taking, during which the  
 980 conditions (trigger setup, participating detectors, etc.) do not change. A run can last from a few minutes  
 981 to several hours until either the experimental setup or conditions have to be changed or the beam is  
 982 dumped. An additional end-of-run (EOR) reason is given by the occurrence of a problem related to  
 983 a given detector or system. The detector parameters measured during a run, such as the voltages and  
 984 currents of the anode and drift channels as well as temperatures of the FEE, are dumped at the EOR to  
 985 the Offline Conditions Database (OCDB) via the Shuttle framework [86, 87]. The relevant parameters  
 986 can then be used in the offline reconstruction and analysis.

987 In order to ensure sufficiently stable conditions during a run, any change, such as the failure of a part  
 988 of the detector, e.g. due to a LV/HV trip, triggers the ending of the run. In order to avoid too frequent  
 989 interruptions, the failure of a single chamber within a stack is ignored. Technically, this is realised using  
 990 the so-called Majority Unit within DCS.

991 All subcomponents of the TRD detector (infrastructure and gas system) are monitored via DCS (see  
 992 Section 6). In case any entity deviates from nominal running conditions by pre-defined thresholds a  
 993 warning is issued. The single entity is either recovered by the DCS operator in the ALICE Run Control  
 994 Centre or by an expert intervention. During RUN 1 data taking, most interventions were related to the  
 995 recovery of single event upsets (SEU) and HV trips of problematic channels by re-configuration of the  
 996 FEE or ramping up of the anode/drift channels. For RUN 2 an automatic recovery of the FEE and HV  
 997 was put in place.



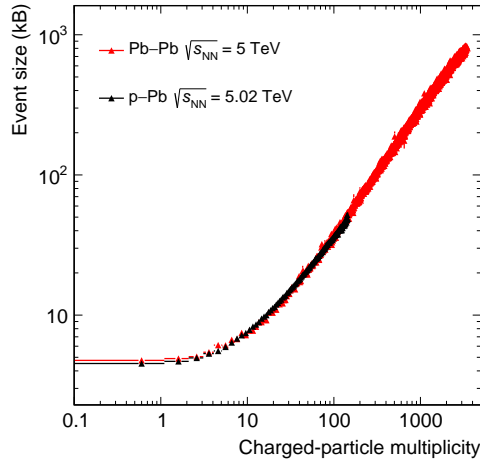


**Fig. 20:** Event size vs charged-particle multiplicity for various collision systems for one supermodule. To obtain the charged-particle multiplicity, global tracks (see Section 8) fulfilling minimum tracking quality criteria were counted on an event-by-event basis.

### 998 7.3.1 Read-out performance

999 The event size depends on the charged-particle multiplicity. It is therefore influenced by the collision  
1000 system and the background conditions of the LHC. The event size vs. charged-particle multiplicity is  
1001 shown for various collision systems for one supermodule in Fig. 20. For the most central Pb–Pb collisions  
1002 an event size of 800 kB per supermodule is found.

1003 The dead time per event is composed of the front-end processing and transmission time to the GTU  
1004 and a potential contribution from the shipping to DAQ. On average the former scales approximately  
1005 linearly with the event size and rate, the latter is suppressed by the MEB as long as the read-out data rate  
1006 stays sufficiently below the effective link bandwidth. The typical event sizes of 7 kB, 14 kB, 200 kB in  
1007 minimum-bias data taking for pp, p–Pb, and Pb–Pb collisions result in front-end contributions of 20  $\mu$ s,  
1008 25  $\mu$ s, 50  $\mu$ s, respectively. This does not include the read-out induced part. However, as illustrated by  
1009 the Pb–Pb case shown in Fig. 16, the detector is typically operated in the linear range of the curve,  
1010 indicating that input rate fluctuations are absorbed by the MEB and that the read-out does not contribute  
1011 significantly to the dead time.

1012 The read-out rate during RUN 1 and until now in RUN 2 ranged from about 100 Hz in rare trigger periods  
1013 to about 850 Hz in minimum-bias data taking in pp and p–Pb collisions. In Pb–Pb collisions, the read-out  
1014 rate was about 100 Hz and 350 Hz for minimum-bias data taking in Pb–Pb collisions in RUN 1 and up to  
1015 now in RUN 2, respectively.

### 1016 7.3.2 Radiation effects

1017 The radiation on the TRD was for RUN 1 and RUN 2 (until the end of 2016) rather low both in terms of  
1018 flux and dose. The following radiation calculations for the inner radius of the TRD are based on simula-  
1019 tions obtained using the FLUKA transport code [88] and taking into account the measured multiplicities  
1020 of Pb–Pb, p–Pb and pp collisions [89–94] as well as the running scenarios (luminosities, running time,  
1021 and interaction rate). For the indicated time range the Total Ionisation Dose (TID) and the Non-Ionising  
1022 Energy Loss (NIEL), quoted in 1-MeV-neq fluence, were  $7 \cdot 10^{-3}$  krad and  $2 \cdot 10^9$  cm $^{-2}$ , respectively. The  
1023 flux of hadrons is highest in Pb–Pb collisions, because it is proportional to the product of the interaction  
1024 rate and the particle multiplicity. For Pb–Pb collisions at  $\sqrt{s_{NN}} = 5.02$  TeV, the flux of hadrons with  
1025  $> 20$  keV energy and charged particles is about  $3.8 \cdot 10^{-2}$  kHz/cm $^2$  and  $2.5 \cdot 10^{-2}$  kHz/cm $^2$ , respectively.

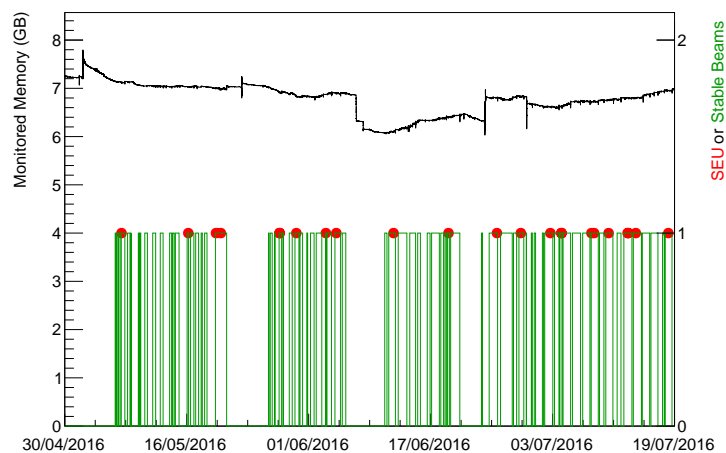


**Fig. 21:** Monitored external DCS memory and occurrences of SEUs as a function of time. The periods of stable beam are indicated as well.

1026 The radiation load in terms of flux and dose are far below the values, for which the experiment was  
 1027 designed for [1].

1028 In the radiation environment described above, very few SEUs are observed in the electronics. The most  
 1029 affected device is the DCS board, for which SEUs result in occasional reboots (a few DCS boards per  
 1030 LHC fill). The DCS board is needed for control and monitoring but is not part of the read-out chain  
 1031 meaning that the reboots do not affect the data taking. The external RAM on the DCS board can be  
 1032 monitored for SEUs by writing and verifying known patterns in unused areas of the  $\sim 13$  MB memory per  
 1033 chamber. During 2.5 months of pp data taking at LHC luminosities of about  $5 \cdot 10^{30} \text{cm}^{-2} \text{s}^{-1}$ , 20 SEUs as  
 1034 shown in Fig. 21 were observed in the external RAM, i.e. a negligible amount compared to the occasional  
 1035 reboots of a few DCS boards.

1036 The memories of the TRAPs are Hamming-protected and, thus, resilient to SEUs. However, the con-  
 1037 figuration registers are not protected and can be affected by radiation. Therefore, the configuration is  
 1038 compressed and written to a Hamming-protected memory area. In this way, the registers can be checked  
 1039 (and corrected) against the compressed configuration.

### 1040 7.3.3 Data quality assurance

1041 The Data Quality Monitoring framework (DQM) provides online feedback on the data and allows prob-  
 1042 lems to be quickly spotted and identified during data taking. The Automatic MONitoRing Environment  
 1043 (AMORE) was developed for ALICE [95] and allows run-based, detector-specific analyses on the raw  
 1044 data. The results are visualised in a dedicated user interface. The monitored observables, such as noise  
 1045 level, event size per supermodule, trigger timing, FEE not sending data, are compared with reference  
 1046 values or diagrams (depending on the data taking scenario). Deviations from the references indicate a  
 1047 problem to the operator. Based on the information obtained from the online DQM all runs are directly  
 1048 marked with a quality flag, both globally and for the individual ALICE subdetectors. For the offline  
 1049 physics analyses, lists of runs are selected based on these flags according to the physics case under study.

### 1050 7.3.4 Pretrigger performance

1051 A dedicated wake-up signal is required for the FEE (see Section 5.1). It should reflect the level-0 trigger  
 1052 condition as closely as possible. However, as it needs to be generated before the actual level-0 trigger,

1053 it cannot use the same information. This introduces some inefficiency into the TRD read-out. In the  
1054 early RUN 1 LHC filling schemes (e.g. during the LHC ramp-up in 2009) with only a few colliding  
1055 bunches per orbit, it was possible to send a wake-up signal for all of the bunch crossings with potential  
1056 interactions. This resulted in a fully efficient operation [71]. During this time, the pretrigger system was  
1057 commissioned to use the V0 and T0 signals as inputs. They could then also be used for filling schemes  
1058 with many bunches. The trigger condition was configured as closely as possible to the ALICE level-0  
1059 interaction trigger, i.e. a coincidence of either the V0 or the T0 detectors (simultaneous signals in the A-  
1060 and C-side, see Section 2). The efficiency of the V0- and T0-derived wake-up signals depends on the  
1061 discrimination thresholds used for those detectors and on the inherent dead time between pretrigger and  
1062 the abort or end of the read-out (see Section 5). The latter is particularly important when subsequent  
1063 collisions are close in time, e.g. in LHC filling schemes that have bunch trains with 25 or 50 ns bunch  
1064 spacing [96]. For runs taken at low interaction rates the pretrigger efficiency is above 97%; for higher  
1065 rates the efficiency depends on the colliding bunch structure of the filling scheme and reaches average  
1066 values down to about 83% in RUN 1 [71]. These inefficiencies were avoided with the LM system used  
1067 in RUN 2 (see Section 5.1).

1068 The analysis of electrons from heavy-flavour hadron decays in p-Pb collisions at  $\sqrt{s_{NN}} = 5.02$  TeV in  
1069 events satisfying the pretrigger condition showed no bias compared to results from events triggered with  
1070 the ALICE level-0 minimum-bias interaction trigger [97].

## 1071 8 Tracking

1072 The charged particle tracking in the ALICE central barrel is based on a Kalman filtering [98]. Track  
1073 finding and fitting are performed simultaneously [2]. The algorithm operates on clusters of track hits  
1074 from the individual detectors. The clusters carry position information and, depending on the detector,  
1075 the amount of charge from the ionisation signal. The cluster parameters are calculated locally from the  
1076 raw data, implying that the cluster finding can be parallelised.

1077 The global tracking starts from seed clusters at the outer radius of the TPC (see Fig. 1). During the  
1078 first inward propagation of the tracks previously unassigned TPC clusters are attached while updating  
1079 the track parameterisation at the same time. If possible, the track is further propagated to the ITS.  
1080 Subsequently, an outward propagation adds information from TRD, TOF, and HMPID. A second inward  
1081 propagation is used to obtain the final track parameters, which are stored at a few important detector  
1082 positions, most importantly at the primary vertex.

1083 The TRD contributes to the tracking in various ways. First, it adds roughly 70 cm to the lever arm, which  
1084 improves significantly the momentum resolution for high- $p_T$  tracks. Second, it increases the precision  
1085 and efficiency of assigning clusters from the detectors at larger radii, in particular the TOF, to propagated  
1086 tracks. In addition, the TRD is used as reference to obtain correction maps for distortions in the TPC,  
1087 which arise from the build up of space charge at high interaction rates. For this the TRD and ITS  
1088 track segments are reconstructed using as seeds the TPC tracks (with relaxed tolerances accounting for  
1089 potential distortions). Then, the estimate of the real track position is built as a weighted average of the  
1090 ITS and TRD refitted tracks (without TPC information). The TPC distortions are deconvoluted from the  
1091 residuals between these interpolations and the measured TPC cluster positions.

1092 The tracking in the TRD can be subdivided into the formation of tracklets (track segments within one  
1093 read-out chamber) from clusters and the updating of the global tracks based on the tracklets. These steps  
1094 are performed layer-by-layer. The chambers within a layer can be treated in parallel. For each layer, a  
1095 seed track is prepared by propagation from the TPC and used to calculate the intersection with a chamber.  
1096 Based on this information a tracklet is formed from the clusters in the vicinity of this intersection and  
1097 then the track parameterisation is updated accordingly. In the following, details of the individual steps  
1098 will be given.

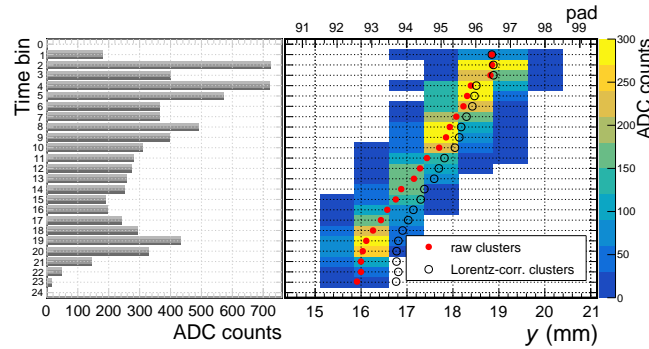


**Fig. 22:** Signal produced by a positively charged particle ( $p_T = 0.5 \text{ GeV}/c$ ). Left: Total charge per time bin used for particle identification. Right: Ionisation signal vs. pad number and time bin. The cluster positions are shown as reconstructed from the charge distribution (raw clusters) and after correction for the  $E \times B$  effect (Lorentz-corr. clusters).

### 1099 8.1 Clusterisation

1100 Primary ionisation in the detector gas leads to a signal that spreads over several pads. Because of the  
 1101 slower ion drift, the charge carries over into subsequent time bins, resulting in a correlation between  
 1102 time bins (see Section 2.1). The cluster algorithm combines the data from adjacent pads in the same  
 1103 time bin, producing clusters with information on position and total charge. The former is calculated  
 1104 from the weighted mean of the charge shared between adjacent pads (up to 3). Look-Up Tables (LUT)  
 1105 are used to relate the measured charge distribution to the actual position. These LUTs are the result of  
 1106 calculations for the different pad width sizes, based on measurements in a test beam [46]. The cluster  
 1107 position can deviate from the LUT values because of detector parameters which are subject to calibration  
 1108 (see Section 10), most importantly the drift velocity  $v_d$  and the time offset  $t_0$  (time corresponding to the  
 1109 position of the anode wires, see Fig. 30). In addition, a correction for the  $E \times B$  effect is applied. The  
 1110 complete position characterisation also includes the estimated uncertainty, which determines the weight  
 1111 for updating the global track. The uncertainties are derived from differential analyses of Monte Carlo  
 1112 simulations. Cluster properties such as the deposited energy, time bin, and reconstructed position relative  
 1113 to the pad with the maximum charge are taken into account as well as particle level characteristics such  
 1114 as electrical charge and incident angle. A linear model relates all uncertainties with parameters being  
 1115 defined by all conditions determining a cluster.

### 1116 8.2 Track reconstruction

1117 For the preparation of the TPC-based track seed used to match with the TRD clusters, the Kalman  
 1118 parameterisation (at the outer radius of the TPC) is propagated to the radial position of the anode wires  
 1119 of a given chamber. At this radius the position is least affected by variations in calibration parameters.  
 1120 If a chamber is rotated with respect to the tracking frame, the radial position of the anode wires depends  
 1121 on the intersection point of the track in the  $y$ - $z$  plane. As this is only known after the propagation, the  
 1122 preparation of the track seed is an iterative process.

1123 The clusters that are assigned to the seed track in a given layer are combined into tracklets. A straight  
 1124 line fit is sufficient for their description since the negligible sagitta of the trajectory is only of the order  
 1125 of tens of microns.

1126 Since in the read-out chamber the electrons drift in the radial direction, that is approximately parallel  
 1127 to the track, and due to the long ion tails, the signals pile up. The measured charges, sampled in time  
 1128 intervals of 100 ns, are therefore correlated between different time samples. Since such correlations  
 1129 degrade the angular resolution, a tail cancellation correction is applied [46]. It subtracts an exponential

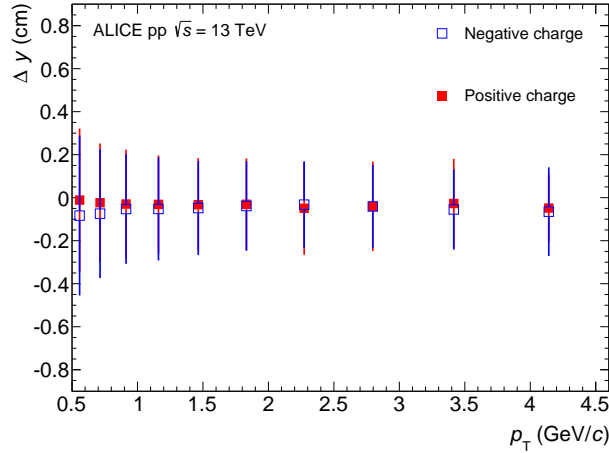


**Fig. 23:** Residuals in  $\Delta y$  of tracklets with respect to global tracks as a function of  $p_T$  in pp collisions at  $\sqrt{s} = 13$  TeV. For every bin the mean (marker) and r.m.s. width (error bar) of the distribution are shown.

1130 tail proportional to the current signal from the subsequent samples for each read-out pad.

1131 The number of pads on the the read-out plane onto which a track is projected depends on the track  
 1132 incident angle. For decreasing transverse momentum, more pads will carry a signal. The Lorentz angle  
 1133 also affects this spread. For negatively (positively) charged particles the Lorentz drift is along (opposite  
 1134 to) the track inclination, independent of the polarity of the magnetic field. On average, negatively charged  
 1135 particles are thus spread over fewer pads than positively charged ones. In the right panel of Fig. 22, an  
 1136 example of a positively charged particle of  $p_T = 0.5$  GeV/c (worst case) is shown. Its projection spans  
 1137 over 6 pads.

1138 The procedure to find candidates for seeds involves a preliminary stage in which clusters are searched in  
 1139 the neighbourhood of the propagated seed. In Fig. 23 the mean and width of the residuals are shown for  
 1140 the arising tracklets in  $\Delta y$  in layer 0 as a function of the seed  $p_T$ . The imperfect tail cancellation results  
 1141 in different position biases for tracklets from positive and negative tracklets, the signal spreading over  
 1142 more pads for the former.

### 1143 8.3 Performance

1144 The relative frequencies of the number of tracklets assigned to a track are shown in Fig. 24 for pp  
 1145 collisions at  $\sqrt{s} = 13$  TeV. Tracks consisting of 6 layers account for more than 50% (60%) for  $p_T <$   
 1146  $1$  GeV/c ( $p_T > 1$  GeV/c). Tracks with 4 and 5 layers are mainly produced by particles crossing dead  
 1147 areas of the detector.

1148 A crucial figure of merit for the tracking is the fraction of global tracks matched to the TRD. This  
 1149 includes acceptance effects, between the TPC and the TRD as well as the TRD and the TOF detector.  
 1150 The momentum dependence is shown in Fig. 25 for tracks with at least 4 layers (about 75% of all tracks).  
 1151 For positively charged particles, the Lorentz drift of the electrons is opposite to the track inclination,  
 1152 which (together with the tail cancellation) results in a slightly higher efficiency.

1153 A systematic analysis of the position resolution in the bending plane ( $r\phi$ ) is presented in Fig. 26. The  
 1154 resolution ( $\sigma_{\Delta y}$ ) is expressed as the width of a Gaussian fit to the difference between the position recon-  
 1155 structed via tracklets and different references ( $\Delta y$ ). It is shown as a function of the inverse transverse  
 1156 momentum scaled with the particle charge ( $q/p_T$ ). First, the ideal position resolution is derived from  
 1157 Monte Carlo simulations by comparing the reconstructed tracklet position with the true particle position

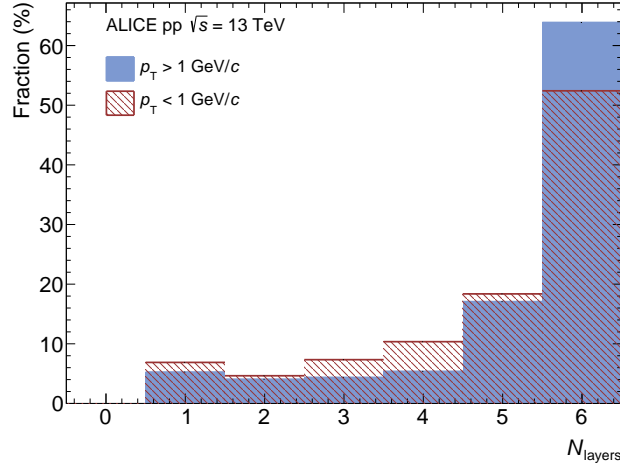


**Fig. 24:** Fraction of tracks, originating from the primary vertex, consisting of a given number of layers in pp collisions at  $\sqrt{s} = 13$  TeV.

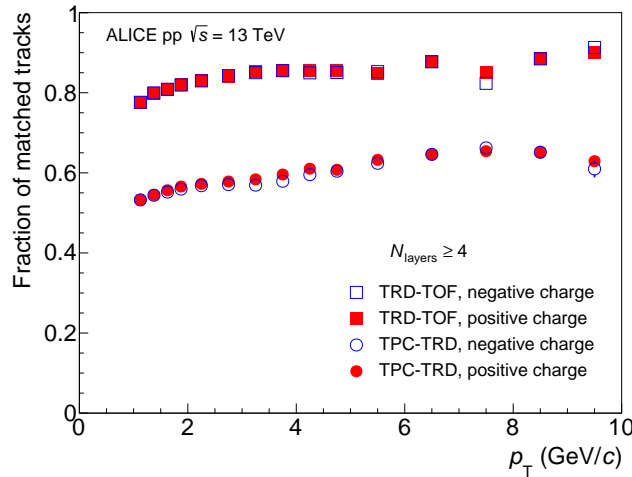


**Fig. 25:** Fraction of tracks matched between the TPC and the TRD (TPC-TRD) and further the TOF detector (TRD-TOF) as a function of transverse momentum in pp collisions at  $\sqrt{s} = 13$  TeV.

1158 at the reference radial point (anode wire plane of the read-out chamber). This is shown as the red curve  
 1159 in Fig. 26, calculated in local chamber coordinates to decouple residual misalignment effects from the  
 1160 result. A parabolic best fit is performed for which the parameters show the best position resolution of  
 1161 close to  $200 \mu\text{m}$  at  $p_T = 1.8 \text{ GeV}/c$ . The best performance is achieved for tracks where the inclination  
 1162 angle cancels the  $E \times B$  effect. In the case of real data, the comparison can be performed only against a  
 1163 measured estimator, i.e. against the reconstructed global (ITS + TPC) track. The black curve shows the  
 1164 distribution for pp collisions at  $\sqrt{s} = 8 \text{ TeV}$ . The combined position resolution of the TRD and global  
 1165 tracks is around  $700 \mu\text{m}$  at very large transverse momentum. In order to bridge the two results, observ-  
 1166 ables at the level of reconstruction and simulation are compared. The blue curve shows the position  
 1167 resolution of the global tracks as reconstructed against the true position from the Monte Carlo simula-  
 1168 tion. The green line represents the theoretical value for the combined resolution for TRD and global  
 1169 tracks, given by the quadratic sum of the dependencies described by the red and the blue distributions.

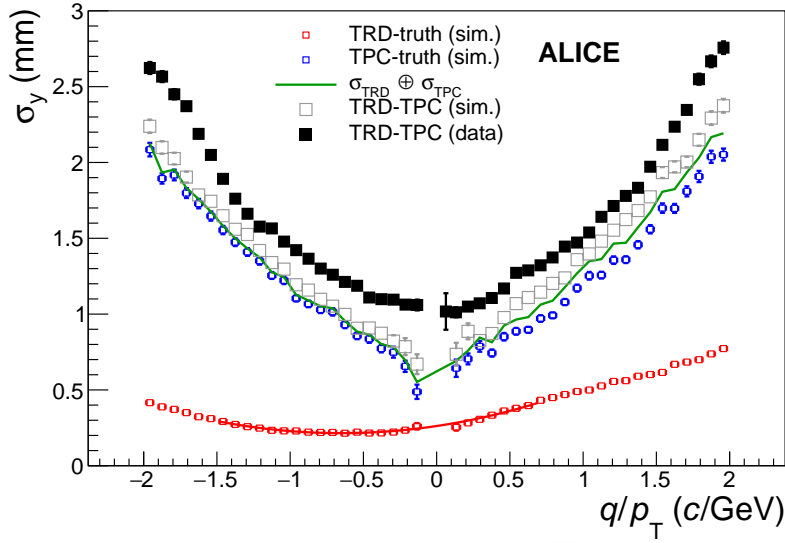


**Fig. 26:** Dependence of the position resolution on charge over transverse momentum for simulated tracks in the TRD (red) and in the TPC (blue), reconstructed global tracks from simulation (gray) and from pp collisions at  $\sqrt{s} = 13$  TeV (black). The label TRD-TPC indicates global tracks reconstructed with the ITS and TPC that were extrapolated to the TRD. The green line represents the theoretical value for the combined resolution of TRD and global tracks. The red line shows a parabolic fit to the corresponding points.

1170 These tracks from simulation yield a slightly worse resolution because the theoretical limit does not  
 1171 consider the pad tilting. It is worth noting that the simulated position resolution describes the measured  
 1172 dependency reasonably well. Effects of remaining miscalibration and misalignment of all central barrel  
 1173 detectors lead to a degradation of about 500  $\mu\text{m}$  for the resolution in the TRD.

1174 The good position resolution capabilities demonstrated by the TRD detector can be used in the central  
 1175 barrel tracking of ALICE to improve the transverse momentum resolution of reconstructed particles.  
 1176 Figure 27 shows the  $q/p_T$  resolution of the combined ITS-TPC tracking with and without the TRD  
 1177 for various running scenarios. In all considered cases the TRD was also used as reference to obtain  
 1178 the correction maps for the distortions in the TPC. The inclusion of the TRD in tracking in addition  
 1179 improves the resolution by about 40% at high transverse momentum for pp collisions recorded at both  
 1180 low (12 kHz) and high interaction (230 kHz) rates. For example in the low interaction scenario of pp  
 1181 collisions, the achieved  $q/p_T$  resolution is 3% at 40 GeV. In addition the inclusion of the TRD in the  
 1182 track reconstruction improves the impact parameter resolution and the reconstruction of tracks that pass  
 1183 at the edges of the TPC sectors, i.e. increasing the acceptance of the experiment.

## 1184 9 Alignment

1185 The physical alignment of the detectors during installation (see Section 2.3) has a finite precision of the  
 1186 order of 1 mm for chambers within a supermodule and of 1 cm for supermodules in the spaceframe. The  
 1187 subsequent software alignment, i.e. accounting for the actual positions of supermodules and chambers  
 1188 in the reconstruction and simulation software, is the subject of this section. The alignment parameters  
 1189 (three shifts and three rotation parameters per alignable volume) are deduced from optical survey data  
 1190 and/or from reconstructed tracks. In the latter case, the obtained values have to be added to those already  
 1191 used during the reconstruction. The obtained alignment sets are stored in the OCDB and used in the  
 1192 subsequent reconstructions.

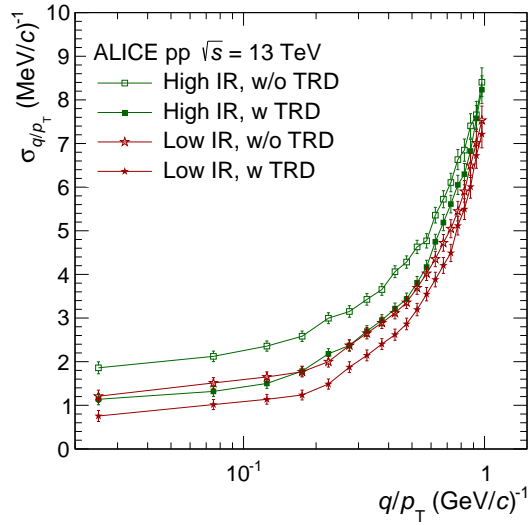


**Fig. 27:** Improvement of the  $q/p_T$  resolution in data when TRD information is included as compared with the performance of tracking without TRD information for various running scenarios. The labels low and high IR indicate interaction rates of 12 and 230 kHz, respectively.

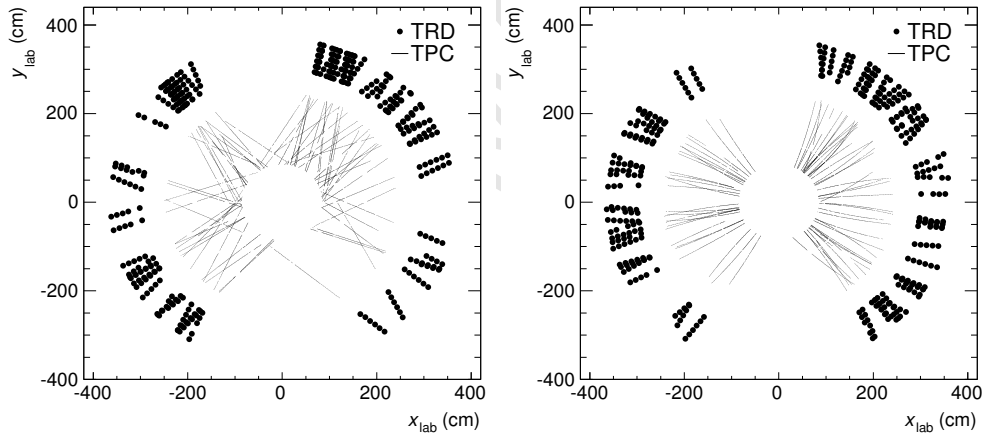


**Fig. 28:** Left: Cosmic-ray tracks with at least 100 TPC clusters and 5 TRD layers, recorded without magnetic field, used for the relative  $r\phi$  alignment of the TRD chambers within stacks (internal alignment). Right: Charged-particle tracks with at least 100 TPC clusters and 4 TRD layers from pp collisions at  $\sqrt{s} = 8$  TeV, used for the alignment of the TRD with respect to the TPC (external alignment). Both figures show data from 2012 (setup with 13 supermodules).

1193 The different alignment steps are described in the following subsections. The alignment is checked and,  
 1194 if necessary, redone after shutdown periods and/or interventions that may affect the detector positions,  
 1195 e.g. installations of new supermodules.

### 1196 9.1 Internal alignment of chambers with cosmic-ray tracks

1197 The internal detector alignment, i.e. the relative alignment of the read-out chambers within one stack, is  
 1198 performed with cosmic-ray tracks recorded without magnetic field (Fig. 28, left). The local  $y$  coordinates  
 1199 (see Section 2) of the chambers of the intermediate layers L1–L4 (tracklet) are varied to minimise the  
 1200  $\chi^2$  of straight tracks calculated from the hits in layers L0 and L5. The coordinates of the first and last  
 1201 chamber, L0 and L5, are kept constant. Any misalignment of a stack, such as a tilt, possibly resulting



Alignment volumes	Input data set	Residual width ( $\sigma$ )
L0	cosmics	2 mm
L2	cosmics	1 mm
L5	cosmics	2 mm
L0	pp collisions	2–3 mm
L2	pp collisions	1–2 mm
L5	pp collisions	2–3 mm

**Table 5:** Typical width of the tracklet-to-track residuals in  $y$  observed during the internal alignment procedure. The residuals are between a tracklet (measured by a single chamber) and track (defined by the remaining chambers of the stack). L0–L5 refer to the six TRD chambers within a stack. The L0 and L5 resolutions are given only for comparison purposes as the positions of these two chambers are fixed during the minimisation.

1202 from this constraint is removed later during the stack alignment. Chamber tilts are neglected. The typical  
 1203 spread (Gaussian  $\sigma$ ) of the residual between tracklet and straight track is about 1 mm for a single chamber  
 1204 (see Table 5). The initial chamber misalignments of 0.6–0.7 mm are reduced to 0.2–0.3 mm (r.m.s.). The  
 1205 minimum required statistics is  $O(10^3)$  tracks per read-out chamber (i.e. per stack). For a few stacks,  
 1206 located around  $\varphi = 0$  and  $\varphi = 180^\circ$ , with low statistics of cosmic-ray tracks, charged tracks from pp  
 1207 collisions taken without magnetic field are used instead.

1208 The internal  $y$  alignment sets deduced from cosmic-ray tracks and from pp collisions agree within  
 1209 0.18 mm (Gaussian  $\sigma$ ). From this, the accuracy of the internal alignment is estimated to be about  
 1210  $\Delta y = 0.18 \text{ mm}/\sqrt{2} = 0.13 \text{ mm}$ . Similar agreement exists between cosmic-ray runs taken in different  
 1211 periods.

## 1212 9.2 Survey-based alignment of supermodules

1213 The supermodules are subject to an optical survey after installation and, subsequently, after every hard-  
 1214 ware intervention that may affect the geometry of the detector. For this measurement, survey targets are  
 1215 inserted into precision holes existing at each end of every supermodule.

1216 Because of poor accessibility of the muon-arm side, the supermodules are only surveyed on one side  
 1217 (A-side). Four of the six alignment parameters,  $x$ ,  $y$ ,  $z$  shifts and the rotation around the  $z$ -axis, are then  
 1218 determined for each supermodule by fitting the survey results. The typical survey precision is 1 mm.  
 1219 The survey-based alignment procedure reduces the supermodule misalignment from its initial value of  
 1220 1–2 cm to a few mm.

## 1221 9.3 External alignment with tracks from beam–beam collisions

1222 The external alignment, i.e. the alignment of TRD volumes with respect to the TPC, is performed with  
 1223 charged-particle tracks recorded with magnetic field (Fig. 28, right). Only tracks with  $p_T > 1.5 \text{ GeV}/c$   
 1224 are used. First, all six alignment parameters of each TRD supermodule are varied to minimise the  
 1225 residuals. Subsequently, the alignment of each stack is refined by adjusting its  $x$  and  $y$  positions and its  
 1226 rotation around the  $z$ -axis. The tracklet-to-track residuals in  $y$  before and after alignment are shown in  
 1227 Fig. 29 for two supermodules. As can be seen, the initial misalignment and the degree of improvement  
 1228 vary supermodule by supermodule. The typical width of the residuals (Gaussian  $\sigma$ ) is about 2 mm (see  
 1229 Table 6). In the limit of low number of tracks per stack  $N_{\text{track}}$ , the alignment precision is statistical:  
 1230  $\sigma/\sqrt{N_{\text{track}}}$ . With  $N_{\text{track}} = O(10^3)$ , systematic effects start to dominate.

1231 Figure 29 shows the effect of an alignment procedure applied to the same data set from which it was  
 1232 deduced. However, one single alignment set is used for runs of a complete year. This raises the question  
 1233 of the universality and temporal stability of the alignment, which can be addressed by comparing align-  
 1234 ment sets deduced from various portions of data. Separate analyses of positive and negative tracks yield

Alignment volumes	Residual width ( $\sigma$ )
L0 chamber	1 mm
L5 chamber	3 mm
stack	2 mm
supermodule	2 mm

**Table 6:** Typical width of the tracklet-to-track residuals observed during the external alignment procedure with  $p_T > 1.5$  GeV/ $c$  tracks from pp collisions. The residuals are between a TRD chamber, stack, or supermodule and the TPC track. L0 and L5 denote the first and the last (radially) TRD chambers within a stack.

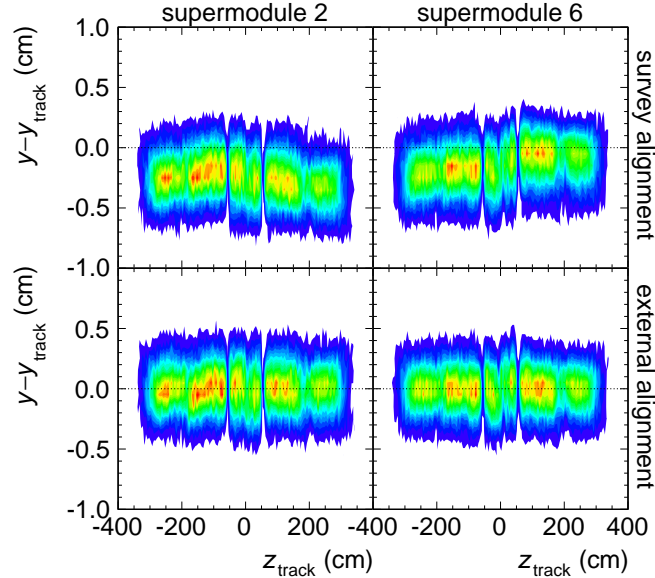


**Fig. 29:** TRD tracklet to TPC track residuals in  $y$  as a function of the  $z$  coordinate of the TPC track ( $z_{\text{track}}$ ) for supermodules 2 (left) and 6 (right). The colour code is linear in the number of tracks. The upper and lower panels show the situation with the survey alignment and with in addition the external alignment, respectively. The data are from a 2012 run of pp collisions with  $B = -0.5$  T. The alignment set used for the lower plots was deduced from the same run. The internal alignment is applied in all four cases.

1235 two alignment sets that agree within 1 mm (r.m.s. of the  $y$  shifts). A larger difference (2 mm) is seen  
 1236 between the two magnetic field polarities. Such differences can result from mechanical displacements  
 1237 and/or from the fact that the TPC calibration is performed separately for the two polarities. The presence  
 1238 of a step in the middle of the central TRD stack, at  $z = 0$ , in Fig. 29 indicates the latter. Several iterations  
 1239 of the TRD to TPC alignment and the TPC calibration with respect to the TRD are needed to achieve  
 1240 the best possible precision. In order to address the entanglement of the alignment and calibration of the  
 1241 central barrel detectors, an alternative approach was developed during LS 1. It is based on a combined  
 1242 alignment and calibration fit performed using the Millepede algorithm [99]. The new method allows for  
 1243 a simultaneous alignment and calibration of the ITS, TRD, and TOF, followed by the calibration of the  
 1244 TPC. The procedure is being used successfully in RUN 2.

## 1245 10 Calibration

1246 The ALICE calibration scheme is explained in [2]. Here the calibration procedures for the TRD are  
 1247 described. The four basic calibration parameters for the TRD – time offset, drift velocity, gain, and noise  
 1248 – are illustrated in Fig. 30. The position of the anode wires and the entrance window are visible in the  
 1249 measured drift time spectrum as a peak (around  $0.5 \mu\text{s}$ , caused by charges coming from both sides of the

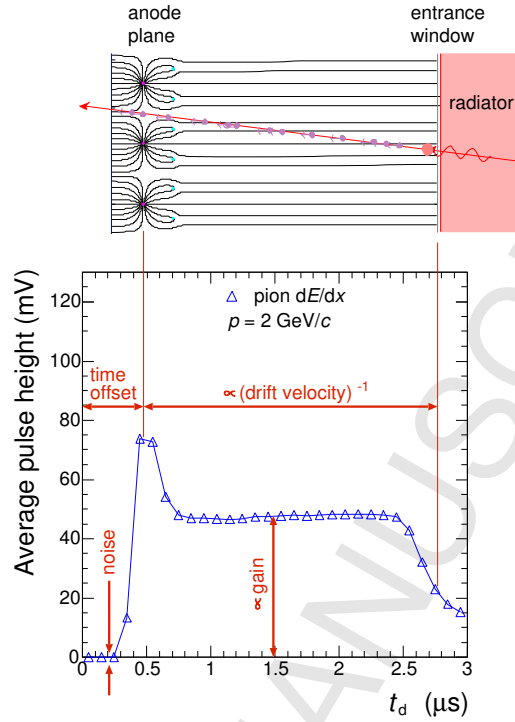


**Fig. 30:** Average pulse height vs. drift time plot (derived from Fig. 5) illustrating the main calibration parameters. For better understanding, a sketch of the chamber cross-section with field lines from Fig. 2 is shown at the top. The peak at the left and the edge on the right of the drift time spectrum correspond to the anode wires and the chamber entrance window. The temporal difference between them depends on the drift velocity. The anode-peak position defines the time offset. The mean pulse height and the pedestal width are related to the gain and the pad noise, respectively.

Input data	Parameters
pedestal runs	pad noise, pad status
runs with $^{83\text{m}}\text{Kr}$ in the gas	relative pad gain
physics runs (cpass0/1)	chamber status, time offset, drift velocity, Lorentz angle, gain

**Table 7:** Sources of input data and the derived calibration parameters.

1250 anode wires) and an edge (around  $2.8 \mu\text{s}$ ), respectively. Since the calibrated time represents the distance from the anode wires, the position of the anode peak provides the time offset. The time span between the  
 1251 anode peak and the entrance-window edge is inversely proportional to the drift velocity. The mean pulse  
 1252 height is proportional to the gain and the width of the pedestal is proportional to the pad noise.  
 1253

1254 While ionisation electrons are attracted to the anode wires by an electric field  $E$ , the presence of a  
 1255 magnetic field perpendicular to it,  $|E \times B| > 0$ , leads to a Lorentz angle of about  $9^\circ$  between the electron  
 1256 drift direction and the direction of the electric field. Knowledge of the Lorentz angle is necessary for the  
 1257 reconstruction of the tracklets, described in Section 8.2 (see Fig. 22 and Fig. 46).

1258 The complete list of the calibration parameters, organised according to the source from which they are  
 1259 determined, is given in Table 7. Once determined for a given run, the calibration parameters are stored in  
 1260 the OCDB and used in the subsequent reconstructions. In the following, the methods used to determine  
 1261 the values of the calibration parameters are discussed.

### 1262 **10.1 Pad noise and pad status calibration using pedestal runs**

1263 Short pedestal runs are taken roughly once per month during data taking. In these runs, events are  
1264 triggered at random instants and the data are recorded without zero suppression. At the end of the run, an  
1265 automatic analysis of the pedestal data is performed on the computers of the DAQ system [100]. Hundred  
1266 events are sufficient to calculate the position of the baseline of the analogue pre-amplifier and shaper  
1267 output (pedestal) and its fluctuation (noise) for all electronics channels. The results are subsequently  
1268 collected by the Shuttle system [87] and transported to the OCDB. The mean noise is 1.2 ADC counts,  
1269 corresponding to an equivalent of 1200 electrons. The pad-by-pad r.m.s. value is 0.17 counts. The  
1270 precision of the measurement is 0.015 counts (r.m.s.). Pads that have a faulty connection to the FEE,  
1271 are connected to a non working FEE channel, have excessive noise, or are bridged with a neighbour are  
1272 marked in the OCDB and treated correspondingly during the data taking and reconstruction chain (pad  
1273 status).

### 1274 **10.2 Pad gain calibration using $^{83\text{m}}\text{Kr}$ decays**

1275 Pad-by-pad gain calibration of the TRD chambers is performed after every installation of new supermod-  
1276 ules. It is done by injecting radioactive gas into the chambers and measuring the signals of the decay  
1277 electrons. The method, developed by ALEPH [101, 102] and DELPHI [103], is also used to calibrate the  
1278 ALICE TPC [31].

1279 Solid  $^{83}\text{Rb}$  decays by electron capture into gaseous Kr and populates, among others, the isomeric state  
1280  $^{83\text{m}}\text{Kr}$  with an excitation energy of 41.6 keV and a half-life of 1.8 hours. The radioactive krypton is  
1281 injected into the gas circulation system and is distributed over the sensitive volumes of all installed  
1282 chambers. The krypton nuclei decay to their ground state by electron emission. The decay energy,  
1283 comparable to the energy lost by a minimum-ionising particle traversing the sensitive volume of a read-  
1284 out chamber (20–30 keV), gets deposited within 1 cm from the decay point. For each decay, the total  
1285 signal is calculated by integrating over  $y$  (pad column),  $z$  (pad row) and  $x$  (drift time), and filled into the  
1286 histogram associated with the pad of maximum signal.

1287 With three gas inlets to each supermodule (see Section 3), groups of 10 chambers are connected in series.  
1288 The difference between the decay rates seen in the first and last chamber of the chain was reduced to a  
1289 factor of  $\sim 3$  by increasing the gas flow during the krypton calibration run. With an  $^{83}\text{Rb}$  source intensity  
1290 of 5 MBq and a measurement time of one week, the collected statistics is of the order of thousand counts  
1291 per pad. This is sufficient to identify the expected decay lines in the distribution. An example is shown  
1292 in Fig. 31. The histogram of each pad is fitted by stretching horizontally the reference distribution. The  
1293 stretching factor is the measure of the pad gain. The energy resolution at 41.6 keV is 10%.

1294 The resulting pad gain factors for one particular chamber are shown in Fig. 32. The short-range variations  
1295 of up to 10% reflect the differences between electronics channels. The long-range inhomogeneities  
1296 originate from chamber geometry and are typically within  $\pm 15\%$  (peak to peak). A detailed description  
1297 of the krypton calibration can be found in [104] and [105].

1298 The improvement of the chamber resolution achieved by the krypton-based pad-by-pad calibration is  
1299 presented in Fig. 33. The histograms show the pulse height spectrum before calibration, after one and  
1300 after two iterations (calibrations performed in consecutive years), respectively.

### 1301 **10.3 Chamber calibration using physics data**

1302 The anode and drift voltages of the individual chambers are adjusted periodically (once a year) to equalise  
1303 the chamber gains and drift velocities. Moreover, an automatic procedure is in place that continuously  
1304 adjusts the voltages depending on the atmospheric pressure, compensating the impact of the environment  
1305 on the gas properties (see Section 7.2). This is important because the pulse height and the tracklet angle  
1306 are used for triggering (see Section 12).

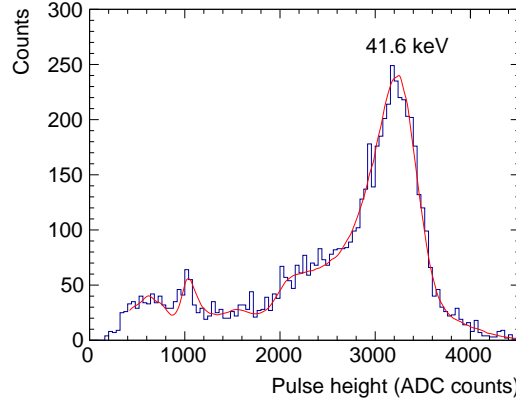


**Fig. 31:** Pulse height spectrum accumulated for one pad during the Kr-calibration run [104, 105]. The smooth solid line represents the fit from which the gain is extracted.

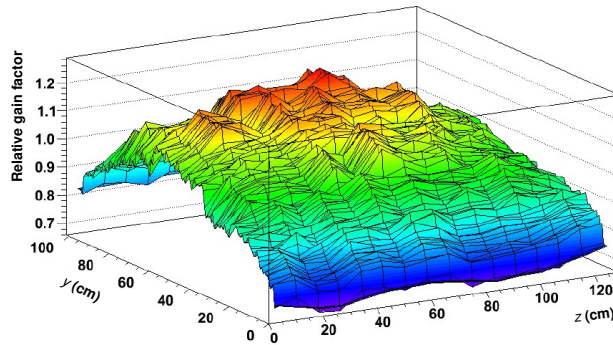


**Fig. 32:** Relative pad gains for one chamber calibrated with electrons from  $^{83\text{m}}\text{Kr}$  decays.

1307 In order to achieve the ultimate resolution for physics data analysis, the chamber status, time offset, drift  
 1308 velocity, Lorentz angle, and gain are calibrated run-by-run offline, using global tracks from physics runs.  
 1309 A sample of events of each run is reconstructed for this purpose. The required statistics is equivalent  
 1310 to  $10^5$  pp interaction events. The first reconstruction pass (cpass0) provides input for the calibration.  
 1311 The second pass (cpass1) applies the calibration and the reconstructed events are used as input for the  
 1312 data quality assurance analysis, and for the second iteration of the calibration. The read-out chamber  
 1313 status and the chamber-wide time offset, drift velocity, Lorentz angle, and gain values are extracted from  
 1314 cpass0 and updated after cpass1. The time offset is obtained as indicated in Fig. 30. The drift velocity  
 1315 and the Lorentz angle are derived from the correlation between the derivative of the local tracking  $y$   
 1316 coordinate with respect to the drift time, and the azimuthal inclination angle of the global track (see  
 1317 Fig. 34). The former represents the uncalibrated estimate of the tracklet angle. The latter is obtained  
 1318 from the extrapolation of the global track to the TRD. The correlation is fitted by a straight line. The  
 1319 effect of the pad tilt ( $dy/dz = \tan(\alpha)$ ,  $\alpha = \pm 2^\circ$ , see Section 2) is taken into account by adding the  
 1320 respective term to the global track inclination. The slope and the offset parameters give the drift velocity  
 1321 and the Lorentz angle, respectively.

1322 The gain calibration factor is determined by histogramming, for each chamber, the deposited charge di-  
 1323 vided by the path length and taking the mean of this distribution. The last stage of the chamber calibration  
 1324 is to identify chambers for which a satisfactory calibration cannot be obtained or whose parameter values  
 1325 are very different from the mean. These chambers are masked in the data analysis and in the respective  
 1326 simulation.

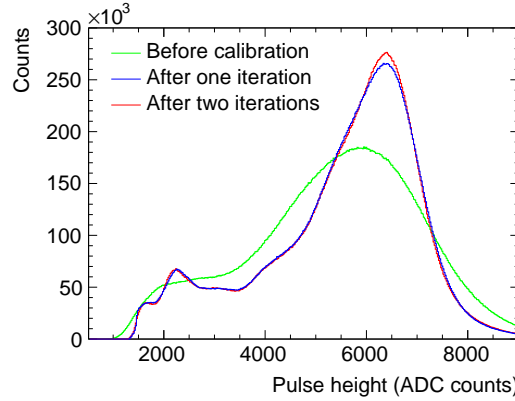


**Fig. 33:** Pulse height spectrum before the krypton-based calibration, after one and after two iterations (calibrations performed in consecutive years) for one read-out chamber.

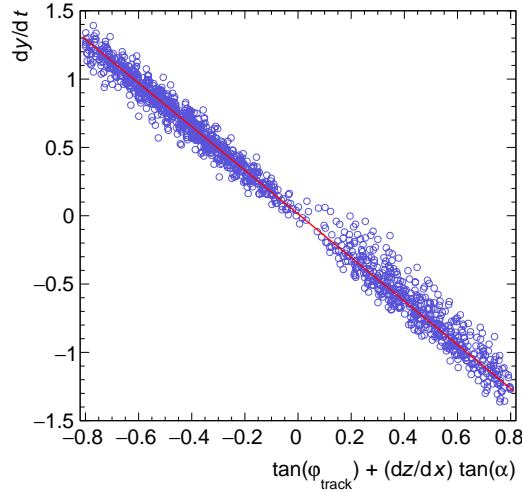


**Fig. 34:** The derivative of the local tracking  $y$  coordinate with respect to the drift time  $t$  vs. the tangent of the azimuthal track inclination angle from global tracking. The slope and the offset of the fit (red line) give the drift velocity and the Lorentz angle, respectively.

1327 The typical mean values, chamber-by-chamber variations, stability, and precision of the calibration pa-  
 1328 rameters are shown in Table 8. The chamber-by-chamber variation is quantified by the r.m.s. of the  
 1329 chamber distribution within one run. The stability is described via the maximum variations observed in  
 1330 one read-out chamber during half a year of running. The precision is defined as  $1/\sqrt{2}$  of the r.m.s. differ-  
 1331 ence between the calibration parameters deduced from two high-statistics data sets taken under identical  
 1332 conditions.

#### 1333 10.4 Quality assurance

1334 As described before, during cpass1 reconstructed events are subject to a quality assurance (QA) analysis  
 1335 in which control histograms monitoring the quality of the calibrated data are filled. The analogous  
 1336 monitoring of raw data, performed online, is described in Section 7.3. As an example, two such QA  
 1337 histograms, representing the efficiency and the mean number of layers in each stack (equivalent to the  
 1338 number of active layers) in one particular run of the pp data taking in 2015, are shown in Fig. 35. The  
 1339 efficiency drops at stack boundaries and the window in correspondence of the detector coverage of the

Parameter	Mean	Variations	Stability	Precision
$t_0$	145.2 ns	2.7 ns	$\pm 3.4$ ns	1 ns
$v_d$	1.56 cm/ $\mu$ s	1–14%	$\pm 3\%$	0.4%
$\Psi_L$	8.8°	0.3°–0.5°	$\pm 0.4^\circ$	0.05°
gain	1.0 (a.u.)	3–16%	$\pm 7\%$	1.4%

**Table 8:** The typical mean values, chamber-by-chamber variations, stability (in the second half of 2012), and precision of the chamber calibration parameters  $t_0$  (drift time offset),  $v_d$  (drift velocity),  $\Psi_L$  (Lorentz angle for  $B = 0.5$  T), and gain. For the chamber-by-chamber variations, which are subject to equalisation by adjusting the voltages, ranges are indicated.

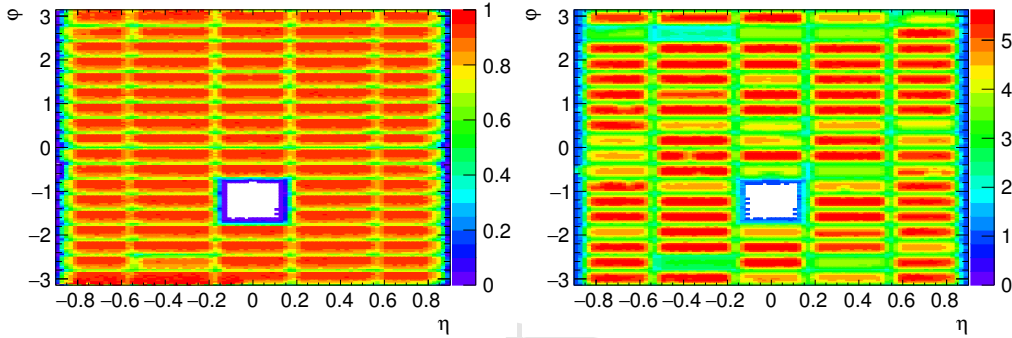


**Fig. 35:** Two quality-assurance plots (data from pp collisions recorded in 2015 with all supermodules installed, tracks with at least 70 TPC clusters and  $p_T > 0.5$  GeV/ $c$ ). Left: Efficiency of matching tracklets to TPC tracks. Right: Mean number of layers per track in each stack (cf. the discussion of inactive chambers in Section 7.2).

1340 PHOS detector are visible.

## 1341 11 Particle identification

1342 The TRD provides electron and charged hadron identification based on the measurement of the specific  
 1343 energy loss and transition radiation. The total integrated charge measured in a tracklet [107], normalised  
 1344 to the tracklet length, is shown in Fig. 36 for electrons and pions in p–Pb collisions at  $\sqrt{s_{NN}} = 5.02$  TeV.  
 1345 The electron and pion samples were obtained by selecting tracks originating from  $\gamma \rightarrow e^+e^-$  conversions  
 1346 in material and from the decay  $K_s^0 \rightarrow \pi^+\pi^-$  via topological cuts and particle identification (PID) with  
 1347 the TPC and the TOF. The obtained electron sample has an impurity of less than 1%. Due to the larger  
 1348 specific energy loss and transition radiation, the average charge deposit of electrons is higher than that  
 1349 of pions. Charge deposit distributions recorded in test beam measurements at CERN PS in 2004 for  
 1350 electrons and pions in the momentum range 1 to 10 GeV/ $c$  [47, 106] describe the results from collision  
 1351 data well (see Fig. 36), and can thus also be used as references for particle identification.

1352 The measured charge deposit distributions can be fitted by a modified Landau-Gaussian convolution:  
 1353 (Exponential  $\times$  Landau)  $\ast$  Gaussian [108, 109], where the Landau distribution is weighted by an expo-  
 1354 nential damping (Landau( $x$ )  $\rightarrow e^{kx}$  Landau( $x$ )). This function describes the specific charge deposit  
 1355 distributions for pions ( $dE/dx$ ) and electrons ( $dE/dx + TR$ ) well and can thus be used to extract the  
 1356 most probable energy loss. The dependence of the most probable signal versus  $\beta\gamma$  is shown in Fig. 37.  
 1357 The data have been extracted from measurements (i) in a beam test at CERN PS in 2004 (pions and  
 1358 electrons) [106], (ii) with pp collisions at  $\sqrt{s} = 7$  TeV (protons, pions and electrons) [107] and (iii)  
 1359 with a cosmic-ray trigger in the ALICE setup (muons) [108]. The selection of the flight direction of  
 1360 the cosmic-ray muons allows only the specific energy loss ( $dE/dx$ ) or the summed signal ( $dE/dx + TR$ )  
 1361 to be measured by selecting muons that first traverse the drift region and then the radiator, and vice  
 1362 versa [108, 109]. To improve the momentum reconstruction of very high  $p_T$  cosmic-ray muons, a ded-

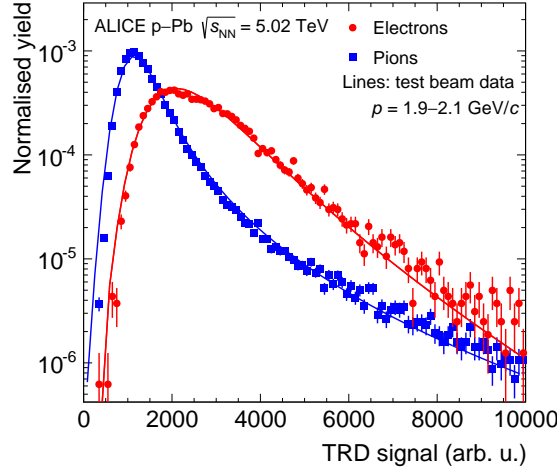


**Fig. 36:** Total integrated charge, normalised to the tracklet length, measured in a single read-out chamber for electrons and pions in p–Pb collisions at  $\sqrt{s_{\text{NN}}} = 5.02$  TeV, in comparison with results from test beam measurements (solid lines) [47, 106]. The electrons and pions from test beam measurements were scaled by one common factor to compensate the difference in gain of the two data sets.

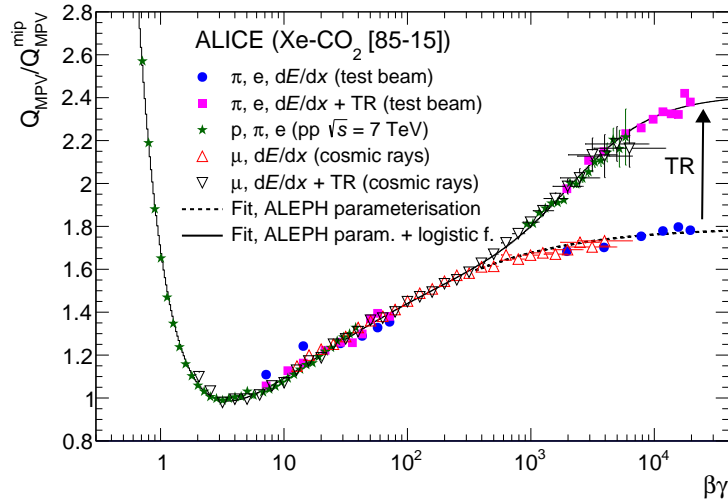


**Fig. 37:** Most probable charge deposit signal normalised to that of minimum ionising particles as a function of  $\beta\gamma$ . The data are from measurements performed in test beam runs, pp collisions at  $\sqrt{s} = 7$  TeV, and cosmic-ray runs. Uncertainties in momentum and thus  $\beta\gamma$  determination are drawn as horizontal and statistical uncertainties as vertical error bars. The shown fits correspond to the Equations 1 and 2 described in the text.

1363 icated track fitting algorithm [108, 109] was developed, combining the clusters of the two individual  
 1364 tracks in the two hemispheres of the TPC. This yields a better momentum resolution by about a factor  
 1365 of 10, e.g. at 1 TeV/c the  $1/p_T$  resolution is  $8.1 \cdot 10^{-4}$  (GeV/c) $^{-1}$  [108, 109].

1366 The onset of the TR production is visible for  $\beta\gamma \gtrsim 800$ , both for electrons and high-energy (TeV scale)  
 1367 cosmic-ray muons. The signals for muons are consistent with those from electrons at the same  $\beta\gamma$ . The  
 1368 most probable signal (MPV) of the energy loss due to ionisation only, normalised to that of minimum  
 1369 ionising particles (mip), is well described by the parameterisation proposed by the ALEPH Collabora-



1370 tion [101, 110] (shown in Fig. 37):

$$\left(\frac{Q_{\text{MPV}}}{Q_{\text{MPV}}^{\text{mip}}}\right) = 0.2 \cdot \frac{4.4 - \beta^{2.26} - \ln\left[0.004 - \frac{1}{(\beta\gamma)^{0.95}}\right]}{\beta^{2.26}}. \quad (1)$$

1371 Minimum ionising particles are at a  $\beta\gamma$  value of 3.5 and the  $dE/dx$  in the relativistic limit is 1.8 times  
1372 the minimum ionisation value. To describe the  $dE/dx + \text{TR}$  signal, a parameterised logistic function is  
1373 needed in addition. The formula, normalised to the signal for minimum ionising particles, is as follows:

$$\frac{\text{TR}}{\text{TR}^{\text{mip}}} = \frac{0.706}{1 + \exp(-1.85 \cdot (\ln \gamma - 7.80))}. \quad (2)$$

1374 The saturated TR yield in the relativistic limit is 0.7 times the minimum ionisation value. At  $\beta\gamma = 2.4 \cdot 10^3$   
1375 the logistic function reaches half its maximum value.

### 1376 11.1 Truncated mean method

1377 The TRD can provide electron (described in the next section) and hadron identification. For the hadron  
1378 identification, the truncated mean is calculated from the energy loss (+TR) signal stored in the clusters  
1379 (see Section 8) [108]. For the particle identification, the deviation from the expected most probable  
1380 signal for a given species is then used after normalisation to the expected resolution of the truncated  
1381 mean signal for the track under study.

1382 In order to obtain an approximately Gaussian shape, the long tail of the Landau distribution needs to be  
1383 eliminated or at least strongly suppressed, which can be realised through a truncated-mean procedure.  
1384 The PID signal of a charged hadron passing through the detector is calculated using all  $M$  clusters along  
1385 the up to six layers (see Section 8). The truncated mean is then calculated as the average over the  $N$  lowest  
1386 values:  $N = f \cdot M$ . The truncation fraction  $f = 0.55$  was chosen in order to maximise the separation power  
1387 between minimum ionising pions with  $p = 0.5$  GeV/ $c$  and electrons with  $p = 0.7$  GeV/ $c$ . The different  
1388 momenta were chosen to maximise the statistics of the electron sample [108]. However, the cluster  
1389 signal strength depends on the radial position of the cluster within the read-out chamber (see Fig. 5).  
1390 Therefore, the cluster amplitudes are first weighted with time-bin dependent calibration factors, found  
1391 and applied during the `cpass0/cpass1` calibration steps (see Section 10). For example, for the cosmic-ray  
1392 data sample, the weights are determined for tracks within the interval  $1.65 \leq \log_{10}(\beta\gamma) \leq 2.5$  to eliminate  
1393 kinematic dependences. These  $\beta\gamma$  are far below the onset of TR. After applying this procedure, some  
1394 non-uniformity over time bins remains ( $\pm 15\%$ ), which is due to the TR component [108].

1395 Figure 38 shows the truncated mean signal as a function of momentum for p-Pb collisions at  $\sqrt{s_{\text{NN}}} =$   
1396 5.02 TeV. The curves represent the expected signals for various particle species. These parameterisa-  
1397 tions were obtained by fitting the truncated mean signal ( $dE/dx + \text{TR}$ ) of electrons from conversion  
1398 processes, pions from  $K_s^0$  and protons from  $\Lambda$  decays as a function of  $\beta\gamma = \frac{p}{m}$  with a sum of the ALEPH  
1399 parameterisation (Eq. 1) and logistic function (Eq. 2), see above.

1400 The resolution of the truncated mean signal is shown in Fig. 39 as a function of the number of clusters  
1401 ( $N_{\text{cls}}$ ), which is described by the function

$$\sigma^{\text{trunc}} = \sqrt{\sigma_{\text{sys}}^2 + \frac{\sigma_{\text{stat}}^2}{N_{\text{cls}}}}, \quad (3)$$

1402 where  $\sigma_{\text{sys}}$  describes systematic uncertainties due to, e.g. residual calibration effects. The fit shows that  
1403 the resolution is, as expected, mainly driven by a statistical scaling according to the law  $\sigma^{\text{trunc}} \propto 1/\sqrt{N_{\text{cls}}}$ .  
1404 The results demonstrate a resolution of the truncated mean signal of 12% for tracks with signals in all

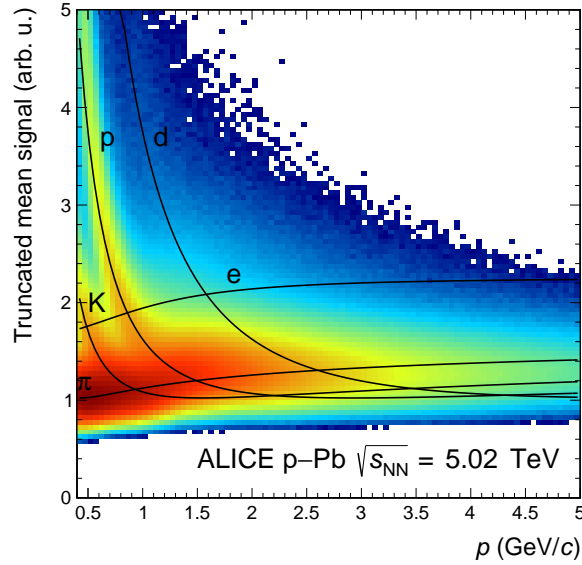


**Fig. 38:** Truncated mean signal as a function of momentum for p–Pb collisions at  $\sqrt{s_{NN}} = 5.02$  TeV. The solid lines represent the expected signals for various particle species.

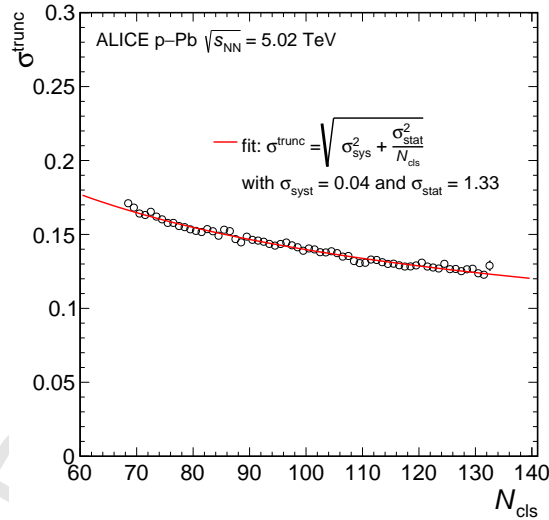


**Fig. 39:** Resolution of the truncated mean signal as a function of the number of clusters in p–Pb collisions at  $\sqrt{s_{NN}} = 5.02$  TeV.

1405 six layers. It should be noted that the resolution is, in parts, limited by the ion tails in the late time bins  
1406 leading to a correlation between individual time bins (see Section 8).

1407 Figure 40 shows the pion-kaon and kaon-proton separation power as a function of momentum. The sep-  
1408 aration power is calculated as the distance between the expected truncated mean signal  $S_{\pi,K}^{\text{trunc}}$  of pions  
1409 (kaons) and kaons (protons) divided by the resolution of the response:  $\frac{\Delta}{\sigma_{\text{trunc}}} = \frac{S_{\pi,K}^{\text{trunc}} - S_{K,p}^{\text{trunc}}}{\sigma_{\text{trunc}}}$ . At low mo-  
1410 menta an excellent separation power is achieved, at high momentum the separation power is about 2 for  
1411  $\pi/K$  and 1 for  $K/p$ .

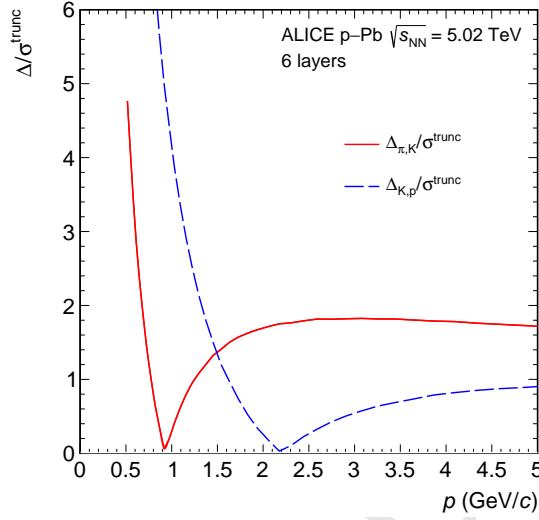


**Fig. 40:** Measured separation power ( $\frac{\Delta}{\sigma^{\text{trunc}}} = \frac{\sigma^{\text{trunc}}_{\pi,K} - \sigma^{\text{trunc}}_{K,p}}{\sigma^{\text{trunc}}}$ ) for  $\pi/K$  and  $K/p$  separation as a function of momentum.

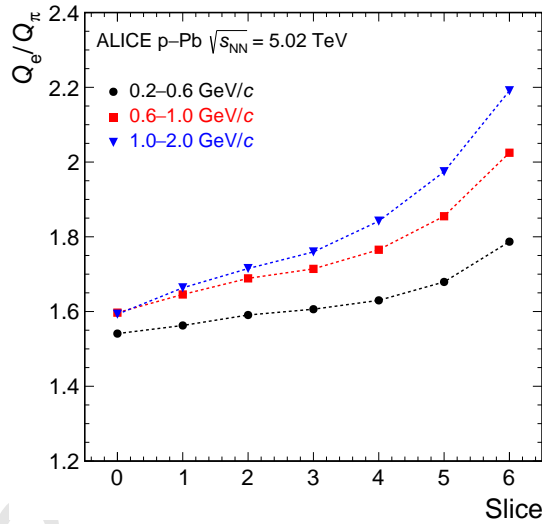


**Fig. 41:** Ratio of the average signal of electrons to that of pions as a function of the depth in the detector (slice number; the lowest (highest) slice number is farthest away from (closest to) the radiator).

## 1412 11.2 Electron identification

1413 For the electron identification (eID), also the temporal evolution of the signal is used. For each TRD  
 1414 chamber the signal amplitudes of the clusters along a tracklet are redistributed into seven slices during  
 1415 the track reconstruction (see Section 8). Each slice corresponds to about 5 mm of detector thickness for  
 1416 a track with normal incidence. The ratio of the average signal for electrons and pions as a function of  
 1417 the slice number is shown in Fig. 41 for p-Pb collisions at  $\sqrt{s_{\text{NN}}} = 5.02$  TeV. At large slice numbers, i.e.  
 1418 long drift times, the TR contribution is visible because the TR photon is predominantly absorbed at the  
 1419 entrance of the drift region.

1420 The eID performance is expressed in terms of the electron efficiency (the probability to correctly identify  
 1421 an electron) and the corresponding pion efficiency (the fraction of pions that are incorrectly identified  
 1422 as electrons). The inverse of the pion efficiency is the pion rejection factor. The following methods

1423 are in use: i) truncated mean (see previous section), ii) a likelihood method with ‘dimensionality’ (one-  
1424 dimensional, LQ1D, corresponds to the total integrated charge [107], two-dimensional, LQ2D, for two  
1425 charge bins [111], etc.), iii) neural networks (NN) [112–114].

1426 For the LQ2D method the signal is evaluated in two charge bins, i.e. the integrated signals of the first  
1427 four slices and the last three slices are averaged. The latter sum contains most of the TR contribution.  
1428 For the LQ3D method, the signals of the slices are combined as sums of the first three, the next two and  
1429 the final two. Both the LQ7D and NN methods utilise 7 charge bins and thus benefit from the complete  
1430 information contained in all 7 slices. While individual slices may be empty, the charge bins must contain  
1431 a charge deposition. In physics analyses, this selection criterion does not introduce a loss of electrons  
1432 when applying the LQ1D or the LQ2D methods, but causes a reduction in the number of electrons  
1433 by about 40% when the LQ7D method is used. The clean samples of electrons and pions described  
1434 above are used to obtain references in momentum bins for particle identification. For each particle  
1435 traversing the TRD, the likelihood values for electrons and pions, muons, kaons and protons are then  
1436 calculated for each chamber via interpolation between adjacent momentum references. The global track  
1437 particle identification is finally determined as the product of the single layer likelihood values. In physics  
1438 analyses, hadrons (e.g. pions) can be rejected with the TRD by applying either a cut on the likelihood  
1439 or a pre-calculated momentum-dependent cut on the likelihood value for electrons. The latter provides  
1440 a specified electron efficiency constant versus momentum. To cross-check the references and determine  
1441 systematic uncertainties, electrons from photon conversions can be studied. In Pb–Pb collisions the  
1442 mean of the charge deposit distributions shows a centrality (event multiplicity) dependence, of about  
1443 15% comparing central and peripheral collisions [111], and therefore centrality-dependent references  
1444 were introduced.

1445 The references can only be created after the relative gain calibration of the individual pads and the time-  
1446 dependent gain calibration of the chambers as described in Section 10. After this, the detector response is  
1447 uniform across the acceptance and in time, and thus it can be studied in detail by combining all chambers  
1448 and the full statistics of 1–2 months of data taking. Since the reference creation requires a large data  
1449 sample, the reference distributions are only produced after the full physics reconstruction pass. This  
1450 means that the reference creation can only be done later, during data analysis rather than already during  
1451 reconstruction. The references for the truncated mean and the likelihood methods are stored for this  
1452 purpose in the Offline Analysis Database (OADB) and read from there in the initialisation phase of the  
1453 analysis tasks [115].

1454 The pion efficiency for 1 GeV/ $c$  tracks is shown as a function of the electron efficiency and as a function  
1455 of the number of detector layers providing signals for the various methods in Fig. 42. For all methods the  
1456 pion rejection factor decreases as expected with decreasing number of contributing layers and a lower  
1457 electron selection efficiency corresponds to a better pion rejection factor for all methods.

1458 A pion rejection factor of about 70 is obtained at a momentum of 1 GeV/ $c$  in p–Pb collisions with the  
1459 LQ1D method, the most simple identification algorithm. The LQ2D method yields a pion rejection factor  
1460 far better than the design goal of 100 at 90% electron efficiency found in test beams with prototypes [106].  
1461 When using the temporal evolution of the signal even better performance is achieved, reaching a rejection  
1462 of up to 410.

1463 Figure 43 shows the momentum dependence of the pion efficiency for the different methods. At low  
1464 momenta, the pion rejection with the LQ1D method improves with increasing momentum because of the  
1465 onset of the transition radiation. From 1–2 GeV/ $c$  upwards, the electron–pion separation power gradually  
1466 decreases due to the saturation of the TR production and the relativistic rise of the specific energy loss  
1467 of pions. The other methods that make use of the temporal evolution of the signal provide substantial  
1468 improvements, in particular for low and intermediate momenta. At high momenta (beyond 2 GeV/ $c$ ),  
1469 the limitation in statistics for the reference distributions is reflected in the rather modest improvements

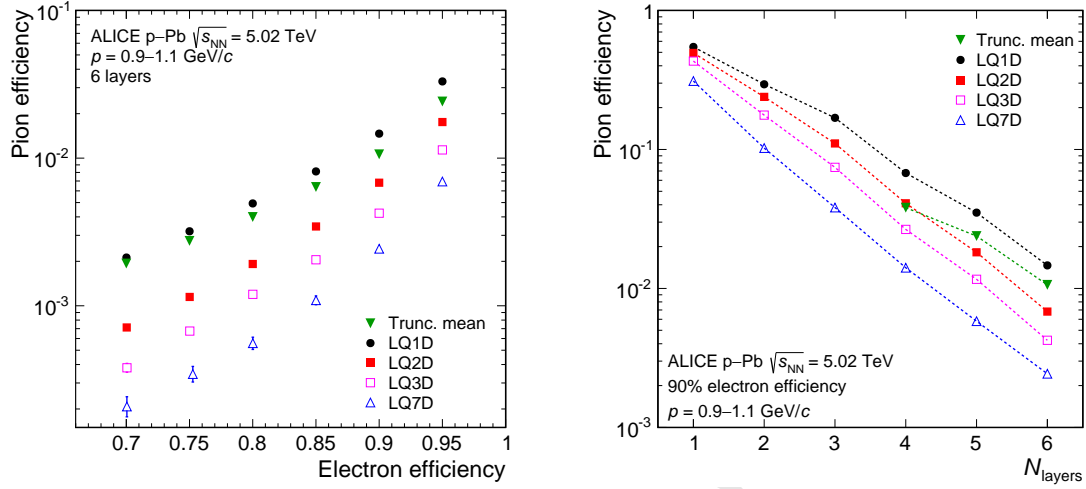


**Fig. 42:** Pion efficiency as a function of electron efficiency (left, for 6 detector layers) and as a function of the number of detector layers (right, for 90% electron efficiency) for the various eID methods. The results are compared for the momentum interval 0.9–1.1 GeV/c in p–Pb collisions at  $\sqrt{s_{\text{NN}}} = 5.02$  TeV. The results of the truncated mean method are only shown for a minimum of 4 tracklets, where the resolution is better than 18% (see Fig. 39).

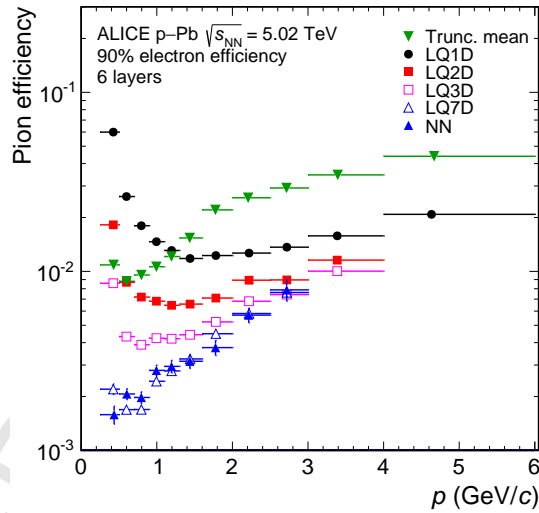


**Fig. 43:** Pion efficiency (for 90% electron efficiency) as a function of momentum for the truncated mean, LQ1D, LQ2D, LQ3D, LQ7D and NN methods. The results are from p–Pb collisions at  $\sqrt{s_{\text{NN}}} = 5.02$  TeV and for tracks with signals in six layers.

1470 in the pion rejection in the multi-dimensional methods. The similar momentum-dependent shape of the  
 1471 likelihood methods is in parts due to the usage of the same data sample for reference creation. The  
 1472 best performance is achieved for the LQ7D and NN methods. However these methods are sensitive to a  
 1473 residual miscalibration of the drift velocity, while the truncated mean and LQ1D method are more robust  
 1474 against small miscalibration effects. At low momentum, where the energy loss dominates the signal, the  
 1475 truncated-mean method provides very good pion rejection. The rejection power of the method decreases  
 1476 at higher momenta, because the TR contribution, yielding higher charge deposits, is likely to be removed  
 1477 in the truncation [108].

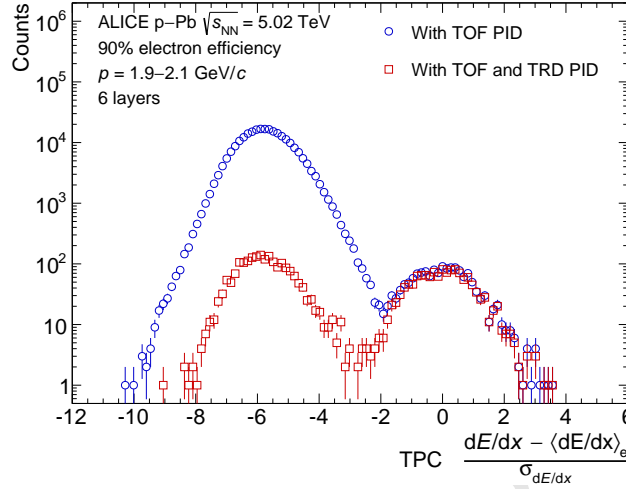


**Fig. 44:** Difference in units of standard deviations between the measured TPC energy loss of a given track and the expected energy loss of an electron with TOF ( $\pm 3\sigma_e^{\text{TOF}}$ ) and TRD (90% electron efficiency) electron identification. The distributions are shown for tracks with a momentum of 1.9–2.1 GeV/c within the TRD acceptance (6 layers in the TRD) in p–Pb collisions at  $\sqrt{s_{\text{NN}}} = 5.02$  TeV.

1478 To visualise the strength of the TRD LQ2D electron identification method, the difference in units of  
 1479 standard deviations between the measured TPC energy loss of a given track and the expected energy  
 1480 loss of an electron for tracks with TOF and TOF+TRD particle identification is shown in Fig. 44. The  
 1481 results are compared for tracks with a momentum of 1.9–2.1 GeV/c within the TRD acceptance. In  
 1482 this momentum interval electrons cannot be discriminated from pions using TOF-only electron identi-  
 1483 fication. After applying the TRD electron identification with 90% electron efficiency with the LQ2D  
 1484 method, hadrons are suppressed by about a factor of 130. The electron identification capabilities of the  
 1485 TRD thus allow selecting a very pure electron sample. This is important, e.g. for the measurement of  
 1486 electrons from heavy-flavour hadron decays. Details on the usage of the electron identification for the  
 1487 latter measurement in pp collisions at  $\sqrt{s} = 7$  TeV can be found in [116].

1488 In the Bayesian approach within ALICE [117], where the identification capabilities of several detectors  
 1489 are combined, the TRD particle identification contributes with its estimate of the probability for a given  
 1490 particle to belong to a given species. For this purpose, transverse momentum dependent ‘propagation  
 1491 factors’ for the priors, which represent the expected abundance of each particle species within the ITS  
 1492 and TPC acceptance, are calculated and stored in the analysis framework.

## 1493 12 Trigger

1494 ALICE features a trigger system with three hardware levels and a HLT farm [2]. Apart from the contri-  
 1495 butions from the pretrigger system (see Section 5.1), the TRD contributes to physics triggers at level-1.  
 1496 These are based on tracks reconstructed online in the GTU (see Section 5.3). The reconstruction is based  
 1497 on online tracklets (track segments corresponding to one read-out chamber) that are calculated locally in  
 1498 the FEE of each chamber. The local tracking in the FEE and the global online tracking in the GTU are  
 1499 discussed in the following.

1500 As the trigger decision is based on individual tracks, a variety of signatures can be implemented, only  
 1501 limited by the complexity of the required calculations and the available time. In the following, the  
 1502 triggers on cosmic-ray muons, electrons, light nuclei, and jets are discussed.

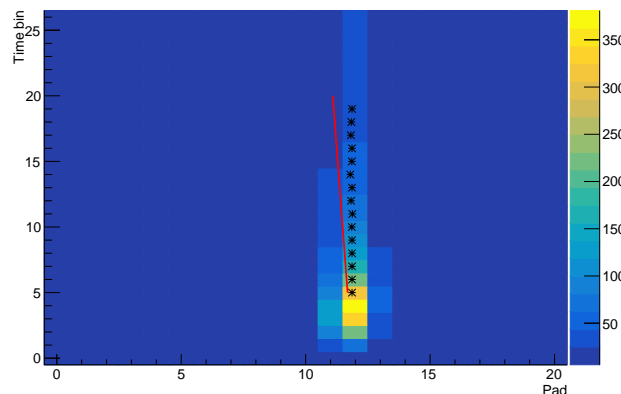


**Fig. 45:** Example tracklet in one MCM. The ADC data for 26 time bins (100 ns each) from 21 channels are shown. The found clusters are marked as asterisks and the final tracklet, calculated as a straight line fit through the clusters, with Lorentz correction as a red line.

### 1503 12.1 Local online tracking

1504 The local online tracking is carried out in parallel in the FEE (see Section 5.2). Each of the 65 000 MCMs  
 1505 processes data from 21 pads, 3 of which are cross-fed from the neighbouring chips to avoid inefficien-  
 1506 cies at the borders of the chip (see Fig. 15). For accurate online tracking, all relevant corrections and  
 1507 calibration steps must be applied online. After appending two digits to avoid rounding imprecisions, the  
 1508 digitised data are propagated through a chain of filters. First, a pedestal filter is used to compensate for  
 1509 variations in the baseline. A gain filter makes it possible to correct for local gain variations, either caused  
 1510 by the chamber or by the electronics. This equilibration is important for the evaluation of the specific  
 1511 energy loss, which is used for online particle identification. It uses correction factors derived from the  
 1512 krypton calibration (see Section 10.2). A tail cancellation filter can be used to reduce the bias from ion  
 1513 tails of signals in preceding time bins. This improves the reconstruction of the radial cluster positions  
 1514 and of the deflection in the transverse plane. The offline reconstruction takes the already applied online  
 1515 corrections into account. For that purpose, all configuration settings are stored in the OCDB and are,  
 1516 therefore, known during the offline processing.

1517 After the filtering, the data for one event are searched time bin-wise for clusters by a hardware pre-  
 1518 processor. A cluster is found if the charge on three adjacent pads exceeds a configurable threshold and  
 1519 the center channel has the largest charge (see Fig. 45). For each MCM and time bin, transverse positions  
 1520 are calculated for up to six clusters. They are used to calculate and store the (channel-wise) sums required  
 1521 for a linear regression.

1522 After the processing of all time bins, up to four channels with a minimum number of found clusters are  
 1523 further processed (if more than four channels exceed the threshold, the four of them with the largest  
 1524 number of clusters are used). For the selected channels, a straight line fit is computed from the pre-  
 1525 calculated sums. The fit results in information on the local transverse position  $y$ , the deflection in the  
 1526 bending plane  $d_y$ , the longitudinal position  $z$ , and a PID value. The transverse position and deflection are  
 1527 calculated from the fit, the longitudinal position is derived from the MCM position, and the PID from a  
 1528 look-up table using the accumulated charge as input.

1529 The reconstructed values for  $y$  and  $d_y$  are corrected for systematic shifts caused by the Lorentz drift  
 1530 and the pad tilt. An example of a reconstructed tracklet is shown in Fig. 46. Eventually, the values (in  
 1531 fixed-point representation) are packed into one 32-bit word per tracklet for read-out.

1532 A realistic simulation of the local tracking was implemented in the ALICE software framework and

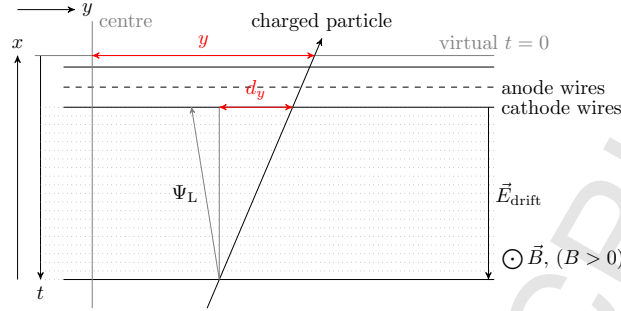


**Fig. 46:** Sketch of the tracklet reconstruction. The tracklet reconstruction in the MCMs is performed in a local coordinate system. The tracklet comprises the information on  $y$ ,  $d_y$ ,  $z$  and PID. The magnetic and electric field and the effect of the Lorentz angle ( $\Psi_L$ ) are indicated as well.

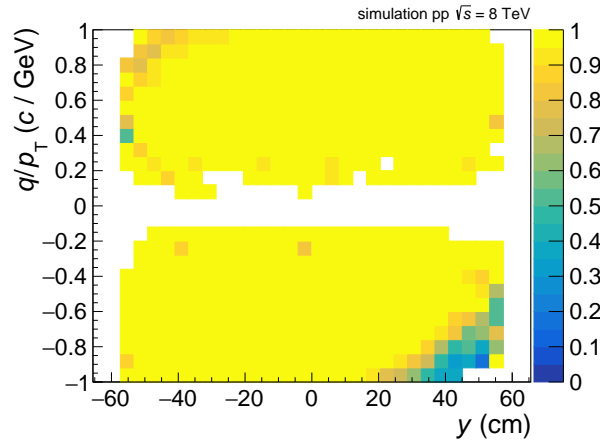


**Fig. 47:** Reconstruction efficiencies for tracklets as a function of  $y$  and  $q/p_T$  for Monte Carlo simulations. The  $z$ -axis entries are zero-suppressed.

1533 is used in Monte Carlo productions based on event generators but can also be run on data recorded  
 1534 with the actual detector. This allows cross-validating hardware and simulation, and to study the effect  
 1535 of parameter changes on the tracklet finding. Therefore, Monte Carlo simulations are well-suited to  
 1536 study the performance of the online tracking algorithm with a given set of configuration options since  
 1537 tracklets can be compared to track references (track positions from Monte Carlo truth information). This  
 1538 allows tracklet efficiencies to be determined. An example is displayed in Fig. 47, which shows the  
 1539 efficiency of the tracklet finding process for a typical set of parameters as a function of  $y$  and  $q/p_T$ . The  
 1540 efficiency drops for large  $y$  and negative  $q/p_T$ , where the asymmetry in  $y$  is caused by a combination  
 1541 of the Lorentz correction and the numerical range available for the deflection. The efficiency is close to  
 1542 100% in the regime relevant for triggering. Furthermore, shifts in  $y$  and  $d_y$  are calculated with respect  
 1543 to the expectation from the Monte Carlo information. Besides a small systematic shift because of the  
 1544 uncorrected misalignment, the distributions show widths of about  $300\ \mu\text{m}$  and  $1700\ \mu\text{m}$  in  $y$  and  $d_y$  [71],  
 1545 respectively.

## 1546 12.2 Global online tracking

1547 The global online tracking in the GTU operates stack-wise on the tracklets reconstructed and transmitted  
 1548 by the FEE. It is divided into a track matching and a reconstruction stage. The algorithm used for the  
 1549 matching of the tracklets is optimised for the high multiplicity environment of Pb–Pb collisions [118]. It



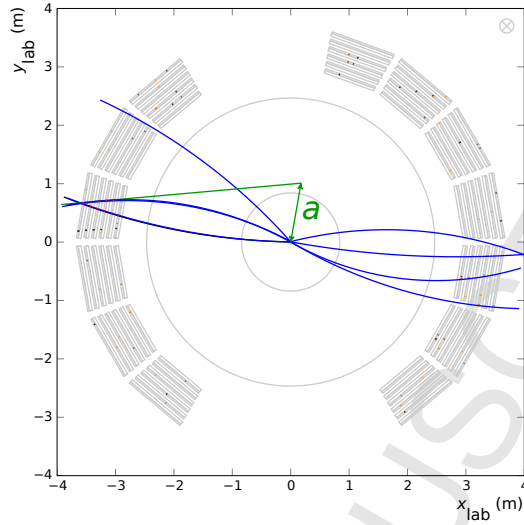


**Fig. 48:** Event display showing the tracks available for the level-1 trigger from the online reconstruction (green) in comparison with helix fits to the contributing tracklets (blue). The offset  $a$  from the primary vertex used as measure for  $1/p_T$  is shown as well. The colour coding of the tracklets (small boxes) is according to stacks.

1550 is implemented in the FPGAs of the GTU (see Section 5.3) and operates in parallel on subsets of tracklets  
 1551 that are compatible with a track in the  $x$ - $z$  plane. Groups of tracklets which fall into ‘roads’ pointing to  
 1552 the nominal primary vertex are pre-selected. The tracklets are propagated to a virtual plane in the middle  
 1553 of the stack. Those which are close enough on this plane are considered to belong to the same track.  
 1554 The algorithm exploits a fixed read-out order of the tracklets to limit the number of comparisons for the  
 1555 matching, meaning that a linear scaling of the tracking time with the number of tracklets can be achieved.

1556 Global online tracks consist of at least four matching tracklets. The reconstruction stage uses the po-  
 1557 sitions of the contributing tracklets to calculate a straight line fit (see Fig. 48). The computation is  
 1558 simplified by the use of pre-calculated and tabulated coefficients, which depend on the layer mask. The  
 1559 approximation of a straight line is adequate for the trigger-relevant tracks above  $2 \text{ GeV}/c$ . The transverse  
 1560 offset  $a$  from the nominal vertex position is then used to estimate the transverse momentum [118]. The  
 1561 PID value for the track is calculated as the average over the contributing tracklets. A precise simulation  
 1562 of all the tracking steps was implemented and validated in AliRoot. It was used for systematic studies of  
 1563 the tracking performance, see below.

1564 Figure 49 shows the timing of the online tracking together with the constraints for the trigger contribu-  
 1565 tions. Between interactions, the FEE is in a sleep mode [78]. In this mode only the ADCs, the digital  
 1566 filters, and the pipeline stages are active. The latter makes it possible to process the data from the full  
 1567 drift time upon arrival of a wake-up signal (see Section 5.1). The processing can be aborted if it is not  
 1568 followed by a level-0 trigger. In this case, a clear sequence is executed for resetting and putting the FEE  
 1569 back to sleep mode. If a level-0 trigger was received, processing continues and the tracklets are sent to  
 1570 the GTU. Here, the track matching and reconstruction runs as the tracklets arrive. The tracks are used  
 1571 to evaluate the trigger conditions (see next sections) until the contribution for the level-1 trigger must be  
 1572 issued to the CTP (about  $6 \mu\text{s}$  after the level-0 trigger). The tracking can continue beyond the contribution  
 1573 time for the trigger; the resulting tracks are ignored for the decision but are available for offline analysis  
 1574 (flagged as out-of-time).

1575 Figure 50 shows the tracking time measured during data taking in p-Pb collisions. It shows the expected  
 1576 linear scaling with the number of tracklets.

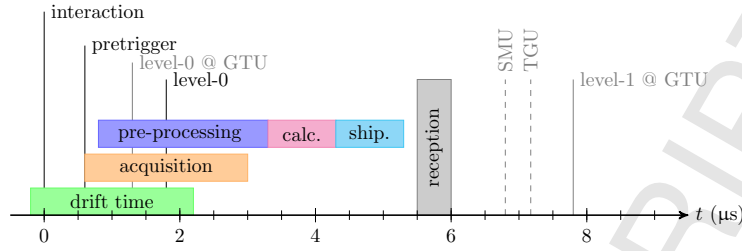


**Fig. 49:** Timing of the various phases for the online tracking with respect to the interaction.

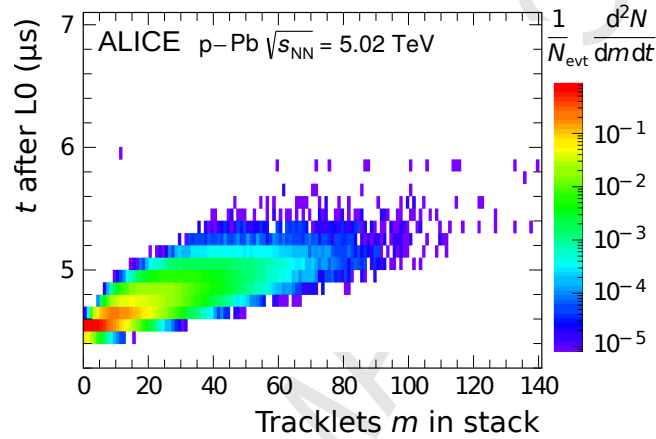


**Fig. 50:** Dependence of the time required for the global online tracking on the tracklet multiplicity in a single stack.

1577 The efficiency of the global online tracking is shown in Fig. 51. In order to separate the efficiency of the  
 1578 online tracking from the acceptance and geometrical limitations, the normalisation is done once for all  
 1579 primary tracks and once for those which are findable, i.e. which have at least 4 tracklets assigned in one  
 1580 stack in the offline tracking (TRD acceptance). The efficiency starts to rise at about 0.6 GeV/c, reaches  
 1581 half of its asymptotic value at 1 GeV/c, and saturates above about 1.5 GeV/c. Lower transverse momenta  
 1582 are not relevant for the trigger operation and corresponding tracks are suppressed at various stages. For  
 1583 comparison, the curve obtained from an ideal Monte Carlo simulation shows slightly higher efficiencies.  
 1584 The difference is caused by non-operational parts of the real detector (see Section 7) not being reflected  
 1585 in the ideal simulation.

1586 The correlation of the inverse transverse momentum from online and offline tracking is established by  
 1587 matching global online tracks to global offline tracks, reconstructed with ITS and TPC, based on a geo-  
 1588 metrical distance measure. An example for pp collisions at  $\sqrt{s} = 8$  TeV is shown in Fig. 52. The online  
 1589 estimate correlates well with the offline value in the transverse momentum range relevant for the trigger  
 1590 thresholds, i.e. 2–3 GeV/c. The width of the correlation corresponds to an online measured resolution of  
 1591 about 10% for momenta of 1.5 – 5 GeV/c.

1592 The  $p_T$  resolution is crucial for the trigger since it determines the sharpness of the threshold. It is shown  
 1593 in Fig. 53 for a  $p_T$  threshold of 3 GeV/c, where a width (10–90%) of about 0.6 GeV/c is found. This is  
 1594 also well reproduced by simulations.

1595 As a further development, the online tracking can benefit from taking the chamber alignment into account  
 1596 in the local tracking, and also by enabling the tail cancellation filter in the FEE. This will allow the use  
 1597 of tighter windows for the track matching and, thus, a reduction in combinatorial background while

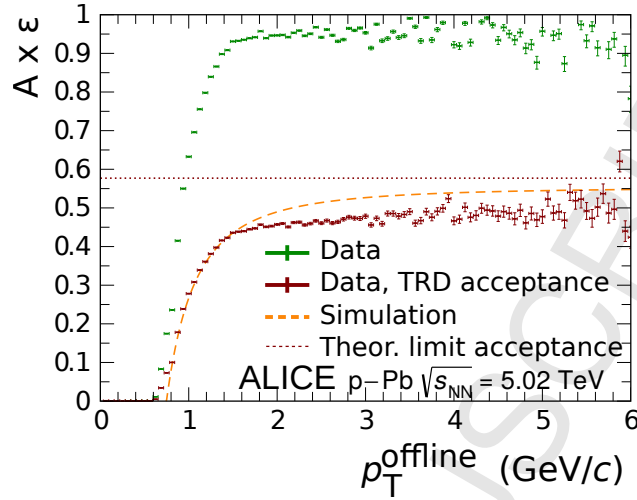


**Fig. 51:** Acceptance times efficiency of the global online tracking for primary tracks (Data) and tracks in the detector acceptance (Data, TRD acceptance) as function of the transverse momentum of the global offline track (trigger threshold at 2–3 GeV/c). The results of an ideal simulation, not considering non-operational parts of the real detector, are drawn for comparison. The dotted line shows the theoretical limit of the acceptance with 13 out of 18 supermodules installed during the p–Pb data taking period in RUN 1.

1598 maintaining the same tracking efficiency. This is relevant for the online tracking in the high-multiplicity  
 1599 environment of Pb–Pb collisions. At the time of writing, these improvements are under development.

### 1600 12.3 Trigger on cosmic-ray muons

1601 Cosmic-ray tracks are used for several purposes in the experiment, e.g. for detector alignment after  
 1602 installation, and before physics runs (see Section 9). Recording sufficient statistics requires a good and  
 1603 clean trigger, in particular for tracks passing the experiment horizontally, for which the rates are very  
 1604 low. Therefore, the first level-1 trigger in ALICE was contributed by the TRD (even before the LHC  
 1605 start-up) in order to select events containing tracks from cosmic rays. It was operated on top of a level-0  
 1606 trigger from TOF (TOF back-to-back coincidence). At first, when the online tracking was still under  
 1607 commissioning, the selection was based on coincident charge depositions in multiple layers of any stack.  
 1608 Later, it used the full tracking infrastructure with the condition requiring the presence of at least one track  
 1609 in the event. This was sufficient to suppress the background from the impure level-0 input from TOF.

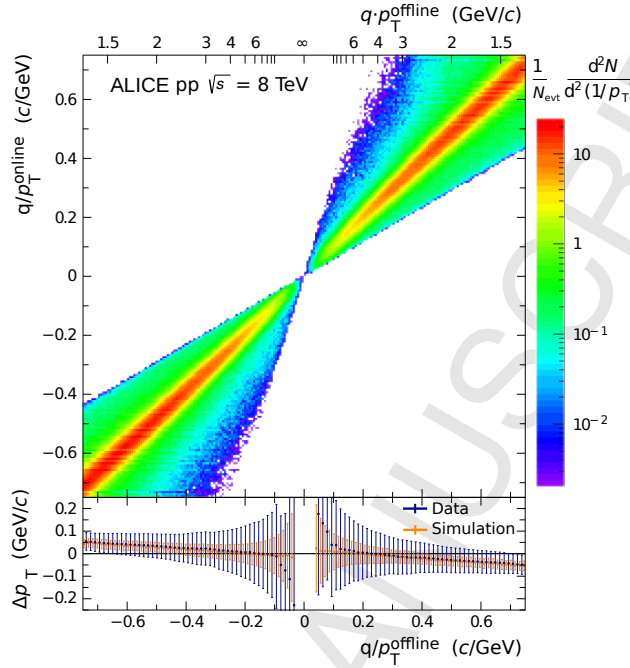


**Fig. 52:** Top: Correlation between  $1/p_T$  obtained from the online tracking and from a matched offline track for pp collisions at  $\sqrt{s} = 8$  TeV. Bottom: Difference (points) of the online and offline track  $p_T$  for data and simulation. The error bars indicate the corresponding width of the difference in  $p_T$ .

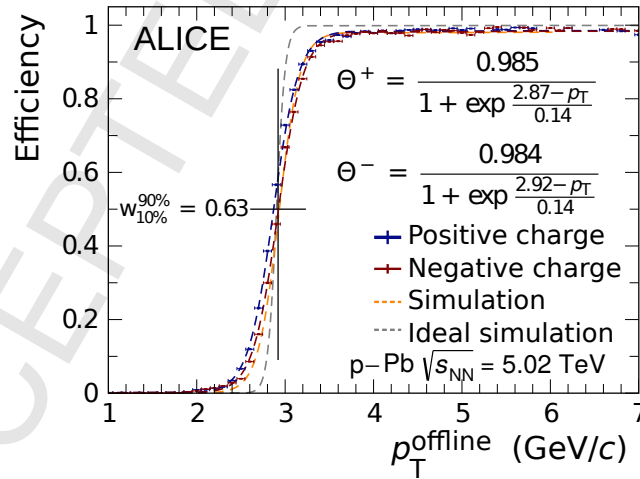


**Fig. 53:** Turn-on curve of the trigger with a  $p_T$  threshold of 3 GeV/c for positively and negatively charged particles in comparison to the same variable computed in simulation with a realistic detector geometry (active channels). Also shown is the corresponding distribution for an ideal detector geometry (ideal simulation, not considering misalignment). The onset is characterised by a fit with a Fermi function.

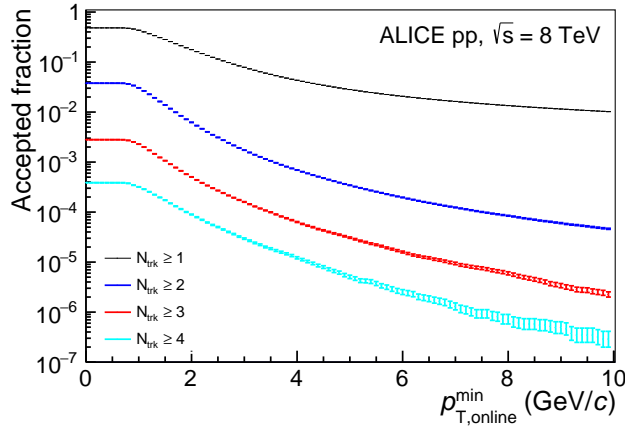


**Fig. 54:** Rejection by the level-1 trigger for requiring 1–4 tracks in any stack ( $N_{\text{trk}}$ ) above varying  $p_T$  thresholds for pp collisions at  $\sqrt{s} = 8$  TeV [71]. The error bars indicate the statistical uncertainties. The distributions were obtained by counting the number of tracks in a stack above a given threshold and normalised by the number of sampled events.

#### 12.4 Trigger on jets

Jets are commonly reconstructed by algorithms which cluster tracks that are close in pseudorapidity and azimuth ( $\eta$ - $\phi$  plane). The area covered by a TRD stack roughly corresponds to that of a jet cone of radius  $R = 0.2$ . This allows the presence of several tracks above a  $p_T$  threshold within one stack to be used as a signature for a high- $p_T$  jet. The TRD is only sensitive to the charged tracks of the jet, which is also the part that is reconstructed using global offline tracking in the central barrel detectors.

In pp collisions at  $\sqrt{s} = 8$  TeV and p–Pb collisions at  $\sqrt{s_{\text{NN}}} = 5.02$  TeV, the trigger sampled the anticipated integrated luminosity of about  $200 \text{ nb}^{-1}$  and  $1.4 \text{ nb}^{-1}$  in RUN 1, respectively. Figure 54 shows the rejection observed in pp collisions ( $\sqrt{s} = 8$  TeV) for the condition of a certain number of global online tracks above a  $p_T$  threshold within any stack. As a compromise between rejection and efficiency for the triggering on jets, 3 tracks above 3 GeV/c were chosen as a trigger condition. This results in a very good rejection, of about  $1.5 \cdot 10^{-4}$ . The jet trigger was also used in p–Pb collisions, where a good performance was achieved as well. However, the higher multiplicity reduces the rejection slightly.

In Fig. 55 the jet  $p_T$  spectra from the TRD-triggered data sample are shown. The jets were reconstructed using the anti-kt jet finder from the Fastjet package [119] with a resolution parameter of  $R = 0.4$ . As expected it extends to significantly larger jet  $p_T$  than the one from the minimum-bias data sample. In order to judge the bias on the shape of the spectrum, it is compared to an EMCal-triggered sample. At sufficiently high  $p_T$  above about 50 GeV/c, the shapes of the spectra agree.

To further judge the bias on the fragmentation, the raw fragmentation function is shown as reconstructed from the jets in the TRD-triggered data sample in Fig. 56. The commonly used variable  $\xi$  is defined as

$$\xi = -\log \frac{p_T^{\text{trk}}}{p_T^{\text{jet}}}. \quad (4)$$

For the lower jet  $p_T$  intervals, a clear distortion can be seen at  $\xi$  values corresponding to the  $p_T$  threshold (in the given jet  $p_T$  interval). It disappears for higher jet  $p_T$ , and agreement with fragmentation functions obtained from an EMCal-triggered sample is found for jet  $p_T$  above about 80 GeV/c [71].

In order to improve the efficiency of the jet trigger, the counting of tracks can be extended over stack boundaries and, thus, avoid the acceptance gaps introduced between sectors and stacks. Corresponding

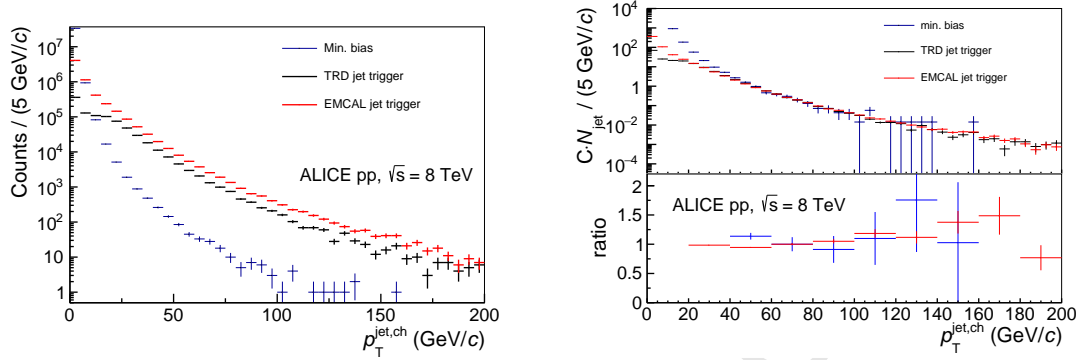


**Fig. 55:** Left:  $p_T$  spectra of leading jets for the minimum-bias and triggered samples of pp collisions at  $\sqrt{s} = 8$  TeV [71]. The leading jets are defined as the jets with the highest  $p_T$  in the event. Right: For comparison the  $p_T$  spectra were scaled to the same yield between 60 and 80 GeV/c. The spectra were re-binned to calculate the ratios.

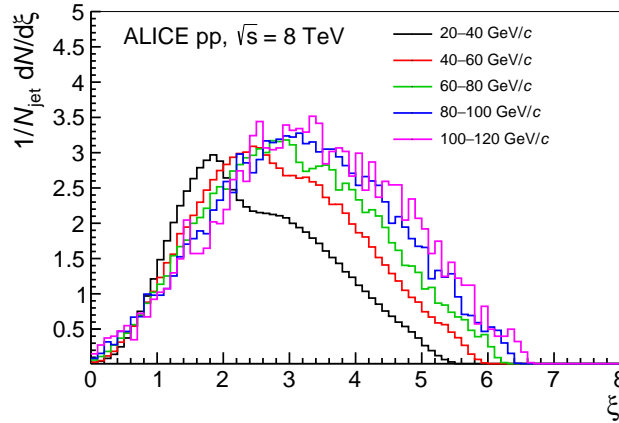


**Fig. 56:** Fragmentation functions of leading jets from the TRD-triggered sample for jets in different  $p_T$  intervals in pp collisions at  $\sqrt{s} = 8$  TeV [71]. The leading jets are defined as the jets with the highest  $p_T$  in the event.

1635 studies are ongoing.

## 1636 12.5 Trigger on electrons

1637 During the tracklet reconstruction stage an electron likelihood is assigned to each tracklet allowing for  
 1638 an electron identification (see Section 12.1). It was calculated using a one-dimensional look-up table  
 1639 based on the total accumulated charge (the hardware also allows a two-dimensional LUT). The tracklet  
 1640 length is taken into account as a correction factor applied to the charge, making the actual look-up table  
 1641 universal across the detector. The look-up table is created from reference charge distributions of clean  
 1642 electron and pion samples obtained through topological identification (see Section 11).

1643 In order to select electrons at the trigger level, a combination of a  $p_T$  threshold and a PID threshold can be  
 1644 used. The thresholds were optimised for different physics cases. For electrons from semileptonic decays  
 1645 of heavy-flavour hadrons, the goal was to extend the  $p_T$  reach at high values. Thus, a  $p_T$  threshold of  
 1646 3 GeV/c was chosen and the PID threshold was adjusted to achieve a rejection of minimum-bias events  
 1647 by a factor of about 100. For the measurement of quarkonia in the electron channel, a  $p_T$  threshold  
 1648 of 2 GeV/c was chosen to cover most of the total cross-section. The PID threshold was increased to

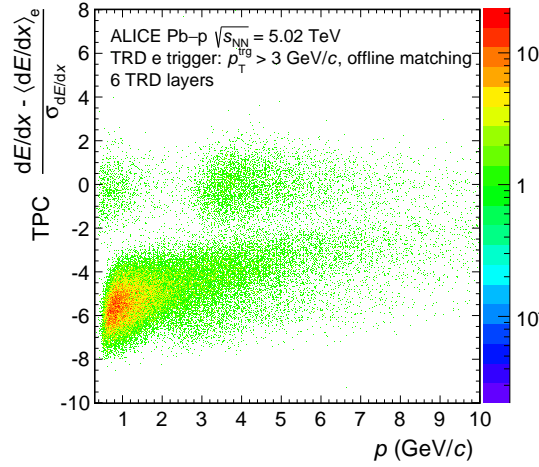


**Fig. 57:**  $n_{\sigma_c}^{TPC}$  as a function of momentum for Pb–p collisions at  $\sqrt{s_{NN}} = 5.02$  TeV recorded with the electron trigger ( $p_T$  threshold at 3 GeV/c). Electrons from photon conversions in the detector material were rejected by matching the online track with a track in the TPC.

1649 achieve a similar rejection as for the heavy-flavour trigger. Both triggers were used in pp and p–Pb (and  
 1650 Pb–p) collisions and share a large fraction of the read-out bandwidth. For example in p–Pb collisions  
 1651 at  $\sqrt{s_{NN}} = 5.02$  TeV recorded during RUN 2, about 45% of the events of both electron triggers with late  
 1652 conversion rejection (see below) overlap.

1653 The main background of the electron triggers is caused by the conversion of photons in the detector  
 1654 material at large radii just in front of or at the beginning of the TRD. The emerging electron-positron  
 1655 pairs look like high- $p_T$  tracks and are likely to also be identified as electrons as well. This background  
 1656 is suppressed by requiring (in addition to the thresholds explained above) at least five tracklets, one of  
 1657 which must be in the first layer. The background can be further reduced by requiring that the online track  
 1658 can be matched to a track in the TPC. However, this can not be done during the online tracking, but only  
 1659 during the offline analysis or in the HLT during data taking.

1660 To judge the performance of the triggers, electron candidates are identified using the signals from TPC,  
 1661 TOF, and TRD. For TPC and TOF the selection is based on  $n_{\sigma_c}$ , i.e. the deviation of the measured signal  
 1662 from the expected signal normalised to the expected resolution. Figure 57 shows the distribution of this  
 1663 variable for the TPC as a function of the track momentum  $p$ . The data sample was derived using an  
 1664 electron trigger with a  $p_T$  threshold of 3 GeV/c and cleaned in the offline analysis by requiring matching  
 1665 with TPC tracks, i.e. rejecting electrons from photon conversions. Above 3 GeV/c the enhancement of  
 1666 electrons is clearly visible in the region around  $n_{\sigma_c}^{TPC} = 0$ .

1667 The enhancement due to the TRD electron trigger in comparison to the minimum-bias trigger is also  
 1668 clearly visible in Fig. 58, which shows a projection of  $n_{\sigma_c}^{TPC}$  in a momentum interval for both data  
 1669 samples. A further suppression of hadrons can be achieved by exploiting the offline PID of the TRD (see  
 1670 Section 11). Figure 59 shows the  $p_T$  spectra of electron candidates with 6 layers identified using the TPC  
 1671 and the TOF in the minimum-bias and triggered data sample. The expected onset at the trigger threshold  
 1672 of 3 GeV/c is observed for the triggered events and shows in comparison to the corresponding spectrum  
 1673 from minimum-bias collisions an enhancement of about 700.

1674 The dominant background for the electron triggers, i.e. the conversion of photons at large radii close to  
 1675 the TRD entrance and in the first part of the TRD, was addressed before RUN 2. The  $p_T$  reconstruction

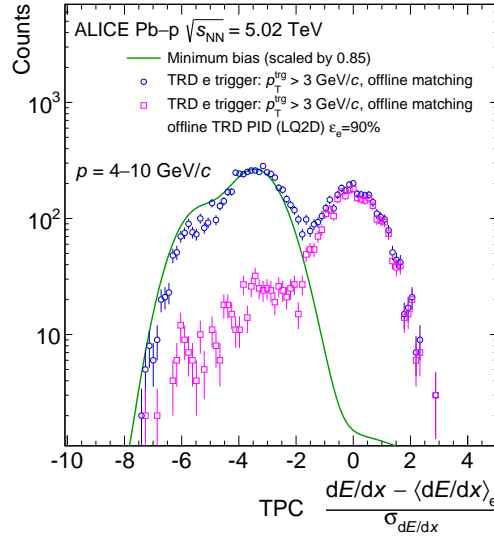


**Fig. 58:** Electron selection for triggered data with and without the TRD offline PID (see Section 11) in Pb-p collisions at  $\sqrt{s_{NN}} = 5.02$  TeV. Electrons from photon conversions in the detector material were rejected by matching the online track with a track in the TPC. The corresponding distribution for minimum-bias data, scaled to the maximum of the distribution of the triggered data sample, is shown to visualise the TRD trigger capability to enhance electrons.

1676 in the online tracking assumes tracks originating from the primary vertex, which results in a too-high  
 1677 momentum for the electrons and positrons from ‘late conversions’ as shown in Fig. 60. An online re-  
 1678 jection based on the calculation of the sagitta in the read-out chambers was implemented and validated.  
 1679 For a sagitta cut of  $\Delta l/p_T = 0.2$  c/GeV an increased rejection of a factor of 7 at the same efficiency  
 1680 was achieved in pp collisions at  $\sqrt{s} = 13$  TeV [120]. For this selection criterion about 90% of the late  
 1681 conversions are removed, while about 70% of the good tracks are kept. This improvement allows only  
 1682 those tracks to be used for the electron trigger which are not tagged as late conversions. This setting was  
 1683 already successfully used in RUN 2.

## 1684 12.6 Trigger on nuclei

1685 A trigger on light nuclei was used for the first time in the high-interaction p-Pb and Pb-p data taking at  
 1686  $\sqrt{s_{NN}} = 5.02$  TeV in 2016. It exploits the much higher charge deposition from multiply-charged particles.  
 1687 The trigger enhances mainly the statistics of doubly-charged particles ( $Z = 2$ ), i.e.  ${}^3\text{He}$  and  ${}^4\text{He}$ . The  
 1688 trigger was operated with an estimated efficiency of about 30% at a rejection factor of about 600.

1689 This trigger is also used in the pp data taking at 13 TeV during RUN 2 to significantly enhance the sample  
 1690 of light nuclei. The trigger does not just enhance the sample of particles with  $Z = 2$ , but also of deuteron,  
 1691 triton and hypertriton (a bound state of a proton, a neutron and a lambda hyperon, which decays weakly  
 1692 into a  ${}^3\text{He}$  and a pion) nuclei. This will allow a precise determination of the mass and the lifetime of the  
 1693 latter.

## 1694 13 Summary

1695 The physics objectives of the TRD together with the challenging LHC environment have led to an ambi-  
 1696 tious detector design. This required the development of a new chamber design with radiator and electron-  
 1697 ics. After extensive tests of individual components and the full system, as well as commissioning with  
 1698 cosmic-ray tracks, the detector was ready for data taking with the first collisions provided by the LHC



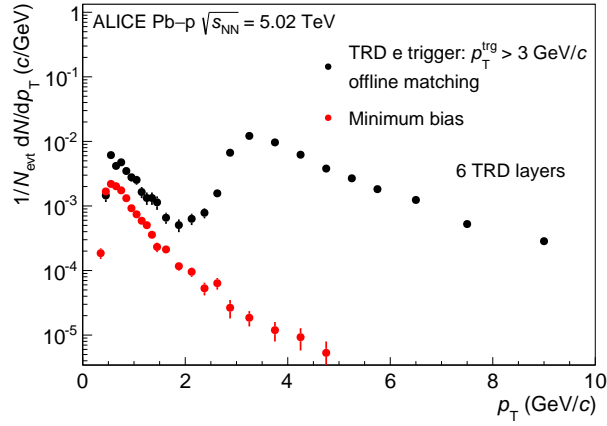


**Fig. 59:**  $p_T$  spectra of identified electrons for the minimum-bias and TRD-triggered data sample of Pb-p collisions at  $\sqrt{s_{NN}} = 5.02$  TeV. For the result of the TRD-triggered sample, electrons from photon conversions in the detector material were rejected by matching the online track with a track in the TPC.

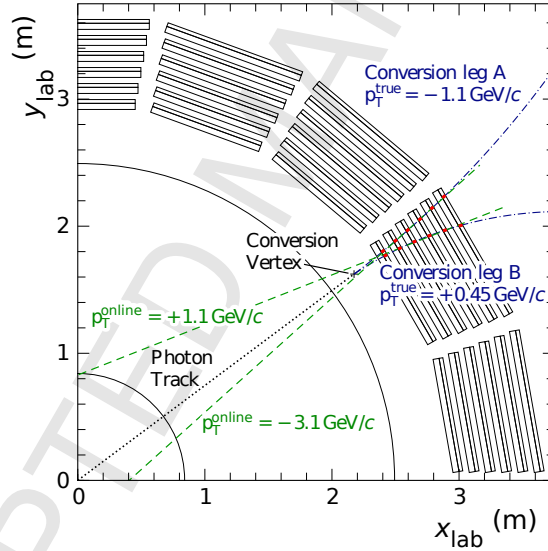


**Fig. 60:** Photon converting into an  $e^+ e^-$  pair at a large radius resembling a high- $p_T$  track for the online tracking (green dashed line) since the offset to the primary vertex is small.

1699 in 2009. During RUN 1, the original setup of 7 installed supermodules was further extended, reaching a  
 1700 maximum coverage of 13/18 in azimuth. The detector was completed in the LS 1 before RUN 2. Since  
 1701 then it provides coverage of the full azimuthal acceptance of the central barrel. Read-out and trigger  
 1702 components were also upgraded. The developed gas system, services and infrastructure, read-out and  
 1703 electronics, and the Detector Control System allow the successful operation of the detector. The xenon-  
 1704 based gas mixture (over  $27 \text{ m}^3$ ) essential for the detection of the TR photons is re-circulated through  
 1705 the detector in order to reduce costs. To minimise the dead time and to cope with the read-out rates for  
 1706 heavy-ion data taking in RUN 2, the data from the detector are processed in a highly parallelised read-out  
 1707 tree using a multi-event buffering technique, with link speeds to the DAQ of about 4 Gbit/s. Failsafe and  
 1708 reliable detector operation and its monitoring was achieved. The resulting running efficiencies are about

1709 100% at read-out rates ranging from 100 Hz to 850 Hz in pp and p–Pb collisions, and up to 350 Hz in  
1710 Pb–Pb collisions.

1711 Robust schemes for calibration, alignment and tracking were established. The TRD adds roughly 70 cm  
1712 to the lever arm of the other tracking detectors in ALICE. The  $q/p_T$  resolution of high transverse mo-  
1713 mentum tracks at 40 GeV/c is thus improved by about 40%. In addition, the TRD increases the precision  
1714 and efficiency of track matching of the detectors that lie behind it. Tracks anchored to the TRD are  
1715 essential to correct the space charge distortions in the ALICE TPC.

1716 Several hadron and electron identification methods were developed. The electron identification perfor-  
1717 mance is overall better than the design value. At 90% electron efficiency, a pion rejection factor of  
1718 about 70 is achieved at a momentum of 1 GeV/c for simple identification algorithms. When using the  
1719 temporal evolution of the signal, a pion rejection factor of up to 410 is obtained.

1720 The complex and efficient design of the trigger allows the provision of triggers based on transverse mo-  
1721 mentum and electron identification in just about 6  $\mu$ s after the level-0 trigger. This procedure successfully  
1722 provides enriched samples of high- $p_T$  electrons, light nuclei, and jets in pp and p–Pb collisions. In pp  
1723 collisions, e.g. at  $\sqrt{s} = 8$  TeV, the jet trigger has efficiently sampled the foreseen integrated luminosity  
1724 of about 200 nb<sup>-1</sup> during RUN 1 with a constant rejection of around  $1.5 \cdot 10^{-4}$ . The TRD will contribute  
1725 further to the physics output of the experiment in various areas, giving enriched samples of electrons,  
1726 light nuclei and jets due to the trigger capabilities as well as its contributions to tracking and particle  
1727 identification.

## 1728 Acknowledgements

1729 The ALICE Collaboration would like to acknowledge the significant contributions to the TRD project  
1730 given by: A. Anjam, W. Amend, V. Aprodu, H. Baumeister, C. Dinca, N. Heine, T. Herold, D. Moisa,  
1731 H. Hinke, H. Hobbel, V. Kiworra\*, L. Prodan, A. Radu, W. Verhoeven, A. Wiesenacker and the CERN  
1732 gas group of EP-DT.

1733 The ALICE Collaboration would like to thank all its engineers and technicians for their invaluable con-  
1734 tributions to the construction of the experiment and the CERN accelerator teams for the outstanding  
1735 performance of the LHC complex. The ALICE Collaboration gratefully acknowledges the resources and  
1736 support provided by all Grid centres and the Worldwide LHC Computing Grid (WLCG) collaboration.  
1737 The ALICE Collaboration acknowledges the following funding agencies for their support in building and  
1738 running the ALICE detector: A. I. Alikhanyan National Science Laboratory (Yerevan Physics Institute)  
1739 Foundation (ANSL), State Committee of Science and World Federation of Scientists (WFS), Arme-  
1740 nia; Austrian Academy of Sciences and Nationalstiftung fur Forschung, Technologie und Entwicklung,  
1741 Austria; Ministry of Communications and High Technologies, National Nuclear Research Center, Azer-  
1742 baijan; Conselho Nacional de Desenvolvimento Cientifico e Tecnologico (CNPq), Universidade Federal  
1743 do Rio Grande do Sul (UFRGS), Financiadora de Estudos e Projetos (Finep) and Fundao de Am-  
1744 paro  Pesquisa do Estado de So Paulo (FAPESP), Brazil; Ministry of Science & Technology of China  
1745 (MSTC), National Natural Science Foundation of China (NSFC) and Ministry of Education of China  
1746 (MOEC), China; Ministry of Science, Education and Sport and Croatian Science Foundation, Croatia;  
1747 Ministry of Education, Youth and Sports of the Czech Republic, Czech Republic; The Danish Council  
1748 for Independent Research | Natural Sciences, the Carlsberg Foundation and Danish National Research  
1749 Foundation (DNRF), Denmark; Helsinki Institute of Physics (HIP), Finland; Commissariat  l’Energie  
1750 Atomique (CEA) and Institut National de Physique Nucleaire et de Physique des Particules (IN2P3) and  
1751 Centre National de la Recherche Scientifique (CNRS), France; Bundesministerium fur Bildung, Wis-  
1752 senschaft, Forschung und Technologie (BMBF) and GSI Helmholtzzentrum fur Schwerionenforschung  
1753 GmbH, Germany; General Secretariat for Research and Technology, Ministry of Education, Research  
1754 and Religions, Greece; National Research, Development and Innovation Office, Hungary; Department

1755 of Atomic Energy Government of India (DAE) and Council of Scientific and Industrial Research (CSIR),  
 1756 New Delhi, India; Indonesian Institute of Science, Indonesia; Centro Fermi - Museo Storico della Fisica  
 1757 e Centro Studi e Ricerche Enrico Fermi and Istituto Nazionale di Fisica Nucleare (INFN), Italy; Institute  
 1758 for Innovative Science and Technology , Nagasaki Institute of Applied Science (IIST), Japan Society for  
 1759 the Promotion of Science (JSPS) KAKENHI and Japanese Ministry of Education, Culture, Sports, Sci-  
 1760 ence and Technology (MEXT), Japan; Consejo Nacional de Ciencia (CONACYT) y Tecnología, through  
 1761 Fondo de Cooperación Internacional en Ciencia y Tecnología (FONCICYT) and Dirección General de  
 1762 Asuntos del Personal Académico (DGAPA), Mexico; Nederlandse Organisatie voor Wetenschappelijk  
 1763 Onderzoek (NWO), Netherlands; The Research Council of Norway, Norway; Commission on Science  
 1764 and Technology for Sustainable Development in the South (COMSATS), Pakistan; Pontificia Universi-  
 1765 dad Católica del Perú, Peru; Ministry of Science and Higher Education and National Science Centre,  
 1766 Poland; Korea Institute of Science and Technology Information and National Research Foundation of  
 1767 Korea (NRF), Republic of Korea; Ministry of Education and Scientific Research, Institute of Atomic  
 1768 Physics and Romanian National Agency for Science, Technology and Innovation, Romania; Joint In-  
 1769 stitute for Nuclear Research (JINR), Ministry of Education and Science of the Russian Federation and  
 1770 National Research Centre Kurchatov Institute, Russia; Ministry of Education, Science, Research and  
 1771 Sport of the Slovak Republic, Slovakia; National Research Foundation of South Africa, South Africa;  
 1772 Centro de Aplicaciones Tecnológicas y Desarrollo Nuclear (CEADEN), Cubaenergía, Cuba, Ministerio  
 1773 de Ciencia e Innovación and Centro de Investigaciones Energéticas, Medioambientales y Tecnológicas  
 1774 (CIEMAT), Spain; Swedish Research Council (VR) and Knut & Alice Wallenberg Foundation (KAW),  
 1775 Sweden; European Organization for Nuclear Research, Switzerland; National Science and Technology  
 1776 Development Agency (NSDTA), Suranaree University of Technology (SUT) and Office of the Higher Ed-  
 1777 ucation Commission under NRU project of Thailand, Thailand; Turkish Atomic Energy Agency (TAEK),  
 1778 Turkey; National Academy of Sciences of Ukraine, Ukraine; Science and Technology Facilities Coun-  
 1779 cil (STFC), United Kingdom; National Science Foundation of the United States of America (NSF) and  
 1780 United States Department of Energy, Office of Nuclear Physics (DOE NP), United States of America.

## 1781 References

- 1782 [1] **ALICE** Collaboration, K. Aamodt *et al.*, “The ALICE experiment at the CERN LHC,” *JINST* **3**  
 1783 (2008) S08002.
- 1784 [2] **ALICE** Collaboration, B. Abelev *et al.*, “Performance of the ALICE Experiment at the CERN  
 1785 LHC,” *Int. J. Mod. Phys. A* **29** (2014) 1430044, arXiv:1402.4476 [nucl-ex].
- 1786 [3] **Wuppertal-Budapest** Collaboration, S. Borsanyi, Z. Fodor, C. Hoelbling, S. D. Katz, S. Krieg,  
 1787 C. Ratti, and K. K. Szabo, “Is there still any  $T_c$  mystery in lattice QCD? Results with physical  
 1788 masses in the continuum limit III,” *JHEP* **09** (2010) 073, arXiv:1005.3508 [hep-lat].
- 1789 [4] **HotQCD** Collaboration, A. Bazavov *et al.*, “Equation of state in (2+1)-flavor QCD,” *Phys. Rev.*  
 1790 **D90** (2014) 094503, arXiv:1407.6387 [hep-lat].
- 1791 [5] P. Braun-Munzinger and J. Stachel, “The quest for the quark-gluon plasma,” *Nature* **448** (2007)  
 1792 302–309.
- 1793 [6] V. L. Ginzburg and I. M. Frank, “Radiation of a uniformly moving electron due to its transition  
 1794 from one medium into another,” *J. Phys. (USSR)* **9** (1945) 353–362. [Zh. Eksp. Teor.  
 1795 Fiz. 16,15(1946)].
- 1796 [7] G. Garibyan, “Contribution to the theory of transition radiation,” *JETP* **6** no. 6, (1958)  
 1797 1079–1085.

- 1798 [8] G. M. Garibian, L. A. Gevorgian, and C. Yang, “X-ray transition radiation produced in an  
1799 irregular medium,” *JETP* **39** no. 2, (1974) 265–270. Russian original - ZhETF, Vol. 66, No. 2, p.  
1800 552, 1974.
- 1801 [9] G. M. Garibian, L. A. Gevorgian, and C. Yang, “The Calculation of x-Ray Transition Radiation  
1802 Generated in Regular and Irregular Layered Media,” *Nucl. Instrum. Meth.* **A125** no. 1, (1975)  
1803 133 – 137.
- 1804 [10] B. Dolgoshein, “Transition radiation detectors,” *Nucl. Instrum. Meth.* **A326** (1993) 434–469.
- 1805 [11] M. L. Cherry, G. Hartmann, D. Muller, and T. A. Prince, “Transition radiation from relativistic  
1806 electrons in periodic radiators,” *Phys. Rev.* **D10** (1974) 3594–3607.
- 1807 [12] **Brookhaven-CERN-Syracuse-Yale** Collaboration, J. Cobb *et al.*, “Transition Radiators for  
1808 electron Identification at the CERN ISR,” *Nucl. Instrum. Meth.* **140** (1977) 413–427.
- 1809 [13] R. D. Appuhn, K. Heinloth, E. Lange, R. Odingen, and A. Schlosser, “Transition Radiation  
1810 Detectors for Electron Identification Beyond 1-GeV/c,” *Nucl. Instrum. Meth.* **A263** (1988) 309.
- 1811 [14] J.F. Detœuf *et al.*, “Status of the transition radiation detector for the D0 experiment,” *Nucl.*  
1812 *Instrum. Meth.* **A279** (1989) 310 – 316.
- 1813 [15] **H1** Collaboration, G. A. Beck *et al.*, “ $e^\pm$  identification using the drift chambers and transition  
1814 radiators of the H1 forward track detector,” *Nucl. Instrum. Meth.* **A367** (1995) 228–232.
- 1815 [16] **D0** Collaboration, H. Piekarz, “Transition radiation detector in the D0 colliding beam experiment  
1816 at Fermilab,” *Nucl. Instrum. Meth.* **A367** (1995) 220.
- 1817 [17] **HERMES** Collaboration, K. Ackerstaff *et al.*, “The HERMES spectrometer,” *Nucl. Instrum.*  
1818 *Meth.* **A417** (1998) 230–265, arXiv:hep-ex/9806008 [hep-ex].
- 1819 [18] P. von Doetinchem *et al.*, “Performance of the AMS-02 Transition Radiation Detector,” *Nucl.*  
1820 *Instrum. Meth.* **A558** (2006) 526–535, arXiv:astro-ph/0608641 [astro-ph].
- 1821 [19] **ATLAS TRT** Collaboration, E. Abat *et al.*, “The ATLAS TRT barrel detector,” *JINST* **3** (2008)  
1822 P02014.
- 1823 [20] M. Ave *et al.*, “The TRACER instrument: A balloon-borne cosmic-ray detector,” *Nucl. Instrum.*  
1824 *Meth.* **A654** (2011) 140–156.
- 1825 [21] V. Beitzel, A. Grunenberg, D. Haun, K. Heinloth, L. Kowalsky, M. Kueckes, H. Muesch,  
1826 T. Siemon, and U. Wollschlaeger, “The Transition radiation detector for ZEUS,” *Nucl. Instrum.*  
1827 *Meth.* **A323** (1992) 135–139.
- 1828 [22] T. Ludlam *et al.*, “Particle Identification by Electron Cluster Detection of Transition Radiation  
1829 Photons,” *Nucl. Instrum. Meth.* **180** (1981) 413.
- 1830 [23] Y. Watase, Y. Suzuki, Y. Kurihara, H. A. Gordon, M. Diwan, R. E. Lanou, and T. Shinkawa, “A  
1831 test of transition radiation detectors for a colliding beam experiment,” *Nucl. Instrum. Meth.* **A248**  
1832 (1986) 379 – 388.
- 1833 [24] M. Holder and H. Suhr, “Separation of Electrons and Pions by a Transition Radiation Detector  
1834 Using Flash ADCs,” *Nucl. Instrum. Meth.* **A263** (1988) 319–324.
- 1835 [25] E. O’Brien *et al.*, “Electron identification in the PHENIX experiment using a tracking TRD,”  
1836 *Nucl. Phys.* **A566** (1994) 615C–618C.

- 1837 [26] Favuzzi C., Giglietto N., Mazziotta M.N., Spinelli P., “Transition radiation detectors for particle  
1838 physics and astrophysics,” *Riv. Nuovo Cim.* **5-6** (2001) 1–172.
- 1839 [27] A. Andronic and J. P. Wessels, “Transition Radiation Detectors,” *Nucl. Instrum. Meth.* **A666**  
1840 (2012) 130–147, arXiv:1111.4188 [physics.ins-det].
- 1841 [28] **Particle Data Group** Collaboration, K.A. Olive and others, “The Review of Particle Physics,”  
1842 *Chin. Phys. C* **38** (2014) 090001.
- 1843 [29] **ALICE** Collaboration, Appelshäuser, H. *et al.*, “Upgrade of the ALICE Time Projection  
1844 Chamber,” Tech. Rep., 2014. CERN-LHCC-2013-020, ALICE-TDR-016.
- 1845 [30] **ALICE** Collaboration, G. Dellacasa *et al.*, “ALICE Technical Design Report of the Inner  
1846 Tracking System (ITS),” Tech. Rep., 1999. CERN-LHCC-99-12.
- 1847 [31] J. Alme *et al.*, “The ALICE TPC, a large 3-dimensional tracking device with fast readout for  
1848 ultra-high multiplicity events,” *Nucl. Instrum. Meth.* **A622** (2010) 316–367, arXiv:1001.1950  
1849 [physics.ins-det].
- 1850 [32] **ALICE** Collaboration, P. Cortese *et al.*, “ALICE: Addendum to the technical design report of the  
1851 Time Of Flight system (TOF),” Tech. Rep., 2002. CERN-LHCC-2002-016.
- 1852 [33] **ALICE** Collaboration, P. Cortese *et al.*, “ALICE electromagnetic calorimeter technical design  
1853 report,” Tech. Rep., 2008. CERN-LHCC-2008-014, CERN-ALICE-TDR-014.
- 1854 [34] **ALICE** Collaboration, G. Dellacasa *et al.*, “ALICE Technical Design Report of the Photon  
1855 Spectrometer (PHOS),” Tech. Rep., 1999. CERN-LHCC-99-04.
- 1856 [35] **ALICE** Collaboration, S. Beole *et al.*, “ALICE Technical Design Report: Detector for High  
1857 Momentum Particle Identification Detector,” Tech. Rep., 1998. CERN-LHCC-98-19.
- 1858 [36] **ALICE** Collaboration, P. Cortese *et al.*, “ALICE Technical Design Report on forward detectors:  
1859 FMD, T0 and V0,” Tech. Rep., 2004. CERN-LHCC-2004-025.
- 1860 [37] **ALICE** Collaboration, E. Abbas *et al.*, “Performance of the ALICE VZERO system,” *JINST* **8**  
1861 (2013) P10016, arXiv:1306.3130 [nucl-ex].
- 1862 [38] **ALICE** Collaboration, G. Dellacasa *et al.*, “ALICE technical design report of the Zero Degree  
1863 Calorimeter (ZDC),” Tech. Rep., 1999. CERN-LHCC-99-05.
- 1864 [39] **ALICE** Collaboration, J. Adam *et al.*, “Determination of the event collision time with the  
1865 ALICE detector at the LHC,” *Eur. Phys. J. Plus* **132** (2017) 99, arXiv:1610.03055  
1866 [physics.ins-det].
- 1867 [40] **ALICE** Collaboration, B. Abelev *et al.*, “Centrality determination of Pb-Pb collisions at  $\sqrt{s_{NN}} =$   
1868 2.76 TeV with ALICE,” *Phys. Rev.* **C88** (2013) 044909, arXiv:1301.4361 [nucl-ex].
- 1869 [41] **ALICE** Collaboration, “ALICE Technical Design Report of the dimuon forward spectrometer,”  
1870 Tech. Rep., 1999. CERN-LHCC-99-22.
- 1871 [42] **ALICE** Collaboration, “ALICE dimuon forward spectrometer: addendum to the Technical  
1872 Design Report,” Tech. Rep., Geneva, 2000. <https://cds.cern.ch/record/494265>.  
1873 ALICE-TDR-5-add-1, CERN-LHCC-2000-046.
- 1874 [43] R. Veenhof, “Garfield - simulation of gaseous detectors, User Guide,” *CERN, W5050* (2010) .  
1875 <http://garfield.web.cern.ch/garfield/>.

- 1876 [44] **ALICE** Collaboration, P. Cortese *et al.*, “ALICE Technical Design Report of Transition  
1877 Radiation Detector,” Tech. Rep., 2001. <https://cds.cern.ch/record/519145>.  
1878 ALICE-TDR-9, CERN-LHCC-2001-021, LYCEN-2001-97.
- 1879 [45] D. Emschermann, *Construction and Performance of the ALICE Transition Radiation Detector*.  
1880 Doctoral thesis, Physikalisches Institut, Ruprecht-Karls-Universität Heidelberg, Heidelberg,  
1881 Germany, 2010.
- 1882 [46] **ALICE** Collaboration, C. Adler *et al.*, “Position reconstruction in drift chambers operated with  
1883 Xe, CO-2 (15%),” *Nucl. Instrum. Meth.* **A540** (2005) 140–157, arXiv:physics/0511233  
1884 [physics].
- 1885 [47] **ALICE TRD** Collaboration, A. Andronic, “Electron identification performance with ALICE  
1886 TRD prototypes,” *Nucl. Instrum. Meth.* **A522** (2004) 40–44, arXiv:physics/0402131  
1887 [physics].
- 1888 [48] **ALICE** Collaboration, A. Andronic *et al.*, “Energy loss of pions and electrons of 1-GeV/c to  
1889 6-GeV/c in drift chambers operated with Xe, CO(2)(15%),” *Nucl. Instrum. Meth.* **A519** (2004)  
1890 508–517, arXiv:physics/0310122 [physics].
- 1891 [49] B. Windelband, “Engineering design review for trd-readout chamber. mechanical design,” Tech.  
1892 Rep. [http://www-alice.gsi.de/trd/docs/edr\\_bernd.ppt](http://www-alice.gsi.de/trd/docs/edr_bernd.ppt).
- 1893 [50] H. Gatz, *Calibration and Alignment of ALICE TRD Super Modules Using Cosmic Ray Data*.  
1894 Diplomarbeit, Institut für Kernphysik, Westfälische Wilhelms-Universität Münster, Münster,  
1895 Germany, 2010.
- 1896 [51] F. Kramer, *Studie zur Messung von Quarkonia mit dem ALICE-TRD und Aufbau eines*  
1897 *Teststandes für seine Ausleseammern*. Diplomarbeit, Institut für Kernphysik, Johann Wolfgang  
1898 Goethe-Universität Frankfurt, Frankfurt, Germany, 2006.
- 1899 [52] C. Baumann, *X-ray Transmission of Radiators for the ALICE-TRD*. Diplomarbeit, Institut für  
1900 Kernphysik, Westfälische Wilhelms-Universität Münster, Münster, Germany, 2005.
- 1901 [53] **ALICE** Collaboration, A. Andronic *et al.*, “Transition radiation spectra of electrons from  
1902 1-GeV/c to 10-GeV/c in regular and irregular radiators,” *Nucl. Instrum. Meth.* **A558** (2006)  
1903 516–525, arXiv:physics/0511229 [physics].
- 1904 [54] R. Brun, F. Carminati, and S. Giani, “GEANT Detector Description and Simulation Tool,” Tech.  
1905 Rep., 1994. CERN-W5013, CERN-W-5013.
- 1906 [55] ALICE Collaboration. <http://aliweb.cern.ch/Offline/AliRoot/Manual.html>.
- 1907 [56] C.Lippmann, K.Oyama and I.Rusanov, “Electronics Integration for the ALICE TRD,” *GSI*  
1908 *Scientific report 2006* (2005) 290.
- 1909 [57] M. Kliemant , H. Appelshäuser , C. Blume , W. Amend , A. Fick , M. Hartig , H. Hinke, M.  
1910 Kessenbrock , F. Kramer , W. Sommer, D. Wegerle and A. Wiesenäcker, “Mass Test and  
1911 Electronics Integration of ALICE TRD chambers at IKF Frankfurt,” *GSI Scientific report 2006*  
1912 (2006) 232.
- 1913 [58] H. Grimm, *Entwicklung eines Gassystems zur Ansteuerung, Überwachung und*  
1914 *Qualitätskontrolle eines ALICE TRD Supermodules*. Diplomarbeit, Institut für Kernphysik,  
1915 Westfälische Wilhelms-Universität Münster, Münster, Germany, 2009.

- 1916 [59] B. Bathen, *Aufbau eines Triggers für Tests der ALICE-TRD-Supermodule mit kosmischer*  
1917 *Strahlung*. Diplomarbeit, Institut für Kernphysik, Westfälische Wilhelms-Universität Münster,  
1918 Münster, Germany, 2007.
- 1919 [60] J. Anielski, *Entwicklung eines Triggersystems zum Testen und Kalibrieren der Supermodule des*  
1920 *ALICE-TRD*. Diplomarbeit, Institut für Kernphysik, Westfälische Wilhelms-Universität Münster,  
1921 Münster, Germany, 2011.
- 1922 [61] S. Wulff, *Position Resolution and Zero Suppression of the ALICE TRD*. Diplomarbeit, Institut für  
1923 Kernphysik, Westfälische Wilhelms-Universität Münster, Münster, Germany, 2009.
- 1924 [62] E. Sicking, *Alignment of ALICE TRD Modules Using Cosmic Ray Data*. Diplomarbeit, Institut  
1925 für Kernphysik, Westfälische Wilhelms-Universität Münster, Münster, Germany, 2009.
- 1926 [63] M. Walter, *Performance of Online Tracklet Reconstruction with the ALICE TRD*. Diplomarbeit,  
1927 Institut für Kernphysik, Westfälische Wilhelms-Universität Münster, Münster, Germany, 2010.
- 1928 [64] B. Albrecht, *Gain Calibration of ALICE TRD Modules Using Cosmic Ray Data*. Diplomarbeit,  
1929 Institut für Kernphysik, Westfälische Wilhelms-Universität Münster, Münster, Germany, 2010.
- 1930 [65] C. Wittweg, *Gas Gain Calibration of an ALICE TRD Supermodule Using Cosmic Rays*.  
1931 Bachelor thesis, Institut für Kernphysik, Westfälische Wilhelms-Universität Münster, Münster,  
1932 Germany, 2014.
- 1933 [66] J. Klein, *Commissioning of and Preparations for Physics with the Transition Radiation Detector*  
1934 *in A Large Ion Collider Experiment at CERN*. Diplomarbeit, Physikalisches Institut,  
1935 Ruprecht-Karls-Universität Heidelberg, Heidelberg, Germany, 2008.
- 1936 [67] Pimenta dos Santos, M., “ALICE TRD and TPC Thermal screen cooling system ,”  
1937 *CERN-ST/CV-2003-490544* (2003) .
- 1938 [68] **CERES** Collaboration, D. Adamova *et al.*, “The CERES/NA45 Radial Drift Time Projection  
1939 Chamber,” *Nucl. Instrum. Meth.* **A593** (2008) 203–231, arXiv:0802.1443 [nucl-ex].
- 1940 [69] ISEG Spezialelektronik GmbH, “Bautzner Landstrasse 23, D-01454 Radeberg, Germany,”  
1941 <http://www.iseg-hv.com/de/>.
- 1942 [70] T. Krawutschke, “A flexible and reliable embedded system for detector control in a high energy  
1943 physics experiment,” *FPL IEEE* (2008) 155–160.
- 1944 [71] J. Klein, *Jet Physics with A Large Ion Collider Experiment at the Large Hadron Collider*.  
1945 Doctoral thesis, Physikalisches Institut, Ruprecht-Karls-Universität Heidelberg, Heidelberg,  
1946 Germany, 2014.
- 1947 [72] **ALICE** Collaboration, C. Fabjan *et al.*, “ALICE Technical Design Report of the Trigger Data  
1948 Acquisition High-Level Trigger and Control System,” Tech. Rep., 2004.  
1949 <https://cds.cern.ch/record/684651>. ALICE-TDR-10, CERN-LHCC-2003-062.
- 1950 [73] **ALICE** Collaboration, Fabjan, C. *et al.*, “ALICE trigger data-acquisition high-level trigger and  
1951 control system: Technical Design Report,” Tech. Rep., 2004.  
1952 <https://cds.cern.ch/record/684651>.
- 1953 [74] S. Zimmer, *Design, Implementation and Commissioning of the Pretrigger System for the*  
1954 *Transition Radiation Detector at the ALICE experiment of CERN*. Diplomarbeit, Physikalisches  
1955 Institut, Ruprecht-Karls-Universität Heidelberg, Heidelberg, Germany, 2008.

- 1956 [75] S. Schmiederer, *Development and Implementation of the Control System for the Pre-Trigger*  
 1957 *System of the Transition Radiation Detector at ALICE*. Diplomarbeit, Physikalisches Institut,  
 1958 Ruprecht-Karls-Universität Heidelberg, Heidelberg, Germany, 2009.
- 1959 [76] S. Klewin, *Development and Commissioning of the Trigger System Upgrade for the ALICE*  
 1960 *Transition Radiation Detector at the LHC at CERN*. Master thesis, Physikalisches Institut,  
 1961 Ruprecht-Karls-Universität Heidelberg, Heidelberg, Germany, 2015.
- 1962 [77] H. K. Soltveit, J. Stachel, P. Braun-Munzinger, L. Musa, H. A. Gustafsson, U. Bonnes,  
 1963 H. Oeschler, L. Osterman, and S. Lang, “The Preamplifier shaper for the ALICE TPC-Detector,”  
 1964 *Nucl. Instrum. Meth.* **A676** (2012) 106–119, arXiv:1203.3564 [physics.ins-det].
- 1965 [78] **ALICE TRD** Collaboration, V. Angelov, “Design and performance of the ALICE TRD front-end  
 1966 electronics,” *Nucl. Instrum. Meth.* **A563** (2006) 317–320.
- 1967 [79] “ETM professional control GmbH, A Siemens company, Kasernenstasse 29, A-7000, Eisenstadt,  
 1968 Austria.”.
- 1969 [80] Simatic WinCC Open Architecture, developed by ETM GmbH.  
 1970 [http://www.etm.at/index\\_e.asp?id=2](http://www.etm.at/index_e.asp?id=2).
- 1971 [81] S. Schmeling, “Common tools for large experiment controls - a common approach for  
 1972 deployment, maintenance and support,” *IEEE Trans. Nucl. Sci.* **53 No. 3** (2006) 970–973.
- 1973 [82] C. Gaspar, M. Doenzelmann, Ph. Charpentier, “DIM, a portable, light weight package for  
 1974 information publishing, data transfer and inter-process communication,” *Comp. Phys. Comm.*  
 1975 **140** (2001) 102–109.
- 1976 [83] R. Bailey and P. Collier, “Standard Filling Schemes for Various LHC Operation Modes,” Tech.  
 1977 Rep. LHC-PROJECT-NOTE-323, CERN, Geneva, Sep, 2003.  
 1978 <https://cds.cern.ch/record/691782>. LHC-PROJECT-NOTE-323.
- 1979 [84] L. Bergmann, *Studies of the Gain and Drift Velocity for the ALICE Transition Radiation Detector*  
 1980 *at the CERN LHC*. Bachelor Thesis, Physikalisches Institut, Ruprecht-Karls-Universität  
 1981 Heidelberg, Heidelberg, Germany, 2017.
- 1982 [85] A. Andronic et al., “Drift velocity and gain in argon- and xenon-based mixtures,” *Nucl. Instrum.*  
 1983 *Meth.* **523** no. 3, (2004) 302 – 308.
- 1984 [86] **ALICE** Collaboration, J. F. Grosse-Oetringhaus, C. Zampolli, A. Colla, and F. Carminati, “The  
 1985 ALICE online-offline framework for the extraction of conditions data,” *J. Phys.: Conf. Ser.* **219**  
 1986 (2010) 022010. <https://cds.cern.ch/record/1269925>.
- 1987 [87] **ALICE** Collaboration, A. Colla and J. Grosse-Oetringhaus, “The Shuttle Framework – a System  
 1988 for Automatic Readout and Processing of Conditions Data,” ALICE-INT-2008-011,  
 1989 <https://edms.cern.ch/document/924807>.
- 1990 [88] A. Ferrari, P. R. Sala, A. Fasso, and J. Ranft, “FLUKA: A multi-particle transport code (Program  
 1991 version 2005),”.
- 1992 [89] **ALICE** Collaboration, K. Aamodt *et al.*, “Charged-particle multiplicity measurement in  
 1993 proton-proton collisions at  $\sqrt{s} = 0.9$  and 2.36 TeV with ALICE at LHC,” *Eur. Phys. J.* **C68**  
 1994 (2010) 89–108, arXiv:1004.3034 [hep-ex].



- 1995 [90] **ALICE** Collaboration, B. Abelev *et al.*, “Pseudorapidity density of charged particles in p + Pb  
1996 collisions at  $\sqrt{s_{NN}} = 5.02$  TeV,” *Phys. Rev. Lett.* **110** no. 3, (2013) 032301, arXiv:1210.3615  
1997 [nucl-ex].
- 1998 [91] **ALICE** Collaboration, K. Aamodt *et al.*, “Charged-particle multiplicity density at mid-rapidity  
1999 in central Pb-Pb collisions at  $\sqrt{s_{NN}} = 2.76$  TeV,” *Phys. Rev. Lett.* **105** (2010) 252301,  
2000 arXiv:1011.3916 [nucl-ex].
- 2001 [92] **ALICE** Collaboration, J. Adam *et al.*, “Pseudorapidity and transverse-momentum distributions  
2002 of charged particles in proton–proton collisions at  $\sqrt{s} = 13$  TeV,” *Phys. Lett.* **B753** (2016)  
2003 319–329, arXiv:1509.08734 [nucl-ex].
- 2004 [93] **ALICE** Collaboration, J. Adam *et al.*, “Charged-particle multiplicities in proton–proton  
2005 collisions at  $\sqrt{s} = 0.9$  to 8 TeV,” *Eur. Phys. J.* **C77** (2017) 33, arXiv:1509.07541 [nucl-ex].
- 2006 [94] **ALICE** Collaboration, J. Adam *et al.*, “Multiplicity and transverse momentum evolution of  
2007 charge-dependent correlations in pp, p–Pb, and Pb–Pb collisions at the LHC,” *Eur. Phys. J.* **C76**  
2008 (2016) 86, arXiv:1509.07255 [nucl-ex].
- 2009 [95] **ALICE DQM** Collaboration, B. von Haller, F. Bellini, A. Telesca, and Y. Foka, “The ALICE  
2010 Data Quality Monitoring: qualitative and quantitative review of three years of operations,” *J.*  
2011 *Phys. Conf. Ser.* **513** (2014) 012038.
- 2012 [96] J. Jowett, “Collision Schedules and Bunch Filling Schemes in the LHC,” Tech. Rep., 1999.  
2013 LHC-PROJECT-NOTE-179.
- 2014 [97] M. Fleck, *Commissioning a gas chromatograph for automatic measurements of gas compositions*  
2015 *in the ALICE TPC and TRD and measurement of electrons from semi-leptonic heavy-flavour*  
2016 *hadron decays in p-Pb collisions at  $\sqrt{s_{NN}} = 5.02$  TeV with the ALICE TRD.* Master Thesis,  
2017 Physikalisches Institut, Ruprecht-Karls-Universität Heidelberg, Heidelberg, Germany, 2014.
- 2018 [98] P. Billoir, “Track Fitting With Multiple Scattering: A New Method,” *Nucl. Instrum. Meth.* **A225**  
2019 (1984) 352–366.
- 2020 [99] V. Blobel and C. Kleinwort, “A New method for the high precision alignment of track detectors,”  
2021 arXiv:hep-ex/0208021 [hep-ex].
- 2022 [100] **ALICE** Collaboration, S. Chapeland *et al.*, “Online processing in the ALICE DAQ. The detector  
2023 algorithms,” *J. Phys. Conf. Ser.* **219** (2010) 022004.
- 2024 [101] **ALEPH** Collaboration, D. Decamp *et al.*, “ALEPH: A detector for electron-positron  
2025 annihilations at LEP,” *Nucl. Instrum. Meth.* **A294** (1990) 121–178. Erratum: *Nucl. Instrum.*  
2026 *Meth.*A303,393(1991).
- 2027 [102] **ALEPH** Collaboration, W. Blum, *The ALEPH handbook: 1989.* CERN, Geneva, 1989.  
2028 <https://cds.cern.ch/record/227125>.
- 2029 [103] A. De Min *et al.*, “Performance of the HPC calorimeter in DELPHI,” *IEEE Trans. Nucl. Sci.* **42**  
2030 (1995) 491–498.
- 2031 [104] M. A. Helwi, *Gain Calibration of the ALICE Transition Radiation Detector with Krypton-83.*  
2032 Diplomarbeit, Physikalisches Institut, Ruprecht-Karls-Universität Heidelberg, Heidelberg,  
2033 Germany, 2010.

- 2034 [105] J. H. Stiller, *Gain Calibration of the ALICE TRD using the Decay of  $^{83m}\text{Kr}$  and Alignment of the*  
2035 *ALICE TRD*. Diplomarbeit, Physikalisches Institut, Ruprecht-Karls-Universität Heidelberg,  
2036 Heidelberg, Germany, 2011.
- 2037 [106] **ALICE TRD** Collaboration, R. Bailhache and C. Lippmann, “New test beam results with  
2038 prototypes of the ALICE TRD,” *Nucl. Instrum. Meth.* **A563** (2006) 310–313.
- 2039 [107] M. Fasel, *Single-electron analysis and open charm cross section in proton-proton collisions at*  
2040  *$\sqrt{s} = 7 \text{ TeV}$* . Doctoral thesis, Technische Universität Darmstadt, Darmstadt, Germany, 2012.
- 2041 [108] X. Lu, *Exploring the performance limits of the ALICE Time Projection Chamber and Transition*  
2042 *Radiation Detector for measuring identified hadron production at the LHC*. Doctoral thesis,  
2043 Physikalisches Institut, Ruprecht-Karls-Universität Heidelberg, Heidelberg, Germany, 2013.
- 2044 [109] **ALICE** Collaboration, X.-G. Lu, “Energy Loss Signals in the ALICE TRD,” *Nucl. Instrum.*  
2045 *Meth.* **A706** (2013) 16–19, arXiv:1204.1218 [physics.ins-det].
- 2046 [110] W. Blum, W. Riegler, and L. Rolandi, *Particle Detection with Drift Chambers*. Springer-Verlag,  
2047 2nd ed., 2008.
- 2048 [111] D. Lohner, *Anisotropic flow of direct photons in Pb-Pb collisions at 2.76 TeV per nucleon*.  
2049 Doctoral thesis, Physikalisches Institut, Ruprecht-Karls-Universität Heidelberg, Heidelberg,  
2050 Germany, 2013.
- 2051 [112] M. Kroesen, *Electron Identification with the ALICE TRD using Multivariate Analysis*  
2052 *Techniques*. Master Thesis, Physikalisches Institut, Ruprecht-Karls-Universität Heidelberg,  
2053 Heidelberg, Germany, 2017.
- 2054 [113] A. Wilk, *Particle Identification Using Artificial Neural Networks with the ALICE Transition*  
2055 *Radiation Detector*. Doctoral thesis, Institut für Kernphysik, Westfälische Wilhelms-Universität  
2056 Münster, Münster, Germany, 2010.
- 2057 [114] **ALICE** Collaboration, C. Adler *et al.*, “Electron / pion identification with ALICE TRD  
2058 prototypes using a neural network algorithm,” *Nucl. Instrum. Meth.* **A552** (2005) 364–371.
- 2059 [115] **ALICE** Collaboration. <http://aliweb.cern.ch/Offline/>.
- 2060 [116] **ALICE** Collaboration, B. Abelev *et al.*, “Measurement of electrons from semileptonic  
2061 heavy-flavour hadron decays in pp collisions at  $\sqrt{s} = 7 \text{ TeV}$ ,” *Phys. Rev.* **D86** (2012) 112007,  
2062 arXiv:1205.5423 [hep-ex].
- 2063 [117] **ALICE** Collaboration, J. Adam *et al.*, “Particle identification in ALICE: a Bayesian approach,”  
2064 *Eur. Phys. J. Plus* **131** no. 5, (2016) 168, arXiv:1602.01392 [physics.data-an].
- 2065 [118] J. de Cuveland, “Entwicklung der globalen Spurrekonstruktionseinheit für den  
2066 ALICE-Übergangsstrahlungsdetektor am LHC (CERN),” diplomarbeit, Kirchhoff-Institut für  
2067 Physik, Ruprecht-Karls-Universität Heidelberg, Heidelberg, Germany, 2003.
- 2068 [119] M. Cacciari, G. P. Salam, and G. Soyez, “FastJet user manual,” *Eur.Phys.J.* **C72** (2012) 1896,  
2069 arXiv:1111.6097 [hep-ph].
- 2070 [120] O. Schmidt, *Simulation and commissioning of the rejection of late conversions in the TRD*  
2071 *triggers of ALICE*. Master Thesis, Physikalisches Institut, Ruprecht-Karls-Universität  
2072 Heidelberg, Heidelberg, Germany, 2016.

2073 **A The ALICE Collaboration**

2074 S. Acharya<sup>137</sup>, J. Adam<sup>96</sup>, D. Adamová<sup>93</sup>, C. Adler<sup>103</sup>, J. Adolfsson<sup>32</sup>, M.M. Aggarwal<sup>98</sup>, G. Aglieri  
2075 Rinella<sup>33</sup>, M. Agnello<sup>29</sup>, N. Agrawal<sup>46</sup>, Z. Ahammed<sup>137</sup>, N. Ahmad<sup>15</sup>, S.U. Ahn<sup>78</sup>, S. Aiola<sup>141</sup>,  
2076 A. Akindinov<sup>63</sup>, M. Al-Turany<sup>106</sup>, S.N. Alam<sup>137</sup>, D. Antonczyk<sup>69</sup>, A. Arend<sup>69</sup>, J.L.B. Alba<sup>111</sup>,  
2077 D.S.D. Albuquerque<sup>122</sup>, D. Aleksandrov<sup>89</sup>, B. Alessandro<sup>57</sup>, R. Alfaro Molina<sup>73</sup>, A. Alici<sup>11,25,52</sup>, A. Alkin<sup>3</sup>,  
2078 J. Alme<sup>20</sup>, T. Alt<sup>69</sup>, L. Altenkamper<sup>20</sup>, I. Altsybeev<sup>136</sup>, C. Alves Garcia Prado<sup>121</sup>, C. Andrei<sup>86</sup>, D. Andreou<sup>33</sup>,  
2079 H.A. Andrews<sup>110</sup>, A. Andronic<sup>106</sup>, V. Anguelov<sup>103</sup>, C. Anson<sup>96</sup>, T. Antičić<sup>107</sup>, F. Antinori<sup>55</sup>, P. Antonioli<sup>52</sup>,  
2080 R. Anwar<sup>124</sup>, L. Aphecetche<sup>114</sup>, H. Appelshäuser<sup>69</sup>, S. Arcelli<sup>25</sup>, R. Arnaldi<sup>57</sup>, O.W. Arnold<sup>104,34</sup>,  
2081 I.C. Arsene<sup>19</sup>, M. Arslanodok<sup>103</sup>, B. Audurier<sup>114</sup>, A. Augustinus<sup>33</sup>, R. Averbeck<sup>106</sup>, M.D. Azmi<sup>15</sup>, A. Badalà<sup>54</sup>,  
2082 Y.W. Baek<sup>59,77</sup>, S. Bagnasco<sup>57</sup>, R. Bailhache<sup>69</sup>, R. Bala<sup>100</sup>, A. Baldisseri<sup>74</sup>, M. Ball<sup>43</sup>, R.C. Baral<sup>66</sup>,  
2083 A.M. Barbano<sup>24</sup>, R. Barbera<sup>26</sup>, F. Barile<sup>31,51</sup>, L. Barioglio<sup>24</sup>, G.G. Barnaföldi<sup>140</sup>, L.S. Barnby<sup>92</sup>, V. Barret<sup>131</sup>,  
2084 P. Bartalini<sup>7</sup>, K. Barth<sup>33</sup>, D. Bartos<sup>86</sup>, E. Bartsch<sup>69</sup>, M. Basile<sup>25</sup>, N. Bastid<sup>131</sup>, S. Basu<sup>139</sup>, B. Bathen<sup>70</sup>,  
2085 G. Batigne<sup>114</sup>, B. Battyanya<sup>76</sup>, P.C. Batzing<sup>19</sup>, C. Baumann<sup>69</sup>, I.G. Bearden<sup>90</sup>, H. Beck<sup>103</sup>, C. Bedda<sup>62</sup>,  
2086 N.K. Behera<sup>59</sup>, I. Belikov<sup>133</sup>, F. Bellini<sup>25,33</sup>, H. Bello Martinez<sup>2</sup>, R. Bellwied<sup>124</sup>, L.G.E. Beltran<sup>120</sup>,  
2087 V. Belyaev<sup>82</sup>, G. Bencedi<sup>140</sup>, S. Beole<sup>24</sup>, I. Berceanu<sup>86</sup>, A. Bercuci<sup>86</sup>, Y. Berdnikov<sup>95</sup>, D. Berenyi<sup>140</sup>,  
2088 R.A. Bertens<sup>127</sup>, D. Berzano<sup>33</sup>, L. Betev<sup>33</sup>, A. Bhasin<sup>100</sup>, I.R. Bhat<sup>100</sup>, A.K. Bhati<sup>98</sup>, B. Bhattacharjee<sup>42</sup>,  
2089 J. Bhom<sup>118</sup>, A. Bianchi<sup>24</sup>, L. Bianchi<sup>124</sup>, N. Bianchi<sup>49</sup>, C. Bianchin<sup>139</sup>, J. Bielčik<sup>37</sup>, J. Bielčíková<sup>93</sup>,  
2090 A. Bilandzic<sup>104,34</sup>, G. Biro<sup>140</sup>, R. Biswas<sup>4</sup>, S. Biswas<sup>4</sup>, J.T. Blair<sup>119</sup>, D. Blau<sup>89</sup>, C. Blume<sup>69</sup>, G. Boca<sup>134</sup>,  
2091 F. Bock<sup>81,33,103</sup>, A. Bogdanov<sup>82</sup>, L. Boldizsár<sup>140</sup>, M. Bombara<sup>38</sup>, G. Bonomi<sup>135</sup>, M. Bonora<sup>33</sup>, J. Book<sup>69</sup>,  
2092 H. Borel<sup>74</sup>, A. Borissov<sup>17</sup>, M. Borri<sup>126</sup>, E. Botta<sup>24</sup>, C. Bourjau<sup>90</sup>, L. Bratrud<sup>69</sup>, P. Braun-Munzinger<sup>106</sup>,  
2093 M. Bregant<sup>121</sup>, T.A. Broker<sup>69</sup>, M. Broz<sup>37</sup>, E.J. Brucken<sup>44</sup>, E. Bruna<sup>57</sup>, G.E. Bruno<sup>31</sup>, D. Bucher<sup>70</sup>,  
2094 D. Budnikov<sup>108</sup>, H. Buesching<sup>69</sup>, S. Bufalino<sup>29</sup>, P. Buhler<sup>113</sup>, P. Buncic<sup>33</sup>, O. Busch<sup>130</sup>, Z. Buthelezi<sup>75</sup>,  
2095 J.B. Butt<sup>14</sup>, J.T. Buxton<sup>16</sup>, J. Cabala<sup>116</sup>, D. Caffarri<sup>33,91</sup>, H. Caines<sup>141</sup>, A. Caliva<sup>62</sup>, E. Calvo Villar<sup>111</sup>,  
2096 P. Camerini<sup>23</sup>, A.A. Capon<sup>113</sup>, G. Caragheorghopol<sup>86</sup>, F. Carena<sup>33</sup>, W. Carena<sup>33</sup>, F. Carnescchi<sup>25,11</sup>,  
2097 J. Castillo Castellanos<sup>74</sup>, A.J. Castro<sup>127</sup>, E.A.R. Casula<sup>53</sup>, V. Catanescu<sup>86</sup>, C. Ceballos Sanchez<sup>9</sup>, P. Cerello<sup>57</sup>,  
2098 S. Chandra<sup>137</sup>, B. Chang<sup>125</sup>, S. Chapeland<sup>33</sup>, M. Chartier<sup>126</sup>, S. Chattopadhyay<sup>137</sup>, S. Chattopadhyay<sup>109</sup>,  
2099 A. Chauvin<sup>34,104</sup>, S. Chernenko<sup>76</sup>, M. Cherney<sup>96</sup>, C. Cheshkov<sup>132</sup>, B. Cheynis<sup>132</sup>, V. Chibante Barroso<sup>33</sup>,  
2100 D.D. Chinellato<sup>122</sup>, S. Cho<sup>59</sup>, P. Chochula<sup>33</sup>, M. Chojnacki<sup>90</sup>, S. Choudhury<sup>137</sup>, T. Chowdhury<sup>131</sup>,  
2101 P. Christakoglou<sup>91</sup>, C.H. Christensen<sup>90</sup>, P. Christiansen<sup>32</sup>, T. Chujo<sup>130</sup>, S.U. Chung<sup>17</sup>, C. Cicalo<sup>53</sup>,  
2102 L. Cifarelli<sup>11,25</sup>, F. Cindolo<sup>52</sup>, M. Ciobanu<sup>86</sup>, J. Cleymans<sup>99</sup>, F. Colamaria<sup>31</sup>, D. Colella<sup>33,51,64</sup>, A. Collu<sup>81</sup>,  
2103 M. Colocci<sup>25</sup>, M. Concas<sup>57,ii</sup>, G. Conesa Balbastre<sup>80</sup>, Z. Conesa del Valle<sup>60</sup>, M.E. Connors<sup>141,iii</sup>,  
2104 J.G. Contreras<sup>37</sup>, T.M. Cormier<sup>94</sup>, Y. Corrales Morales<sup>57</sup>, I. Cortés Maldonado<sup>2</sup>, P. Cortese<sup>30</sup>,  
2105 M.R. Consentino<sup>123</sup>, F. Costa<sup>33</sup>, S. Costanza<sup>134</sup>, J. Crkovská<sup>60</sup>, P. Crochet<sup>131</sup>, E. Cuaute<sup>71</sup>, L. Cunqueiro<sup>70</sup>,  
2106 T. Dahms<sup>34,104</sup>, A. Dainese<sup>55</sup>, M.C. Danisch<sup>103</sup>, A. Danu<sup>67</sup>, D. Das<sup>109</sup>, I. Das<sup>109</sup>, S. Das<sup>4</sup>, A. Dash<sup>87</sup>,  
2107 S. Dash<sup>46</sup>, H. Daues<sup>106</sup>, S. De<sup>121,47</sup>, A. De Caro<sup>28</sup>, G. de Cataldo<sup>51</sup>, C. de Conti<sup>121</sup>, J. de Cuveland<sup>iv</sup>, A. De  
2108 Falco<sup>22</sup>, D. De Gruttola<sup>28,11</sup>, N. De Marco<sup>57</sup>, S. De Pasquale<sup>28</sup>, R.D. De Souza<sup>122</sup>, H.F. Degenhardt<sup>121</sup>,  
2109 A. Deisting<sup>106,103</sup>, A. Deloff<sup>85</sup>, C. Deplano<sup>91</sup>, A. Devismes<sup>106</sup>, P. Dhankher<sup>46</sup>, D. Di Bari<sup>31</sup>, A. Di Mauro<sup>33</sup>,  
2110 P. Di Nezza<sup>49</sup>, B. Di Ruzza<sup>55</sup>, T. Dietel<sup>99</sup>, P. Dillenseger<sup>69</sup>, R. Divià<sup>33</sup>, Ø. Djuvsland<sup>20</sup>, A. Dobrin<sup>33</sup>,  
2111 D. Domenicis Gimenez<sup>121</sup>, B. Dönigus<sup>69</sup>, O. Dordic<sup>19</sup>, L.V.V. Doremalen<sup>62</sup>, A.K. Dubey<sup>137</sup>, A. Dubla<sup>106</sup>,  
2112 L. Ducroux<sup>132</sup>, A.K. Duggal<sup>98</sup>, P. Dupieux<sup>131</sup>, V. Duta<sup>86</sup>, R.J. Ehlers<sup>141</sup>, D. Elia<sup>51</sup>, D. Emschermann<sup>103</sup>,  
2113 E. Endress<sup>111</sup>, H. Engel<sup>68</sup>, E. Epple<sup>141</sup>, B. Erazmus<sup>114</sup>, F. Erhardt<sup>97</sup>, B. Espagnon<sup>60</sup>, S. Esumi<sup>130</sup>,  
2114 G. Eulisse<sup>33</sup>, J. Eum<sup>17</sup>, D. Evans<sup>110</sup>, S. Evdokimov<sup>112</sup>, L. Fabbietti<sup>104,34</sup>, J. Favre<sup>80</sup>, A. Fantoni<sup>49</sup>,  
2115 M. Fasel<sup>94,81</sup>, O. Fateev<sup>76</sup>, L. Feldkamp<sup>70</sup>, A. Feliciello<sup>57</sup>, G. Feofilov<sup>136</sup>, J. Ferencei<sup>93</sup>, A. Fernández  
2116 Téllez<sup>2</sup>, A. Ferretti<sup>24</sup>, A. Festanti<sup>33,27</sup>, V.J.G. Feuillard<sup>131,74</sup>, J. Figiel<sup>118</sup>, M.A.S. Figueredo<sup>121</sup>,  
2117 S. Filchagin<sup>108</sup>, D. Finogeev<sup>61</sup>, F.M. Fionda<sup>20,22</sup>, M. Fleck<sup>103</sup>, M. Floris<sup>33</sup>, S. Foertsch<sup>75</sup>, P. Foka<sup>106</sup>,  
2118 S. Fokin<sup>89</sup>, E. Fragiaco<sup>58</sup>, A. Francescon<sup>33</sup>, A. Francisco<sup>114</sup>, U. Frankenfeld<sup>106</sup>, S. Freuen<sup>103</sup>,  
2119 G.G. Fronze<sup>24</sup>, U. Fuchs<sup>33</sup>, C. Furget<sup>80</sup>, A. Furs<sup>61</sup>, M. Fusco Girard<sup>28</sup>, J.J. Gaardhøje<sup>90</sup>, M. Gagliardi<sup>24</sup>,  
2120 A.M. Gago<sup>111</sup>, K. Gajdosova<sup>90</sup>, M. Gallio<sup>24</sup>, C.D. Galvan<sup>120</sup>, P. Ganoti<sup>84</sup>, C. Garabatos<sup>106</sup>, E. Garcia-Solis<sup>12</sup>,  
2121 K. Garg<sup>26</sup>, C. Gargiulo<sup>33</sup>, P. Gasik<sup>34,104</sup>, H. Gatz<sup>70</sup>, E.F. Gauger<sup>119</sup>, M.B. Gay Ducati<sup>72</sup>, M. Germain<sup>114</sup>,  
2122 J. Ghosh<sup>109</sup>, P. Ghosh<sup>137</sup>, S.K. Ghosh<sup>4</sup>, P. Gianotti<sup>49</sup>, G. Giolu<sup>86</sup>, P. Giubellino<sup>106,57,33</sup>, P. Giubilato<sup>27</sup>,  
2123 E. Gladysz-Dziadus<sup>118</sup>, R. Glasow<sup>70,i</sup>, P. Glässel<sup>103</sup>, S. Gremmler<sup>70</sup>, D.M. Gómez Coral<sup>73</sup>, A. Gomez  
2124 Ramirez<sup>68</sup>, A.S. Gonzalez<sup>33</sup>, S. Gorbunov<sup>40</sup>, L. Görlich<sup>118</sup>, S. Gotovac<sup>117</sup>, D. Gottschalk<sup>103</sup>, H. Gottschlag<sup>70</sup>,  
2125 V. Grabski<sup>73</sup>, L.K. Graczykowski<sup>138</sup>, K.L. Graham<sup>110</sup>, R. Grajcarek<sup>103</sup>, L. Greiner<sup>81</sup>, A. Grelli<sup>62</sup>,  
2126 C. Grigoras<sup>33</sup>, V. Grigoriev<sup>82</sup>, A. Grigoryan<sup>1</sup>, S. Grigoryan<sup>76</sup>, H. Grimm<sup>70</sup>, N. Grion<sup>58</sup>, J.M. Gronefeld<sup>106</sup>,  
2127 F. Grosa<sup>29</sup>, J.F. Grosse-Oetringhaus<sup>33</sup>, R. Grosso<sup>106</sup>, L. Gruber<sup>113</sup>, F. Guber<sup>61</sup>, R. Guernane<sup>80</sup>, B. Guerzoni<sup>25</sup>,  
2128 K. Gulbrandsen<sup>90</sup>, T. Gunji<sup>129</sup>, A. Gupta<sup>100</sup>, R. Gupta<sup>100</sup>, M. Gutfleisch<sup>106</sup>, I.B. Guzman<sup>2</sup>, R. Haake<sup>33</sup>,

- 2129 C. Hadjidakis<sup>60</sup>, H. Hamagaki<sup>83</sup>, G. Hamar<sup>140</sup>, J.C. Hamon<sup>133</sup>, M.R. Haque<sup>62</sup>, J.W. Harris<sup>141</sup>, M. Hartig<sup>69</sup>,  
2130 A. Harton<sup>12</sup>, H. Hassan<sup>80</sup>, D. Hatzifotiadou<sup>11,52</sup>, S. Hayashi<sup>129</sup>, S.T. Heckel<sup>69</sup>, J. Hehner<sup>106</sup>, M. Heide<sup>70</sup>,  
2131 E. Hellbär<sup>69</sup>, H. Helstrup<sup>35</sup>, A. Herghelegiu<sup>86</sup>, G. Herrera Corral<sup>10</sup>, F. Herrmann<sup>70</sup>, N. Herrmann<sup>103</sup>,  
2132 B.A. Hess<sup>102</sup>, K.F. Hetland<sup>35</sup>, H. Hillemanns<sup>33</sup>, C. Hills<sup>126</sup>, B. Hippolyte<sup>133</sup>, J. Hladky<sup>65</sup>, B. Hohlweger<sup>104</sup>,  
2133 D. Horak<sup>37</sup>, S. Hornung<sup>106</sup>, R. Hosokawa<sup>130,80</sup>, P. Hristov<sup>33</sup>, S. Huber<sup>106</sup>, C. Hughes<sup>127</sup>, T.J. Humanic<sup>16</sup>,  
2134 N. Hussain<sup>42</sup>, T. Hussain<sup>15</sup>, D. Hutter<sup>40</sup>, D.S. Hwang<sup>18</sup>, S.A. Iga Buitron<sup>71</sup>, R. Ilkaev<sup>108</sup>, M. Inaba<sup>130</sup>,  
2135 M. Ippolitov<sup>82,89</sup>, M. Irfan<sup>15</sup>, M.S. Islam<sup>109</sup>, M. Ivanov<sup>106</sup>, V. Ivanov<sup>95</sup>, V. Izucheev<sup>112</sup>, B. Jacak<sup>81</sup>,  
2136 N. Jacazio<sup>25</sup>, P.M. Jacobs<sup>81</sup>, M.B. Jadhav<sup>46</sup>, J. Jadlovsky<sup>116</sup>, S. Jaelani<sup>62</sup>, C. Jahnke<sup>34</sup>, M.J. Jakubowska<sup>138</sup>,  
2137 M.A. Janik<sup>138</sup>, P.H.S.Y. Jayarathna<sup>124</sup>, C. Jena<sup>87</sup>, S. Jena<sup>124</sup>, M. Jercic<sup>97</sup>, R.T. Jimenez Bustamante<sup>106</sup>,  
2138 P.G. Jones<sup>110</sup>, A. Jusko<sup>110</sup>, P. Kalinak<sup>64</sup>, A. Kalweit<sup>33</sup>, J.H. Kang<sup>142</sup>, V. Kaplin<sup>82</sup>, S. Kar<sup>137</sup>, A. Karasu  
2139 Uysal<sup>79</sup>, O. Karavichev<sup>61</sup>, T. Karavicheva<sup>61</sup>, L. Karayan<sup>106,103</sup>, P. Karczmarczyk<sup>33</sup>, E. Karpechev<sup>61</sup>,  
2140 U. Keschull<sup>68</sup>, R. Keidel<sup>143</sup>, D.L.D. Keijdener<sup>62</sup>, M. Keil<sup>33</sup>, B. Ketzer<sup>43</sup>, Z. Khabanova<sup>91</sup>, P. Khan<sup>109</sup>,  
2141 S.A. Khan<sup>137</sup>, A. Khanzadeev<sup>95</sup>, Y. Kharlov<sup>112</sup>, A. Khatun<sup>15</sup>, A. Khuntia<sup>47</sup>, M.M. Kielbowicz<sup>118</sup>, B. Kileng<sup>35</sup>,  
2142 B. Kim<sup>130</sup>, D. Kim<sup>142</sup>, D.J. Kim<sup>125</sup>, H. Kim<sup>142</sup>, J.S. Kim<sup>41</sup>, J. Kim<sup>103</sup>, M. Kim<sup>59</sup>, M. Kim<sup>142</sup>, S. Kim<sup>18</sup>,  
2143 T. Kim<sup>142</sup>, S. Kirsch<sup>40</sup>, I. Kisel<sup>40</sup>, S. Kiselev<sup>63</sup>, A. Kisiel<sup>138</sup>, E. Kislov<sup>76</sup>, G. Kiss<sup>140</sup>, J.L. Klay<sup>6</sup>, C. Klein<sup>69</sup>,  
2144 J. Klein<sup>33</sup>, C. Klein-Bösing<sup>70</sup>, M. Klein-Bösing<sup>70</sup>, M. Kliemant<sup>69</sup>, H. Klingenmeyer<sup>103</sup>, S. Klewin<sup>103</sup>,  
2145 A. Kluge<sup>33</sup>, M.L. Knichel<sup>33,103</sup>, A.G. Knospe<sup>124</sup>, C. Kobdaj<sup>115</sup>, M. Kofarago<sup>140</sup>, M. Kohn<sup>70</sup>, T. Kollegger<sup>106</sup>,  
2146 V. Kondratiev<sup>136</sup>, N. Kondratyeva<sup>82</sup>, E. Kondratyuk<sup>112</sup>, A. Konevskikh<sup>61</sup>, M. Konno<sup>130</sup>, M. Konyushikhin<sup>139</sup>,  
2147 M. Kopcik<sup>116</sup>, M. Kour<sup>100</sup>, C. Kouzinopoulos<sup>33</sup>, O. Kovalenko<sup>85</sup>, V. Kovalenko<sup>136</sup>, M. Kowalski<sup>118</sup>,  
2148 G. Koyithatta Meethalevedu<sup>46</sup>, I. Králik<sup>64</sup>, F. Kramer<sup>69</sup>, A. Kravčáková<sup>38</sup>, T. Krawutschke<sup>v</sup>, L. Kreis<sup>106</sup>,  
2149 M. Krivda<sup>64,110</sup>, F. Krizek<sup>93</sup>, D. Krumbhorn<sup>103</sup>, E. Kryshen<sup>95</sup>, M. Krzewicki<sup>40</sup>, A.M. Kubera<sup>16</sup>, V. Kučera<sup>93</sup>,  
2150 C. Kuhn<sup>133</sup>, P.G. Kuijjer<sup>91</sup>, A. Kumar<sup>100</sup>, J. Kumar<sup>46</sup>, L. Kumar<sup>98</sup>, S. Kumar<sup>46</sup>, S. Kundu<sup>87</sup>, P. Kurashvili<sup>85</sup>,  
2151 A. Kurepin<sup>61</sup>, A.B. Kurepin<sup>61</sup>, A. Kuryakin<sup>108</sup>, S. Kushpil<sup>93</sup>, M.J. Kweon<sup>59</sup>, Y. Kwon<sup>142</sup>, S.L. La Pointe<sup>40</sup>,  
2152 P. La Rocca<sup>26</sup>, C. Lagana Fernandes<sup>121</sup>, Y.S. Lai<sup>81</sup>, I. Lakomov<sup>33</sup>, R. Langoy<sup>39</sup>, K. Lapidus<sup>141</sup>, C. Lara<sup>68</sup>,  
2153 A. Lardeux<sup>19,74</sup>, A. Lattuca<sup>24</sup>, E. Laudi<sup>33</sup>, R. Lavicka<sup>37</sup>, R. Lea<sup>23</sup>, L. Leardini<sup>103</sup>, S. Lee<sup>142</sup>, F. Lehas<sup>91</sup>,  
2154 T. Lehmann<sup>103</sup>, J. Lehner<sup>69</sup>, S. Lehner<sup>113</sup>, J. Lehrbach<sup>40</sup>, R.C. Lemmon<sup>92</sup>, V. Lenti<sup>51</sup>, E. Leogrande<sup>62</sup>, I. León  
2155 Monzón<sup>120</sup>, F. Lesser<sup>iv</sup>, P. Lévai<sup>140</sup>, X. Li<sup>13</sup>, J. Lien<sup>39</sup>, R. Lietava<sup>110</sup>, B. Lim<sup>17</sup>, S. Lindal<sup>19</sup>,  
2156 V. Lindenstruth<sup>40</sup>, S.W. Lindsay<sup>126</sup>, C. Lippmann<sup>106</sup>, M.A. Lisa<sup>16</sup>, V. Litichevskiy<sup>44</sup>, W.J. Llope<sup>139</sup>,  
2157 D.F. Lodato<sup>62</sup>, D. Lohner<sup>103</sup>, P.I. Loenne<sup>20</sup>, V. Loginov<sup>82</sup>, C. Loizides<sup>81</sup>, P. Loncar<sup>117</sup>, X. Lopez<sup>131</sup>, E. López  
2158 Torres<sup>9</sup>, A. Lowe<sup>140</sup>, X. Lu<sup>103</sup>, W. Ludolphs<sup>103</sup>, P. Luettig<sup>69</sup>, J.R. Luhder<sup>70</sup>, M. Lunardon<sup>27</sup>,  
2159 G. Luparello<sup>58,23</sup>, M. Lupi<sup>33</sup>, T.H. Lutz<sup>141</sup>, A. Maevskaya<sup>61</sup>, M. Mager<sup>33</sup>, C. Magureanu<sup>86</sup>, S. Mahajan<sup>100</sup>,  
2160 T. Mahmoud<sup>103</sup>, S.M. Mahmood<sup>19</sup>, A. Maire<sup>133</sup>, R.D. Majka<sup>141</sup>, M. Malaev<sup>95</sup>, L. Malinina<sup>76,vi</sup>,  
2161 D. Mal'Kevich<sup>63</sup>, P. Malzacher<sup>106</sup>, A. Mamonov<sup>108</sup>, V. Manko<sup>89</sup>, F. Manso<sup>131</sup>, V. Manzari<sup>51</sup>, Y. Mao<sup>7</sup>,  
2162 M. Marchisone<sup>75,128</sup>, J. Mareš<sup>65</sup>, G.V. Margagliotti<sup>23</sup>, A. Margotti<sup>52</sup>, J. Margutti<sup>62</sup>, A. Marín<sup>106</sup>,  
2163 C. Markert<sup>119</sup>, M. Marquard<sup>69</sup>, N.A. Martin<sup>106</sup>, P. Martinengo<sup>33</sup>, J.A.L. Martinez<sup>68</sup>, M.I. Martínez<sup>2</sup>,  
2164 G. Martínez García<sup>114</sup>, M. Martinez Pedreira<sup>33</sup>, S. Masciocchi<sup>106</sup>, M. Maserà<sup>24</sup>, A. Masoni<sup>53</sup>, E. Masson<sup>114</sup>,  
2165 A. Mastroserio<sup>51</sup>, A.M. Mathis<sup>34,104</sup>, A. Matyja<sup>127</sup>, C. Mayer<sup>118</sup>, J. Mazer<sup>127</sup>, M. Mazzilli<sup>31</sup>,  
2166 M.A. Mazzoni<sup>56</sup>, F. Meddi<sup>21</sup>, Y. Melikyan<sup>82</sup>, A. Menchaca-Rocha<sup>73</sup>, E. Meninno<sup>28</sup>, J. Mercado Pérez<sup>103</sup>,  
2167 M. Meres<sup>36</sup>, S. Mhlanga<sup>99</sup>, Y. Miake<sup>130</sup>, M.M. Mieskolainen<sup>44</sup>, D.L. Mihaylov<sup>104</sup>, K. Mikhaylov<sup>63,76</sup>,  
2168 J. Milosevic<sup>19</sup>, A. Mischke<sup>62</sup>, A.N. Mishra<sup>47</sup>, D. Miśkowiec<sup>106</sup>, J. Mitra<sup>137</sup>, C.M. Mitu<sup>67</sup>, N. Mohammadi<sup>62</sup>,  
2169 B. Mohanty<sup>87</sup>, M. Mohisin Khan<sup>15,vii</sup>, D.A. Moreira De Godoy<sup>70</sup>, L.A.P. Moreno<sup>2</sup>, S. Moretto<sup>27</sup>, Y. Morino<sup>129</sup>,  
2170 A. Morreale<sup>114</sup>, A. Morsch<sup>33</sup>, V. Muccifora<sup>49</sup>, E. Mudnic<sup>117</sup>, D. Mühlheim<sup>70</sup>, S. Muhuri<sup>137</sup>, M. Mukherjee<sup>4</sup>,  
2171 J.D. Mulligan<sup>141</sup>, M.G. Munhoz<sup>121</sup>, K. Mürning<sup>43</sup>, R.H. Munzer<sup>69</sup>, H. Murakami<sup>129</sup>, S. Murray<sup>75</sup>, L. Musa<sup>33</sup>,  
2172 J. Musinsky<sup>64</sup>, C.J. Myers<sup>124</sup>, J.W. Myrcha<sup>138</sup>, J. Mücke<sup>103</sup>, D. Nag<sup>4</sup>, B. Naik<sup>46</sup>, R. Nair<sup>85</sup>, B.K. Nandi<sup>46</sup>,  
2173 R. Nania<sup>11,52</sup>, E. Nappi<sup>51</sup>, A. Narayan<sup>46</sup>, M.U. Naru<sup>14</sup>, H. Natal da Luz<sup>121</sup>, C. Nattrass<sup>127</sup>, S.R. Navarro<sup>2</sup>,  
2174 K. Nayak<sup>87</sup>, R. Nayak<sup>46</sup>, T.K. Nayak<sup>137</sup>, S. Nazarenko<sup>108</sup>, A. Nedosekin<sup>63</sup>, R.A. Negrao De Oliveira<sup>33</sup>,  
2175 M. Neher<sup>103</sup>, L. Nellen<sup>71</sup>, S.V. Nesbo<sup>35</sup>, F. Ng<sup>124</sup>, M. Nicassio<sup>106</sup>, M. Niculescu<sup>67</sup>, J. Niedziela<sup>33,138</sup>,  
2176 B.S. Nielsen<sup>90</sup>, S. Nikolaev<sup>89</sup>, S. Nikulin<sup>89</sup>, V. Nikulin<sup>95</sup>, F. Noferini<sup>52,11</sup>, P. Nomokonov<sup>76</sup>, G. Nooren<sup>62</sup>,  
2177 J.C.C. Noris<sup>2</sup>, J. Norman<sup>126</sup>, A. Nyanin<sup>89</sup>, J. Nystrand<sup>20</sup>, H. Oeschler<sup>103,i</sup>, S. Oh<sup>141</sup>, A. Ohlson<sup>33,103</sup>,  
2178 T. Okubo<sup>45</sup>, L. Olah<sup>140</sup>, J. Oleniacz<sup>138</sup>, A.C. Oliveira Da Silva<sup>121</sup>, M.H. Oliver<sup>141</sup>, J. Onderwaater<sup>106</sup>,  
2179 C. Oppedisano<sup>57</sup>, R. Orava<sup>44</sup>, M. Oravec<sup>116</sup>, A. Ortiz Velasquez<sup>71</sup>, A. Oskarsson<sup>32</sup>, J. Otwinowski<sup>118</sup>,  
2180 K. Oyama<sup>83</sup>, Y. Pachmayer<sup>103</sup>, V. Pacik<sup>90</sup>, D. Pagano<sup>135</sup>, P. Pagano<sup>28</sup>, G. Paic<sup>71</sup>, Y. Panebratsev<sup>76</sup>, P. Palni<sup>7</sup>,  
2181 J. Pan<sup>139</sup>, A.K. Pandey<sup>46</sup>, S. Panebianco<sup>74</sup>, V. Papikyan<sup>1</sup>, G.S. Pappalardo<sup>54</sup>, P. Pareek<sup>47</sup>, J. Park<sup>59</sup>,  
2182 W. Park<sup>106</sup>, S. Parmar<sup>98</sup>, A. Passfeld<sup>70</sup>, S.P. Pathak<sup>124</sup>, R.N. Patra<sup>137</sup>, B. Paul<sup>57</sup>, H. Pei<sup>7</sup>, T. Peitzmann<sup>62</sup>,  
2183 X. Peng<sup>7</sup>, L.G. Pereira<sup>72</sup>, H. Pereira Da Costa<sup>74</sup>, D. Peresunko<sup>89,82</sup>, E. Perez Lezama<sup>69</sup>, V. Peskov<sup>69</sup>,  
2184 Y. Pestov<sup>5</sup>, V. Petráček<sup>37</sup>, M. Petris<sup>86</sup>, V. Petrov<sup>112</sup>, M. Petrovici<sup>86</sup>, C. Petta<sup>26</sup>, R.P. Pezzi<sup>72</sup>, S. Piano<sup>58</sup>,

- 2185 M. Pikna<sup>36</sup>, P. Pillot<sup>114</sup>, L.O.D.L. Pimentel<sup>90</sup>, O. Pinazza<sup>52,33</sup>, L. Pinsky<sup>124</sup>, N. Pitz<sup>69</sup>, D.B. Piyarathna<sup>124</sup>,  
2186 M. Płoskon<sup>81</sup>, M. Planinic<sup>97</sup>, F. Pliquett<sup>69</sup>, J. Pluta<sup>138</sup>, S. Pochybova<sup>140</sup>, P.L.M. Podesta-Lerma<sup>120</sup>,  
2187 M.G. Poghosyan<sup>94</sup>, B. Polichtchouk<sup>112</sup>, N. Poljak<sup>97</sup>, W. Poonsawat<sup>115</sup>, A. Pop<sup>86</sup>, H. Poppenborg<sup>70</sup>,  
2188 S. Porteboeuf-Houssais<sup>131</sup>, V. Pozdniakov<sup>76</sup>, S.K. Prasad<sup>4</sup>, R. Preghenella<sup>52</sup>, F. Prino<sup>57</sup>, C.A. Pruneau<sup>139</sup>,  
2189 I. Pshenichnov<sup>61</sup>, M. Puccio<sup>24</sup>, G. Puddu<sup>22</sup>, P. Pujahari<sup>139</sup>, V. Punin<sup>108</sup>, J. Putschke<sup>139</sup>, S. Radomski<sup>103</sup>,  
2190 A. Rachevski<sup>58</sup>, S. Raha<sup>4</sup>, S. Rajput<sup>100</sup>, J. Rak<sup>125</sup>, A. Rakotozafindrabe<sup>74</sup>, L. Ramello<sup>30</sup>, F. Rami<sup>133</sup>,  
2191 D.B. Rana<sup>124</sup>, R. Raniwala<sup>101</sup>, S. Raniwala<sup>101</sup>, S.S. Räsänen<sup>44</sup>, B.T. Rascanu<sup>69</sup>, D. Rathee<sup>98</sup>, V. Ratza<sup>43</sup>,  
2192 I. Ravasenga<sup>29</sup>, K.F. Read<sup>94,127</sup>, K. Redlich<sup>85,viii</sup>, A. Rehman<sup>20</sup>, P. Reichelt<sup>69</sup>, F. Reidt<sup>33</sup>, A. Reischl<sup>103</sup>,  
2193 X. Ren<sup>7</sup>, R. Renfordt<sup>69</sup>, A.R. Reolon<sup>49</sup>, A. Reshetin<sup>61</sup>, K. Reygers<sup>103</sup>, V. Riabov<sup>95</sup>, R.A. Ricci<sup>50</sup>, T. Richert<sup>62</sup>,  
2194 M. Richter<sup>19</sup>, P. Riedler<sup>33</sup>, W. Riegler<sup>33</sup>, F. Riggi<sup>26</sup>, C. Ristea<sup>67</sup>, M. Rodríguez Cahuantzi<sup>2</sup>, K. Røed<sup>19</sup>,  
2195 E. Rogochaya<sup>76</sup>, D. Rohr<sup>40,33</sup>, D. Röhrich<sup>20</sup>, P.S. Rokita<sup>138</sup>, F. Ronchetti<sup>49</sup>, E.D. Rosas<sup>71</sup>, P. Rosnet<sup>131</sup>,  
2196 A. Rossi<sup>27,55</sup>, A. Rotondi<sup>134</sup>, F. Roukoutakis<sup>84</sup>, A. Roy<sup>47</sup>, C. Roy<sup>133</sup>, P. Roy<sup>109</sup>, O.V. Rueda<sup>71</sup>, R. Rui<sup>23</sup>,  
2197 B. Rumyantsev<sup>76</sup>, I. Rusanov<sup>103</sup>, A. Rustamov<sup>88</sup>, E. Ryabinkin<sup>89</sup>, Y. Ryabov<sup>95</sup>, A. Rybicki<sup>118</sup>, S. Saarinen<sup>44</sup>,  
2198 S. Sadhu<sup>137</sup>, S. Sadovsky<sup>112</sup>, K. Šafařík<sup>33</sup>, S.K. Saha<sup>137</sup>, B. Sahlmüller<sup>69</sup>, B. Sahoo<sup>46</sup>, P. Sahoo<sup>47</sup>, R. Sahoo<sup>47</sup>,  
2199 S. Sahoo<sup>66</sup>, P.K. Sahu<sup>66</sup>, J. Saini<sup>137</sup>, S. Sakai<sup>130</sup>, D. Sakata<sup>130</sup>, M.A. Saleh<sup>139</sup>, J. Salzwedel<sup>16</sup>, S. Sambyal<sup>100</sup>,  
2200 V. Samsonov<sup>95,82</sup>, A. Sandoval<sup>73</sup>, H. Sann<sup>106,i</sup>, M. Sano<sup>130</sup>, R. Santo<sup>70</sup>, D. Sarkar<sup>137</sup>, N. Sarkar<sup>137</sup>,  
2201 P. Sarma<sup>42</sup>, M.H.P. Sas<sup>62</sup>, E. Scapparone<sup>52</sup>, F. Scarlassara<sup>27</sup>, B. Schaefer<sup>94</sup>, R.P. Scharenberg<sup>105</sup>,  
2202 H.S. Scheid<sup>69</sup>, C. Schiaua<sup>86</sup>, R. Schicker<sup>103</sup>, C. Schmidt<sup>106</sup>, H.R. Schmidt<sup>102</sup>, M.O. Schmidt<sup>103</sup>,  
2203 M. Schmidt<sup>102</sup>, N.V. Schmidt<sup>94,69</sup>, S. Schmiederer<sup>103</sup>, R. Schneider<sup>iv</sup>, J. Schukraft<sup>33</sup>, R. Schulze<sup>106</sup>,  
2204 Y. Schutz<sup>33,133,114</sup>, K. Schwarz<sup>106</sup>, K. Schweda<sup>106</sup>, G. Scioli<sup>25</sup>, E. Scomparin<sup>57</sup>, R. Scott<sup>127</sup>, S. Sedykh<sup>106</sup>,  
2205 M. Šefčík<sup>38</sup>, J.E. Seger<sup>96</sup>, Y. Sekiguchi<sup>129</sup>, D. Sekihata<sup>45</sup>, I. Selyuzhenkov<sup>82,106</sup>, K. Senosi<sup>75</sup>,  
2206 S. Senyukov<sup>33,133,3</sup>, E. Serradilla<sup>73</sup>, P. Sett<sup>46</sup>, A. Sevcenco<sup>67</sup>, A. Shabanov<sup>61</sup>, A. Shabetai<sup>114</sup>, R. Shahoyan<sup>33</sup>,  
2207 W. Shaikh<sup>109</sup>, A. Shangaraev<sup>112</sup>, A. Sharma<sup>98</sup>, A. Sharma<sup>100</sup>, M. Sharma<sup>100</sup>, M. Sharma<sup>100</sup>, N. Sharma<sup>98,127</sup>,  
2208 A.I. Sheikh<sup>137</sup>, K. Shigaki<sup>45</sup>, S. Shimansky<sup>76</sup>, Q. Shou<sup>7</sup>, K. Shtejer<sup>24,9</sup>, P. Shukla<sup>103</sup>, Y. Sibiriak<sup>89</sup>,  
2209 E. Sicking<sup>70</sup>, S. Siddhanta<sup>53</sup>, K.M. Sielewicz<sup>33</sup>, T. Siemiarzczuk<sup>85</sup>, S. Silaeva<sup>89</sup>, D. Silvermyr<sup>32</sup>, C. Silvestre<sup>80</sup>,  
2210 G. Simatovic<sup>97</sup>, R. Simon<sup>106</sup>, G. Simonetti<sup>33</sup>, R. Singaraju<sup>137</sup>, R. Singh<sup>87</sup>, V. Singhal<sup>137</sup>, T. Sinha<sup>109</sup>,  
2211 B. Sitar<sup>36</sup>, M. Sitta<sup>30</sup>, T.B. Skaali<sup>19</sup>, M. Slupecki<sup>125</sup>, N. Smirnov<sup>141</sup>, L. Smykov<sup>76</sup>, R.J.M. Snellings<sup>62</sup>,  
2212 T.W. Snellman<sup>125</sup>, H. Solveit<sup>103</sup>, W. Sommer<sup>69</sup>, J. Song<sup>17</sup>, M. Song<sup>142</sup>, F. Soramel<sup>27</sup>, S. Sorensen<sup>127</sup>,  
2213 F. Sozzi<sup>106</sup>, E. Spiriti<sup>49</sup>, I. Sputowska<sup>118</sup>, B.K. Srivastava<sup>105</sup>, J. Stachel<sup>103</sup>, I. Stan<sup>67</sup>, P. Stankus<sup>94</sup>,  
2214 H. Stelzer<sup>106</sup>, E. Stenlund<sup>32</sup>, J. Stiller<sup>103</sup>, D. Stocco<sup>114</sup>, M. Stockmeyer<sup>103</sup>, M.M. Støretvedt<sup>35</sup>, P. Strmen<sup>36</sup>,  
2215 A.A.P. Suaide<sup>121</sup>, T. Sugitate<sup>45</sup>, C. Suire<sup>60</sup>, M. Suleymanov<sup>14</sup>, M. Suljic<sup>23</sup>, R. Sultanov<sup>63</sup>, M. Šumbera<sup>93</sup>,  
2216 S. Sumowidagdo<sup>48</sup>, K. Suzuki<sup>113</sup>, S. Swain<sup>66</sup>, A. Szabo<sup>36</sup>, I. Szarka<sup>36</sup>, U. Tabassam<sup>14</sup>, J. Takahashi<sup>122</sup>,  
2217 G.J. Tambave<sup>20</sup>, N. Tanaka<sup>130</sup>, M. Tarhini<sup>60</sup>, M. Tariq<sup>15</sup>, M.G. Tazila<sup>86</sup>, A. Tauro<sup>33</sup>, G. Tejada Muñoz<sup>2</sup>,  
2218 A. Telesca<sup>33</sup>, K. Terasaki<sup>129</sup>, C. Terrevoli<sup>27</sup>, B. Teyssier<sup>132</sup>, D. Thakur<sup>47</sup>, S. Thakur<sup>137</sup>, D. Thomas<sup>119</sup>,  
2219 F. Thoresen<sup>90</sup>, R. Tieulent<sup>132</sup>, A. Tikhonov<sup>61</sup>, H. Tilsner<sup>103</sup>, A.R. Timmins<sup>124</sup>, A. Toia<sup>69</sup>, S.R. Torres<sup>120</sup>,  
2220 S. Tripathy<sup>47</sup>, S. Trogolo<sup>24</sup>, G. Trombetta<sup>31</sup>, L. Tropp<sup>38</sup>, V. Trubnikov<sup>3</sup>, W.H. Trzaska<sup>125</sup>, B.A. Trzeciak<sup>62</sup>,  
2221 G. Tsileadakis<sup>103</sup>, T. Tsuji<sup>129</sup>, A. Tumkin<sup>108</sup>, R. Turrisi<sup>55</sup>, T.S. Tveter<sup>19</sup>, K. Ullaland<sup>20</sup>, E.N. Umaka<sup>124</sup>,  
2222 A. Uras<sup>132</sup>, G.L. Usai<sup>22</sup>, A. Utrobicic<sup>97</sup>, M. Vala<sup>116,64</sup>, J. Van Der Maarel<sup>62</sup>, J.W. Van Hoorne<sup>33</sup>, M. van  
2223 Leeuwen<sup>62</sup>, T. Vanat<sup>93</sup>, H. Vargas<sup>69</sup>, P. Vande Vyvre<sup>33</sup>, D. Varga<sup>140</sup>, A. Vargas<sup>2</sup>, M. Vargyas<sup>125</sup>, R. Varma<sup>46</sup>,  
2224 M. Vasileiou<sup>84</sup>, A. Vasiliev<sup>89</sup>, A. Vauthier<sup>80</sup>, O. Vázquez Doce<sup>104,34</sup>, V. Vechernin<sup>136</sup>, A.M. Veen<sup>62</sup>,  
2225 A. Velure<sup>20</sup>, E. Vercellin<sup>24</sup>, S. Vergara Limón<sup>2</sup>, R. Vernet<sup>8</sup>, R. Vértesi<sup>140</sup>, L. Vickovic<sup>117</sup>, S. Vigolo<sup>62</sup>,  
2226 J. Viinikainen<sup>125</sup>, Z. Vilakazi<sup>128</sup>, O. Villalobos Baillie<sup>110</sup>, A. Villatoro Tello<sup>2</sup>, A. Vinogradov<sup>89</sup>,  
2227 L. Vinogradov<sup>136</sup>, T. Virgili<sup>28</sup>, V. Vislavicius<sup>32</sup>, A. Vodopyanov<sup>76</sup>, M.A. Völkl<sup>103,102</sup>, K. Voloshin<sup>63</sup>,  
2228 S.A. Voloshin<sup>139</sup>, G. Volpe<sup>31</sup>, B. von Haller<sup>33</sup>, I. Vorobyev<sup>104,34</sup>, D. Voscek<sup>116</sup>, D. Vranic<sup>33,106</sup>, J. Vrláková<sup>38</sup>,  
2229 B. Vulpesu<sup>103</sup>, B. Wagner<sup>20</sup>, H. Wang<sup>62</sup>, M. Wang<sup>7</sup>, Y. Wang<sup>103</sup>, D. Watanabe<sup>130</sup>, K. Watanabe<sup>130</sup>,  
2230 Y. Watanabe<sup>129,130</sup>, M. Weber<sup>113</sup>, S.G. Weber<sup>106</sup>, D. Wegerle<sup>69</sup>, D.F. Weiser<sup>103</sup>, S.C. Wenzel<sup>33</sup>,  
2231 J.P. Wessels<sup>70</sup>, U. Westerhoff<sup>70</sup>, A.M. Whitehead<sup>99</sup>, J. Wiechula<sup>69</sup>, J. Wikne<sup>19</sup>, A. Wilk<sup>70</sup>, G. Wilk<sup>85</sup>,  
2232 J. Wilkinson<sup>103,52</sup>, G.A. Willems<sup>70</sup>, M.C.S. Williams<sup>52</sup>, E. Willsher<sup>110</sup>, B. Windelband<sup>103</sup>, M. Winn<sup>103</sup>,  
2233 W.E. Witt<sup>127</sup>, C. Xu<sup>103</sup>, S. Yalcin<sup>79</sup>, K. Yamakawa<sup>45</sup>, P. Yang<sup>7</sup>, S. Yano<sup>45</sup>, Z. Yin<sup>7</sup>, H. Yokoyama<sup>130,80</sup>,  
2234 I.-K. Yoo<sup>17</sup>, J.H. Yoon<sup>59</sup>, V. Yurchenko<sup>3</sup>, V. Yurevich<sup>76</sup>, V. Zaccolo<sup>57</sup>, A. Zaman<sup>14</sup>, C. Zampolli<sup>33</sup>,  
2235 H.J.C. Zanoli<sup>121</sup>, Y. Zanevski<sup>76,i</sup>, N. Zardoshti<sup>110</sup>, A. Zarochentsev<sup>136</sup>, P. Závada<sup>65</sup>, N. Zaviyalov<sup>108</sup>,  
2236 H. Zbroszczyk<sup>138</sup>, M. Zhalov<sup>95</sup>, H. Zhang<sup>20,7</sup>, X. Zhang<sup>7</sup>, Y. Zhang<sup>7</sup>, C. Zhang<sup>62</sup>, Z. Zhang<sup>131,7</sup>, C. Zhao<sup>19</sup>,  
2237 N. Zhigareva<sup>63</sup>, D. Zhou<sup>7</sup>, Y. Zhou<sup>90</sup>, Z. Zhou<sup>20</sup>, H. Zhu<sup>20</sup>, J. Zhu<sup>7</sup>, A. Zichichi<sup>11,25</sup>, S. Zimmer<sup>103</sup>,  
2238 A. Zimmermann<sup>103</sup>, M.B. Zimmermann<sup>33</sup>, G. Zinovjev<sup>3</sup>, J. Zmeskal<sup>113</sup>, S. Zou<sup>7</sup>,

2239 **Affiliation notes**

- 2240 <sup>i</sup> Deceased  
 2241 <sup>ii</sup> Dipartimento DET del Politecnico di Torino, Turin, Italy  
 2242 <sup>iii</sup> Georgia State University, Atlanta, Georgia, United States  
 2243 <sup>iv</sup> Kirchhoff-Institut für Physik, Ruprecht-Karls-Universität Heidelberg, Heidelberg, Germany  
 2244 <sup>v</sup> Fachhochschule Köln, Köln, Germany  
 2245 <sup>vi</sup> M.V. Lomonosov Moscow State University, D.V. Skobel'syn Institute of Nuclear, Physics, Moscow, Russia  
 2246 <sup>vii</sup> Department of Applied Physics, Aligarh Muslim University, Aligarh, India  
 2247 <sup>viii</sup> Institute of Theoretical Physics, University of Wrocław, Poland

2248 **Collaboration Institutes**

- 2249 <sup>1</sup> A.I. Alikhanyan National Science Laboratory (Yerevan Physics Institute) Foundation, Yerevan, Armenia  
 2250 <sup>2</sup> Benemérita Universidad Autónoma de Puebla, Puebla, Mexico  
 2251 <sup>3</sup> Bogolyubov Institute for Theoretical Physics, Kiev, Ukraine  
 2252 <sup>4</sup> Bose Institute, Department of Physics and Centre for Astroparticle Physics and Space Science (CAPSS),  
 2253 Kolkata, India  
 2254 <sup>5</sup> Budker Institute for Nuclear Physics, Novosibirsk, Russia  
 2255 <sup>6</sup> California Polytechnic State University, San Luis Obispo, California, United States  
 2256 <sup>7</sup> Central China Normal University, Wuhan, China  
 2257 <sup>8</sup> Centre de Calcul de l'IN2P3, Villeurbanne, Lyon, France  
 2258 <sup>9</sup> Centro de Aplicaciones Tecnológicas y Desarrollo Nuclear (CEADEN), Havana, Cuba  
 2259 <sup>10</sup> Centro de Investigación y de Estudios Avanzados (CINVESTAV), Mexico City and Mérida, Mexico  
 2260 <sup>11</sup> Centro Fermi - Museo Storico della Fisica e Centro Studi e Ricerche "Enrico Fermi", Rome, Italy  
 2261 <sup>12</sup> Chicago State University, Chicago, Illinois, United States  
 2262 <sup>13</sup> China Institute of Atomic Energy, Beijing, China  
 2263 <sup>14</sup> COMSATS Institute of Information Technology (CIIT), Islamabad, Pakistan  
 2264 <sup>15</sup> Department of Physics, Aligarh Muslim University, Aligarh, India  
 2265 <sup>16</sup> Department of Physics, Ohio State University, Columbus, Ohio, United States  
 2266 <sup>17</sup> Department of Physics, Pusan National University, Pusan, Republic of Korea  
 2267 <sup>18</sup> Department of Physics, Sejong University, Seoul, Republic of Korea  
 2268 <sup>19</sup> Department of Physics, University of Oslo, Oslo, Norway  
 2269 <sup>20</sup> Department of Physics and Technology, University of Bergen, Bergen, Norway  
 2270 <sup>21</sup> Dipartimento di Fisica dell'Università 'La Sapienza' and Sezione INFN, Rome, Italy  
 2271 <sup>22</sup> Dipartimento di Fisica dell'Università and Sezione INFN, Cagliari, Italy  
 2272 <sup>23</sup> Dipartimento di Fisica dell'Università and Sezione INFN, Trieste, Italy  
 2273 <sup>24</sup> Dipartimento di Fisica dell'Università and Sezione INFN, Turin, Italy  
 2274 <sup>25</sup> Dipartimento di Fisica e Astronomia dell'Università and Sezione INFN, Bologna, Italy  
 2275 <sup>26</sup> Dipartimento di Fisica e Astronomia dell'Università and Sezione INFN, Catania, Italy  
 2276 <sup>27</sup> Dipartimento di Fisica e Astronomia dell'Università and Sezione INFN, Padova, Italy  
 2277 <sup>28</sup> Dipartimento di Fisica 'E.R. Caianiello' dell'Università and Gruppo Collegato INFN, Salerno, Italy  
 2278 <sup>29</sup> Dipartimento DISAT del Politecnico and Sezione INFN, Turin, Italy  
 2279 <sup>30</sup> Dipartimento di Scienze e Innovazione Tecnologica dell'Università del Piemonte Orientale and INFN  
 2280 Sezione di Torino, Alessandria, Italy  
 2281 <sup>31</sup> Dipartimento Interateneo di Fisica 'M. Merlin' and Sezione INFN, Bari, Italy  
 2282 <sup>32</sup> Division of Experimental High Energy Physics, University of Lund, Lund, Sweden  
 2283 <sup>33</sup> European Organization for Nuclear Research (CERN), Geneva, Switzerland  
 2284 <sup>34</sup> Excellence Cluster Universe, Technische Universität München, Munich, Germany  
 2285 <sup>35</sup> Faculty of Engineering, Bergen University College, Bergen, Norway  
 2286 <sup>36</sup> Faculty of Mathematics, Physics and Informatics, Comenius University, Bratislava, Slovakia  
 2287 <sup>37</sup> Faculty of Nuclear Sciences and Physical Engineering, Czech Technical University in Prague, Prague,  
 2288 Czech Republic  
 2289 <sup>38</sup> Faculty of Science, P.J. Šafárik University, Košice, Slovakia  
 2290 <sup>39</sup> Faculty of Technology, Buskerud and Vestfold University College, Tonsberg, Norway  
 2291 <sup>40</sup> Frankfurt Institute for Advanced Studies, Johann Wolfgang Goethe-Universität Frankfurt, Frankfurt,  
 2292 Germany  
 2293 <sup>41</sup> Gangneung-Wonju National University, Gangneung, Republic of Korea

- 2294 42 Gauhati University, Department of Physics, Guwahati, India  
 2295 43 Helmholtz-Institut für Strahlen- und Kernphysik, Rheinische Friedrich-Wilhelms-Universität Bonn, Bonn,  
 2296 Germany  
 2297 44 Helsinki Institute of Physics (HIP), Helsinki, Finland  
 2298 45 Hiroshima University, Hiroshima, Japan  
 2299 46 Indian Institute of Technology Bombay (IIT), Mumbai, India  
 2300 47 Indian Institute of Technology Indore, Indore, India  
 2301 48 Indonesian Institute of Sciences, Jakarta, Indonesia  
 2302 49 INFN, Laboratori Nazionali di Frascati, Frascati, Italy  
 2303 50 INFN, Laboratori Nazionali di Legnaro, Legnaro, Italy  
 2304 51 INFN, Sezione di Bari, Bari, Italy  
 2305 52 INFN, Sezione di Bologna, Bologna, Italy  
 2306 53 INFN, Sezione di Cagliari, Cagliari, Italy  
 2307 54 INFN, Sezione di Catania, Catania, Italy  
 2308 55 INFN, Sezione di Padova, Padova, Italy  
 2309 56 INFN, Sezione di Roma, Rome, Italy  
 2310 57 INFN, Sezione di Torino, Turin, Italy  
 2311 58 INFN, Sezione di Trieste, Trieste, Italy  
 2312 59 Inha University, Incheon, Republic of Korea  
 2313 60 Institut de Physique Nucléaire d'Orsay (IPNO), Université Paris-Sud, CNRS-IN2P3, Orsay, France  
 2314 61 Institute for Nuclear Research, Academy of Sciences, Moscow, Russia  
 2315 62 Institute for Subatomic Physics of Utrecht University, Utrecht, Netherlands  
 2316 63 Institute for Theoretical and Experimental Physics, Moscow, Russia  
 2317 64 Institute of Experimental Physics, Slovak Academy of Sciences, Košice, Slovakia  
 2318 65 Institute of Physics, Academy of Sciences of the Czech Republic, Prague, Czech Republic  
 2319 66 Institute of Physics, Bhubaneswar, India  
 2320 67 Institute of Space Science (ISS), Bucharest, Romania  
 2321 68 Institut für Informatik, Johann Wolfgang Goethe-Universität Frankfurt, Frankfurt, Germany  
 2322 69 Institut für Kernphysik, Johann Wolfgang Goethe-Universität Frankfurt, Frankfurt, Germany  
 2323 70 Institut für Kernphysik, Westfälische Wilhelms-Universität Münster, Münster, Germany  
 2324 71 Instituto de Ciencias Nucleares, Universidad Nacional Autónoma de México, Mexico City, Mexico  
 2325 72 Instituto de Física, Universidade Federal do Rio Grande do Sul (UFRGS), Porto Alegre, Brazil  
 2326 73 Instituto de Física, Universidad Nacional Autónoma de México, Mexico City, Mexico  
 2327 74 IRFU, CEA, Université Paris-Saclay, Saclay, France  
 2328 75 iThemba LABS, National Research Foundation, Somerset West, South Africa  
 2329 76 Joint Institute for Nuclear Research (JINR), Dubna, Russia  
 2330 77 Konkuk University, Seoul, Republic of Korea  
 2331 78 Korea Institute of Science and Technology Information, Daejeon, Republic of Korea  
 2332 79 KTO Karatay University, Konya, Turkey  
 2333 80 Laboratoire de Physique Subatomique et de Cosmologie, Université Grenoble-Alpes, CNRS-IN2P3,  
 2334 Grenoble, France  
 2335 81 Lawrence Berkeley National Laboratory, Berkeley, California, United States  
 2336 82 Moscow Engineering Physics Institute, Moscow, Russia  
 2337 83 Nagasaki Institute of Applied Science, Nagasaki, Japan  
 2338 84 National and Kapodistrian University of Athens, Physics Department, Athens, Greece  
 2339 85 National Centre for Nuclear Studies, Warsaw, Poland  
 2340 86 National Institute for Physics and Nuclear Engineering, Bucharest, Romania  
 2341 87 National Institute of Science Education and Research, HBNI, Jatni, India  
 2342 88 National Nuclear Research Center, Baku, Azerbaijan  
 2343 89 National Research Centre Kurchatov Institute, Moscow, Russia  
 2344 90 Niels Bohr Institute, University of Copenhagen, Copenhagen, Denmark  
 2345 91 Nikhef, Nationaal instituut voor subatomaire fysica, Amsterdam, Netherlands  
 2346 92 Nuclear Physics Group, STFC Daresbury Laboratory, Daresbury, United Kingdom  
 2347 93 Nuclear Physics Institute, Academy of Sciences of the Czech Republic, Řež u Prahy, Czech Republic  
 2348 94 Oak Ridge National Laboratory, Oak Ridge, Tennessee, United States  
 2349 95 Petersburg Nuclear Physics Institute, Gatchina, Russia

- 2350 <sup>96</sup> Physics Department, Creighton University, Omaha, Nebraska, United States  
 2351 <sup>97</sup> Physics department, Faculty of science, University of Zagreb, Zagreb, Croatia  
 2352 <sup>98</sup> Physics Department, Panjab University, Chandigarh, India  
 2353 <sup>99</sup> Physics Department, University of Cape Town, Cape Town, South Africa  
 2354 <sup>100</sup> Physics Department, University of Jammu, Jammu, India  
 2355 <sup>101</sup> Physics Department, University of Rajasthan, Jaipur, India  
 2356 <sup>102</sup> Physikalisches Institut, Eberhard Karls Universität Tübingen, Tübingen, Germany  
 2357 <sup>103</sup> Physikalisches Institut, Ruprecht-Karls-Universität Heidelberg, Heidelberg, Germany  
 2358 <sup>104</sup> Physik Department, Technische Universität München, Munich, Germany  
 2359 <sup>105</sup> Purdue University, West Lafayette, Indiana, United States  
 2360 <sup>106</sup> Research Division and ExtreMe Matter Institute EMMI, GSI Helmholtzzentrum für  
 2361 Schwerionenforschung GmbH, Darmstadt, Germany  
 2362 <sup>107</sup> Rudjer Bošković Institute, Zagreb, Croatia  
 2363 <sup>108</sup> Russian Federal Nuclear Center (VNIIEF), Sarov, Russia  
 2364 <sup>109</sup> Saha Institute of Nuclear Physics, Kolkata, India  
 2365 <sup>110</sup> School of Physics and Astronomy, University of Birmingham, Birmingham, United Kingdom  
 2366 <sup>111</sup> Sección Física, Departamento de Ciencias, Pontificia Universidad Católica del Perú, Lima, Peru  
 2367 <sup>112</sup> SSC IHEP of NRC Kurchatov institute, Protvino, Russia  
 2368 <sup>113</sup> Stefan Meyer Institut für Subatomare Physik (SMI), Vienna, Austria  
 2369 <sup>114</sup> SUBATECH, IMT Atlantique, Université de Nantes, CNRS-IN2P3, Nantes, France  
 2370 <sup>115</sup> Suranaree University of Technology, Nakhon Ratchasima, Thailand  
 2371 <sup>116</sup> Technical University of Košice, Košice, Slovakia  
 2372 <sup>117</sup> Technical University of Split FESB, Split, Croatia  
 2373 <sup>118</sup> The Henryk Niewodniczanski Institute of Nuclear Physics, Polish Academy of Sciences, Cracow, Poland  
 2374 <sup>119</sup> The University of Texas at Austin, Physics Department, Austin, Texas, United States  
 2375 <sup>120</sup> Universidad Autónoma de Sinaloa, Culiacán, Mexico  
 2376 <sup>121</sup> Universidade de São Paulo (USP), São Paulo, Brazil  
 2377 <sup>122</sup> Universidade Estadual de Campinas (UNICAMP), Campinas, Brazil  
 2378 <sup>123</sup> Universidade Federal do ABC, Santo Andre, Brazil  
 2379 <sup>124</sup> University of Houston, Houston, Texas, United States  
 2380 <sup>125</sup> University of Jyväskylä, Jyväskylä, Finland  
 2381 <sup>126</sup> University of Liverpool, Liverpool, United Kingdom  
 2382 <sup>127</sup> University of Tennessee, Knoxville, Tennessee, United States  
 2383 <sup>128</sup> University of the Witwatersrand, Johannesburg, South Africa  
 2384 <sup>129</sup> University of Tokyo, Tokyo, Japan  
 2385 <sup>130</sup> University of Tsukuba, Tsukuba, Japan  
 2386 <sup>131</sup> Université Clermont Auvergne, CNRS-IN2P3, LPC, Clermont-Ferrand, France  
 2387 <sup>132</sup> Université de Lyon, Université Lyon 1, CNRS/IN2P3, IPN-Lyon, Villeurbanne, Lyon, France  
 2388 <sup>133</sup> Université de Strasbourg, CNRS, IPHC UMR 7178, F-67000 Strasbourg, France, Strasbourg, France  
 2389 <sup>134</sup> Università degli Studi di Pavia, Pavia, Italy  
 2390 <sup>135</sup> Università di Brescia, Brescia, Italy  
 2391 <sup>136</sup> V. Fock Institute for Physics, St. Petersburg State University, St. Petersburg, Russia  
 2392 <sup>137</sup> Variable Energy Cyclotron Centre, Kolkata, India  
 2393 <sup>138</sup> Warsaw University of Technology, Warsaw, Poland  
 2394 <sup>139</sup> Wayne State University, Detroit, Michigan, United States  
 2395 <sup>140</sup> Wigner Research Centre for Physics, Hungarian Academy of Sciences, Budapest, Hungary  
 2396 <sup>141</sup> Yale University, New Haven, Connecticut, United States  
 2397 <sup>142</sup> Yonsei University, Seoul, Republic of Korea  
 2398 <sup>143</sup> Zentrum für Technologietransfer und Telekommunikation (ZTT), Fachhochschule Worms, Worms,  
 2399 Germany